The Dissertation Committee for Jun Wen
certifies that this is the approved version of the following dissertation:

Interaction Effects in Topological Insulators

Committee:

Gregory A. Fiete, Supervisor

Allan H. MacDonald

Qian Niu

Zhen Yao

James R. Chelikowsky

Interaction Effects in Topological Insulators

by

Jun Wen, B.S., M.S.

Dissertation

Presented to the Faculty of the Graduate School of

The University of Texas at Austin

in Partial Fulfillment

of the Requirements

for the Degree of

Doctor of Philosophy

The University of Texas at Austin

May 2012

Dedicated to My Parents and My Wife

Acknowledgments

First and foremost, I would like to express my sincere gratitude to my advisor Gregory Fiete, who has been an excellent mentor to me. His insight into physics problems and thoughtful guidance have opened many doors of opportunity for me. I am also indebted to him for his constant support, kindness, patience and understanding. Without his encouragement, this PhD thesis would not have been possible.

I have had great pleasure of working and collaborating with many others during my PhD study. I would like to thank Allan MacDonald, Qian Niu, Zhen Yao and Jim Chelikowsky, who introduced me to various fields of condensed matter theory and took the time to serve on my dissertation committee. I would also like to thank Andreas Rüegg, Mehdi Kargarian, Abolhassan Vaezi, C.-C. Joseph Wang, Di Xiao, Yugui Yao, Wanxiang Feng and Dagim Tilahun for providing me generous assistance as we worked on projects together.

I am also grateful for my other group members who I have not mentioned above: Stuart Sevier, Victor Chua, Xiang Hu, Rex Lundgren, Vladimir Zyuzin. It was so pleasant to discuss physics problems with them and many of our discussions inspired me in a way they probably did not realize.

I wish to express special gratitude to my dearest friends in Austin, Jingxue Lu, Xiaowen Zhang, Wei Xie, Yi Sui, Jiabei Yuan, Yan Yan, Tuo Wang, Xinyu Gu, Dan Gao, Xianhui Kong, Zhiheng Li, Ye Tian, Chao Wang, Ku He, Yingying Jiang, Xiaojing Jiang, Yujia Zhai, Hao Tang, Tang Fang, Zekun Shi, Fan Zhang, Qing Xu, Changhai Xu, Jing Zan, Junwei Wei, Xuhui Luo, Shengyuan Yang, Liming Luo, Peng Dong, Ligang Long, Huan Li, Chen Su, Zhuojie Wu, Rao Wang, Zhehui Mao, Yihua Cai, Neil Ni, Garrett Fair, Tin Dinh, and Xu Wang. All of you make my life in Austin great and I will never forget our friendship.

Finally, I wish to thank my father Huiliang Wen, my mother Yuying Wen and my wife Xiaoyu Wu for their unconditional love and constant support in my life.

JUN WEN

The University of Texas at Austin
May 2012

Interaction Effects in Topological Insulators

Publication No. ____________________

Jun Wen, Ph.D.
The University of Texas at Austin, 2012

Supervisor: Gregory A. Fiete

In this thesis we employ various mean-field approaches to study the short-range interaction effects in topological insulators. We start with the Kane-Mele model on the decorated honeycomb lattice and study the stability of topological insulator phase against different perturbations. We establish an adiabatic connection between a noninteracting topological insulator and a strongly interacting spin liquid in its Majorana fermion representation.

We use the Hartree-Fock mean-field approach, slave-rotor approach and slave-boson approach to study correlation effects related to topological insulators. With the spontaneous symmetry breaking mechanism, we can have an interaction-driven topological insulator with extended Hubbard models on the kagome lattice and decorated honeycomb lattice. For the interplay among spin-orbit coupling, distortion and correlation effect in transition metal oxides, we use the slave-rotor mean-field approach to study its phase transition. We identify regimes where a strong topological Mott insulator and a weak topological insulator reside due to the strong Coulomb interaction and distortion. This is relevant to experiments with the transition metal oxides as they hold promise to realize topological insulators. To study the doping effects and a possible spin liquid in Kane-Mele-Hubbard model on the honeycomb lattice, we employ the slave-boson mean-field approach which is appropriate for the intermediate interaction strength. We compare our results with those obtained from other methods.

Contents

List of Figures

Chapter 1

Introduction

1.1 Topological Insulators

The search for novel phases with distinctive orders has been a constant drive in condensed matter physics. Before the 1980s, Landau's approach, which classifies states in terms of underlying spontaneous breaking symmetry, was very successful until the discovery of the quantum Hall effect. The notion of topological order [1, 2] was developed to describe a topological phase in which no symmetry is broken but certain fundamental properties (like the quantized value of Hall conductance and the number of massless edge states) are insensitive to smooth changes of parameters until a quantum phase transition is reached.

In the past few years, a new state called a topological insulator has been predicted[3–9] and observed[10–13]. This is based on the realization that the relativistic spin-orbit coupling which lead to a new topological order when combined with time-reversal symmetry. A topological insulator has a bulk gap like an ordinary insulator, but differs from an ordinary insulator by the existence of topologically protected gapless modes on the boundary. In two dimension, a topological insulator can be viewed as two copies of Haldane's quantum anomalous Hall insulator[14] with opposite effective magnetic fields for different spins. Due to the cancelation of effective magnetic field, the system preserves time-reversal symmetry, but "inherits" gapless modes on the boundary. A three-dimension topological insulator[5]is more interesting in that it does not have a counterpart in quantum Hall states. It also has gapless surface states which possess an odd number of Dirac points in the surface state Brillouin zone.

The theory of topological insulators can be simply understood in the framework of Bloch band theory which exploits the translational symmetry to classify states with some momentum for systems with periodic boundary conditions. The existence of a bulk gap together with time reversal symmetry allows only an ordinary insulator or a topological insulator. The mathematical description of topological insulator is based on a Z_2 invariant[4] instead of Z invariant as in integer quantum Hall systems[1]. The Z_2 number can either be 1 or 0 with 1 indicating there are gapless modes on the boundary. An even number of gapless modes on the boundary can be gapped out due to the scattering between them, however, there is always at least one gapless mode on the boundary for a topological insulator.

1.2 Outline of the thesis

While there are many fascinating properties associated with topological insulators, I am particularly interested in the role of electron-electron interactions in topological insulators. According to the principle of adiabatic continuation, a topological insulator is stable against weak interactions due to the presence of a bulk gap[3, 4]. However, the fate of a topological insulator in the presence of intermediate or strong interactions remain unclear. There has been a recent development in theories of interacting topological insulators where the single-particle Green functions are required to identify topological properties[15]. Nevertheless, finding the exact interacting Green's function itself is a challenging task. In this thesis, I take various mean-field approaches to treat the electron-electron interactions and study it with different aspects.

This thesis is a collection of my recent works under the supervision of Professor Gregory Fiete at the University of Texas at Austin.

In Chapter 2[16], we show that the decorated honeycomb lattice supports a number of topological insulating phases with a non-trivial Z_2 invariant and time-reversal symmetry protected gapless edge modes. We investigate the stability of these phases with respect to various symmetry breaking perturbations and demonstrate the connection to the recently discovered exactly solvable $S = 1/2$ chiral spin liquid model[17] with non-Abelian and Abelian excitations on the same lattice. Our work highlights the relationship between topological band insulators and topologically ordered spin systems, and points to promising avenues for enlarging the number of known examples of both.

In Chapter 3[18],we study the spinless and spinful extended Hubbard models with repulsive interactions on the kagome and the decorated honeycomb ("star") lattice. Using Hartree-Fock mean-field theory, we show that interaction-driven insulating phases with non-trivial topological invariants (Chern number or Z_2 invariant) exist for an experimentally reasonable range of parameters. These phases occur at filling fractions which involve either Dirac points or quadratic band crossing points in the non-interacting limit. We present comprehensive mean-field phase diagrams for these lattices and discuss the competition between topologically non-trivial phases and numerous other ordered states, including various charge, spin, and bond orderings. Our results suggest that Z_2 topological insulators should be found in a number of systems with either little or no intrinsic spin-orbit coupling.

In Chapter 4[19], we investigate the phase diagram of heavy ($4d$ and $5d$) transition metal oxides on the pyrochlore lattice, such as those of the form $\mathrm{A_2M_2O_7}$, where A is a rare earth element and M is a transition metal element. We focus on the competition between Coulomb interaction, spin-orbit coupling, and lattice distortion when these energy scales are comparable. Strong spin-orbit coupling entangles the spin and the t_{2g} d-orbitals giving rise to doublet $j = 1/2$ and quadruplet $j = 3/2$ states. In contrast to previous works which focused on the doublet manifold, we also discuss the quadruplet manifold which is relevant for several pyrochlore oxides. The Coulomb interaction is taken into account by use of the slave-rotor mean-field theory and different classes of lattice distortions which further split the levels of the quadruplet $j = 3/2$ manifold are studied. Various topological phases are predicted, including exotic strong and weak topological Mott insulating phases. We discuss the general structure of the phase diagram for several values of d-shell filling and various symmetry classes of lattice distortions. Our results are relevant to the search for exotic topological insulators and quantum spin liquids in strongly correlated materials with strong spin-orbit coupling.

In Chapter 4[20],we study the Kane-Mele-Hubbard model both at half-filling and away from half-filling using a slave-boson mean-field approach at zero temperature. We obtain a phase diagram at half-filling and discuss its connection to recent results from quantum Monte Carlo, cellular dynamical mean-field, slave-rotor, and Z_2 mean-field studies. In particular, we find a small window in parameter space where a spin liquid phase with gapped spin and charge excitations reside. Upon doping, we show the spin liquid state becomes a superconducting state by explicitly calculating the singlet pairing order parameters. Interestingly, we find an “optimal” doping for such superconductivity. Our work reveals some of the phenomenology associated with doping an interacting system with strong spin-orbit coupling and intermediate strength electron-electron interactions.

In Chapter 6, we conclude this thesis by discussing future directions, especially on the newly discovered Weyl semimetals [21]. We also discuss possible future projects on Weyl semimetals.

Chapter 2

Topological Insulators On the Decorated Honeycomb Lattice

2.1 Introduction

In recent years, the study of various types of topological order in condensed matter physics has dramatically increased [22–24]. The interest in this topic has been driven in large part by the fractional quantum Hall effect, and efforts to understand the high temperature superconductors. In both cases electron interactions are fundamental to the phenomena. However, a new class of systems, non-interacting Z_2 topological band insulators (TBI) with time-reversal symmetry (TRS), has diverted attention to topological properties that do not depend on interactions (but are robust to weak interactions)[3, 4, 25]. The existence of topological properties in models that can be exactly solved in the non-interacting limit, and treated to a high degree of accuracy by conventional band theory methods in the interacting limit, has led to precise predictions for experiment[10, 26–28]. An unusually rapid verification of many of these predictions in experiment has followed, and there are now several known examples of this state of matter in both two dimensional [11, 29] and three dimensional systems[12, 30–32]. In some of these materials, topological properties are expected to be robust up to room temperature and therefore hold great promise as components of future electronic devices[31].

Current theoretical research on topological insulators is proceeding along several parallel tracks. On the one hand, there is great interest in identifying new physical systems that will possess topologically non-trivial phases[33–39], while on the other hand there are fundamental questions about the fate of topological properties as the strong electron interaction limit is approached[40, 41]. In this work, we contribute to both directions by providing several other examples of Z_2 TBIs on a lattice where they have not been reported before–the decorated honeycomb lattice. We also establish a topological connection at 1/2 filling between the non-interacting limit and the strongly interacting limit where an exactly solvable electron model (the Kitaev spin model) is realized on the same lattice[17]. We are unaware of any other model that realizes exactly solvable states at weak and strong interaction, both with topological properties. Moreover, via explicit calculation, we show these two limits share topological properties, even though their symmetries are very different.

Our discussion focuses on a tight-binding model of fermions hopping on the 2-dimensional decorated honeycomb lattice shown in Fig. 2.1. This lattice is a "cousin" of both the honeycomb lattice and the kagome lattice, each of which is known to support TBI phases[3, 14, 33, 42, 43]. In a certain regard, the decorated honeycomb lattice can be viewed as an "interpolating" lattice between the honeycomb and the kagome: If one shrinks the triangles at the verticies of the *underlying* honeycomb lattice (sites with hopping parameter t in the figure) to their center point, the honeycomb lattice is recovered, while expanding the triangles until their corners touch produces the kagome lattice. One might consider this geometrical property to be the key reason the decorated honeycomb lattice supports topological insulator phases, given that the honeycomb and kagome lattices also support topological phases. However, because the unit cell of the decorated honeycomb lattice contains 6 sites (compared to 3 for the kagome and 2 for the honeycomb) its phase diagram is much richer than that of either of its "cousins" and some novel features appear that we will discuss in more detail below.

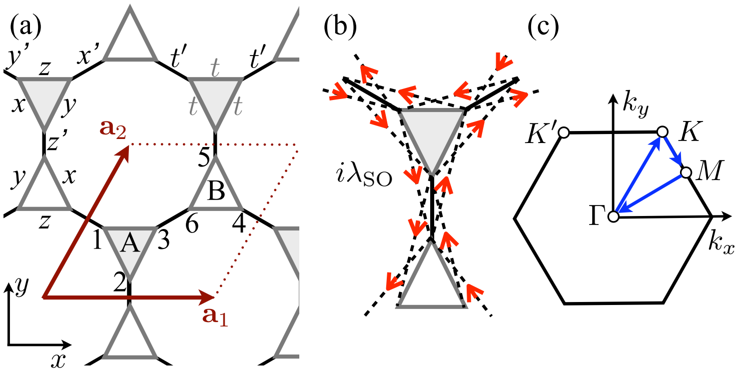

Figure 2.1: (a) The decorated honeycomb lattice has a triangle at each vertex of the honeycomb lattice. The 6-site unit cell with "sublattice" A and B is contained in the parallelogram indicated by $\mathbf{a}_1$ and $\mathbf{a}_2$. Nearest neighbor hopping on vertex triangles occurs with amplitude t, between triangles with amplitude t', and with $\pm i\lambda_{\rm SO}$ for second neighbor hopping as indicated in (b). Topological phases occur at a number of filling fractions (see Fig. 2.3), as well as in the case that $\lambda_{\rm SO} \equiv 0$ and t is allowed to be complex corresponding to finite flux through vertex triangles. (c) The first Brillouin zone including a path along the high-symmetry lines.

2.2 Tight-binding model

The Hamiltonian for our (initially non-interacting) problem is

$$H = H_0 + H_{\mathrm{SO}} + H_{\mathrm{CDW}} + H_{\mathrm{R}}. \tag{2.1}$$

The nearest-neighbor hopping is described by

$$H_0 = -t \sum_{\langle ij\rangle,\sigma,\Delta} c^{\dagger}_{i\sigma} c_{j\sigma} - t' \sum_{\langle ij\rangle,\sigma,\Delta\to\Delta} c^{\dagger}_{i\sigma} c_{j\sigma} + \mathrm{h.c.} \tag{2.2}$$

with amplitude t on the triangles "Δ" and with amplitude t' between triangles "$\Delta \to \Delta$", as shown in Fig. 2.1(a). The intrinsic spin-orbit coupling,

$$H_{\mathrm{SO}} = i\lambda_{\mathrm{SO}} \sum_{\langle\langle ij\rangle\rangle,\alpha,\beta} \vec{e}_{ij} \cdot \vec{s}_{\alpha\beta} c^{\dagger}_{i\alpha} c_{j\beta} + \mathrm{h.c.}, \tag{2.3}$$

describes the second-neighbor hopping with amplitude $\pm i\lambda_{\mathrm{SO}}$, see Fig. 2.1(b). The sign of the amplitude is different for different spin orientations $s_z = \pm 1$, $\vec{s}$ is the vector of Pauli matrices and $\vec{e}_{ij} = (\mathbf{d}^1_{ij} \times \mathbf{d}^2_{ij})/|\mathbf{d}^1_{ij} \times \mathbf{d}^2_{ij}|$ is a vector normal to the $x-y$ plane describing how the path $\langle\langle ij\rangle\rangle$ was traversed using the standard conventions[3]. In Eq. (2.1), H_{CDW} and H_{R} are charge density wave and Rashba spin-orbit terms, respectively. The CDW Hamiltonian is

$$H_{\mathrm{CDW}} = \sum_{i,\sigma} \lambda_{vi} c^{\dagger}_{i\sigma} c_{i\sigma}, \tag{2.4}$$

and the Rashba Hamiltonian is

$$H_{\mathrm{R}} = i\lambda_{\mathrm{R}} \sum_{\langle ij\rangle,\alpha,\beta} c^{\dagger}_{i\alpha} (\vec{s}_{\alpha\beta} \times \hat{d}_{ij})_z c_{j\beta} + \mathrm{h.c.}, \tag{2.5}$$

where λ_{vi} is an on-site potential possibly differing on each of the 6 unit cell sites labeled in Fig. 2.1, λ_{R} is the strength of the Rashba coupling and $\hat{d}_{ij}$ is the unit vector connecting site i to j.

2.3 Phase diagrams

The 6 (doubly degenerate) bands coming from the 6-site unit cell (see Fig. 2.1) for $H_0 + H_{\mathrm{SO}}$ are shown in Fig. 2.2 along the various high symmetry directions. The first Brillouin zone is identical to that of the honeycomb and kagome lattices which share the same underlying triangular Bravais lattice[3, 33], see Fig. 2.1(c). There

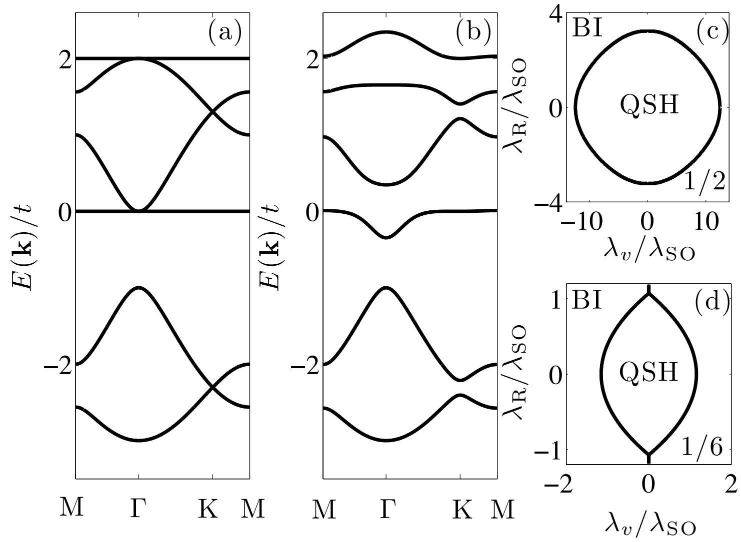

Figure 2.2: (a) and (b) show the band structure of the tight binding model $H_0 + H_{\mathrm{SO}}$ with $t = t'$ along the path shown in Fig. 2.1(c). In (a) $\lambda_{\mathrm{SO}} = 0$ and in (b) $\lambda_{\mathrm{SO}} = 0.1t$. There are Dirac points at K and K' (not shown) and quadratic band crossing points (QBCP) at Γ in (a), while in (b) $\lambda_{\mathrm{SO}} \neq 0$ opens up a gap at each of these points and destroys the flat bands. (c) The phase diagram at $f = 1/2$ (involving QBCP) with $\lambda_{\mathrm{SO}} = 0.1t$. (d) The phase diagram at $f = 1/6$ (involving Dirac points) for $\lambda_{\mathrm{SO}} = 0.1t$. We have chosen a staggered sublattice potential configuration where all the sites in A(B)-triangle (see Fig. 2.1) have potentials λ_v ($-\lambda_v$).

are Dirac points at K and K', two quadratic band crossing points (QBCP) at Γ, and two flat bands present when $\lambda_{\mathrm{SO}} = 0$. We note that the lower QBCP appears at filling fraction $f = 1/2$ for $t' < 3t/2$ and at $f = 1/3$ for $t' > 3t/2$. Similar band features are also found on the kagome lattice at the same Brillouin zone points[33, 42]. When the second neighbor hopping $\lambda_{\mathrm{SO}} \neq 0$, a gap opens at the Dirac and the QBCP and topologically non-trivial phases appear; denoted as quantum spin Hall (QSH) insulator in Figs. 2.2 and 2.3. By explicitly computing the Z_2 invariant using the parity eigenvalues at the time-reversal invariant moment[26] and checking for helical edge states in a strip geometry[3], we have found the phase diagrams for different filling fractions, f. The results are summarized in Fig. 2.3.

One feature of the decorated honeycomb lattice that differs from the kagome and honeycomb lattices is the natural presence of two (t and t'), rather than one,

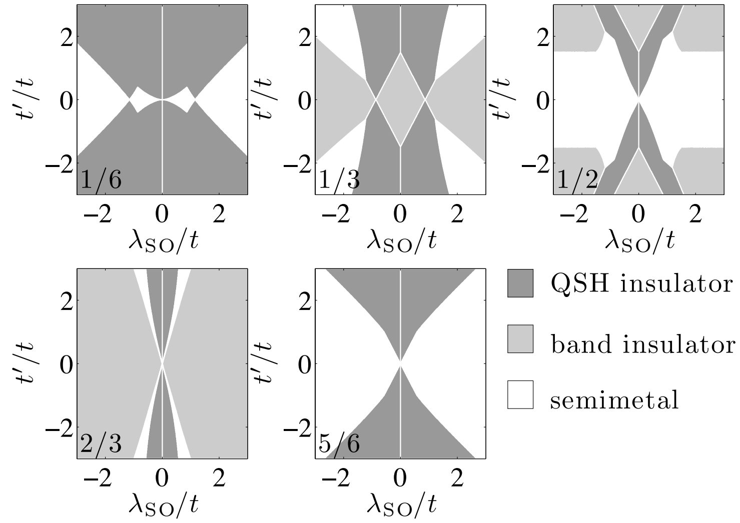

Figure 2.3: Phase diagrams for the decorated honeycomb lattice with t and t' real in the absence of a staggered on-site potential and no Rashba coupling. Several filling fractions f are shown (lower left corner). For fixed f and λ_{SO} it is possible to drive a transition between a topological insulator and a non-topological phase by varying the ratio t'/t.

nearest-neighbor hopping parameters. This effectively adds an additional degree of freedom to the phase diagram and can lead to transitions to topologically non-trivial phases even when there is not an *obvious* Dirac point or quadratic band crossing involved in the nearest-neighbor hopping model, such as occur at filling fraction 1/3 in Fig. 2.2(a). As Fig. 2.2(b) shows, when λ_{SO} is turned on, an "incipient" band touching point develops at the Γ point for filling fraction 1/3 and this effectively drives the transition to the topologically non-trivial state. Thus, the band structures with zero spin-orbit coupling do not always clearly reveal potential topological transitions for strong spin-orbit coupling.

At $f = 1/3, 1/2$, and $2/3$ there are (electron-hole compensated) intervening metallic phases between topologically trivial and non-trivial insulators. This also indicates that a "direct" transition coming from a band inversion is not generic in this model[44]. The filling fractions with such an intervening metallic phase mimic the behavior of disorder on the honeycomb lattice in the presence of finite Rashba coupling[45]. Also note that varying the ratio of t'/t at fixed λ_{SO} can lead to a transition between a TBI and a trivial insulator. More surprisingly, increasing λ_{SO} for fixed value of t'/t can trigger a transition between a TBI and a trivial insulator, as seen for $f = 1/3$ and $1/2$.

Next we turn to an analysis of the stability of the topological phases indicated in Fig. 2.3 in the presence of Rashba interaction and on-site (CDW) potentials. The stability of the topological phases at $f = 1/6$ and $f = 1/2$ is shown in Fig. 2.2 (c) and (d), where we used $\lambda_{vi} = \lambda_v$ on "sublattice" A and $\lambda_{vi} = -\lambda_v$ on "sublattice" B as shown in Fig. 2.1. Consequently, the stability regions are qualitatively similar to the analogous model on the honeycomb lattice[3, 46]. The stability region of the QBCP at $f = 1/2$ is larger than that for the Dirac point at $f = 1/6$, which we attribute to a larger value of the gap ($\sim$3 times) at the QBCP when $\lambda_R = \lambda_v = 0$[47].

2.4 Effective low energy description at Dirac points

At the Dirac points it is straightforward to derive an effective low energy description for arbitrary λ_{vi} in the 6-site unit cell. Setting the zero of energy to be right at the Dirac point (either at $f = 1/6$ or $f = 2/3$) for $\lambda_{\text{SO}} = \lambda_R = \lambda_{vi} = 0$, the effective low-energy Hamiltonian is given by

$$H' = H'_0 + H'_{\text{SO}} + H'_{\text{R}} + H'_{\text{CDW}} \tag{2.6}$$

with

$$\begin{aligned} H'_0 &= \alpha v_F \hbar (k_x \tau_z \sigma_x + k_y \sigma_y), && (2.7) \\ H'_{\text{SO}} &= -4\alpha\, w(t'/t)\, \lambda_{\text{SO}} \sigma_z \tau_z s_z, && (2.8) \\ H'_{\text{R}} &= -\alpha\, w_R(t'/t)\, \lambda_R (\sigma_x \tau_z s_y - \sigma_y s_x), && (2.9) \\ H'_{\text{CDW}} &= g_0 I + \alpha (g_x \sigma_x + g_y \tau_z \sigma_y + g_z \sigma_z). && (2.10) \end{aligned}$$

We have adopted a τ_z, σ_i, s_i notation similar to Ref. [4]: The $\tau_z = \pm 1$ describes states at either the K or K' points, the $\sigma_z = \pm 1$ describes the two bands that are involved in the Dirac band crossing (analog of A and B sublattice bands on the honeycomb lattice), and $s_z = \pm 1$ represents the electron spin as it did in Eq. (2.3) and Eq. (2.5). The parameter $\alpha = \pm 1$ refers to the Dirac point at $f = 1/6$, and $f = 2/3$, respectively. We have also defined two functions describing the dependence of the effective low-energy theory on the parameter $x = t'/t$:

$$\begin{aligned} w(x) &= \frac{\sqrt{3}|x|}{2\sqrt{9+4x^2}}, \\ w_R(x) &= \frac{3+2\sqrt{3}x}{\sqrt{9+4x^2}}. \end{aligned}$$

The effective Fermi velocity entering Eq. (2.7) is

$$v_F = w(t'/t)v_0$$

where $v_0 = ta/\hbar$ and a is the length of the unit cell vector. It follows from Eq. (2.9) that for $\lambda_{vi} = \lambda_{\rm R} = 0$ the spin-orbit coupling opens up a gap with magnitude $E_{\rm gap} = 8|w(t'/t)\lambda_{\rm SO}|$. The parameters entering the low-energy description of the CDW term, Eq. (2.10), are given by

$$\begin{aligned}
g_0 &= \frac{\lambda_{v1}+\lambda_{v2}+\lambda_{v3}+\lambda_{v4}+\lambda_{v5}+\lambda_{v6}}{6}, \\
g_x &= w\left(t'/t\right)\frac{\lambda_{v1}+\lambda_{v2}-2\lambda_{v3}+\lambda_{v4}+\lambda_{v5}-2\lambda_{v6}}{3\sqrt{3}}, \\
g_y &= w\left(t'/t\right)\frac{-\lambda_{v1}+\lambda_{v2}-\lambda_{v4}+\lambda_{v5}}{3}, \\
g_z &= w\left(t'/t\right)\frac{-\lambda_{v1}-\lambda_{v2}-\lambda_{v3}+\lambda_{v4}+\lambda_{v5}+\lambda_{v6}}{\sqrt{3}(t'/t)}.
\end{aligned}$$

A finite g_0 can be absorbed in a shift of the chemical potential.

It is useful to consider a few important limits of the general low-energy form of $H_{\rm CDW}$. First take $\lambda_{vi} = \lambda_v$ for sites on the A-triangle and $\lambda_{vi} = -\lambda_v$ for sites on the B-triangle. In this case,

$$H_{\rm CDW} = -\alpha\frac{2\sqrt{3}w(\frac{t'}{t})\lambda_v}{t'/t}\sigma_z,$$

which is identical to the form of the expression for the honeycomb lattice and will generically open a gap at the Dirac point[3]. We have verified that the low-energy description given above produces the same stability phase diagram and phase boundary shown in Fig. 2.2(d) as a direct diagonalization of the full 6-band

Hamiltonian. Another important limit to consider is that of general λ_{vi}. In that case, the physics more closely resembles the kagome lattice where an effective axial gauge field appears [33] with

$$\begin{aligned}\mathscr{A}_x^l &= -\frac{\lambda_{v1}+\lambda_{v2}-2\lambda_{v3}+\lambda_{v4}+\lambda_{v5}-2\lambda_{v6}}{3\sqrt{3}}l,\\ \mathscr{A}_y^l &= \frac{\lambda_{v1}-\lambda_{v2}+\lambda_{v4}-\lambda_{v5}}{3}l\end{aligned}$$

when $\lambda_{v1}+\lambda_{v2}+\lambda_{v3}-\lambda_{v4}-\lambda_{v5}-\lambda_{v6}=0$, where $l=\pm1$ refers to the two Dirac points K and K'. If, on the other hand, $\lambda_{v1}+\lambda_{v2}+\lambda_{v3}-\lambda_{v4}-\lambda_{v5}-\lambda_{v6}\neq 0$ a gap

$$E_{\text{gap}} = \frac{|\lambda_{v1}+\lambda_{v2}+\lambda_{v3}-\lambda_{v4}-\lambda_{v5}-\lambda_{v6}|}{\sqrt{9+4(t'/t)^2}}$$

opens with a smallest direct gap at shift $\mathscr{A}_x^l, \mathscr{A}_y^l$ with respect to K or K'. Thus, the behavior of the decorated honeycomb lattice with respect to H_{CDW} is another example of the ways in which this lattice "interpolates" between the honeycomb and kagome lattices, and we expect, for example, analogs of the kekule phase to be realized as well[33, 48].

2.5 Adiabatic deformations and the Kitaev model

We now turn our attention to one of the features of the decorated honeycomb lattice which is related to its geometry: Topological phases exist *even in the absence of second neighbor hopping* when t is made complex (obtained by putting a flux through the vertex triangles). Below we show by an explicit calculation for spinless fermions that the model obtained in the absence of second neighbor hopping but with complex t (and possibly also complex t') can be adiabatically deformed into a model with real t, t' and λ_{SO}. An example of such an adiabatic deformation is illustrated in Fig. 2.4 and in the last part of this section we will describe each step of the deformation in detail.

The adiabatic connection we establish also holds for time reversal invariant models of electrons with spin: For s_z conserving models on the honeycomb lattice, Kane and Mele showed [3, 4] that one can view a Z_2 TBI in 2-d as two copies of Haldane's model [14] with different effective magnetic fluxes (with a net zero flux through the unit cell) for different spins (so that under time-reversal each copy is transformed into the other, thus preserving TRS overall). Moreover, as long as the gap does not close, s_z non-conserving terms are also allowed. With this insight, it is evident that any lattice model that supports a quantum Hall effect for spinless fermions will support a Z_2 TBI for electrons with spin (by taking the appropriate "second copy").

There is an interesting consequence of the above mentioned adiabatic connection. It allows us to topologically relate the phases in the non-interacting tight-binding model at half-filling, see Fig. 2.3, to the chiral spin liquid phases recently reported in the Kitaev model[17, 32] on the same lattice which can be viewed as a *strongly interacting* electron model with spin-orbit coupling[49]. The Kitaev model on the decorated honeycomb lattice is defined in the following way[17, 50]

$$\begin{aligned}\mathscr{H} &= \sum_{x\text{-link}} J_x \sigma_i^x \sigma_j^x + \sum_{y\text{-link}} J_y \sigma_i^y \sigma_j^y + \sum_{z\text{-link}} J_z \sigma_i^z \sigma_j^z \\ &\quad + \sum_{x'\text{-link}} J'_x \sigma_i^x \sigma_j^x + \sum_{y'\text{-link}} J'_y \sigma_i^y \sigma_j^y + \sum_{z'\text{-link}} J'_z \sigma_i^z \sigma_j^z.\end{aligned}$$

In the summation, i and j are nearest neighboring sites connected by a α-link ($\alpha = x, y, z, x', y', z'$) as shown in Fig. 2.1(a). After a Jordan-Wigner transformation this model can be mapped onto a model of free majorana fermions hopping in the background of static Z_2 fluxes. The ground state spontaneously breaks time-reversal symmetry and is described by a chiral spin liquid with either Abelian or non-Abelian vortex excitations[17]. In the following we set $J_x = J_y = J_z = J > 0$ and $J'_x = J'_y = J'_z = J' > 0$. The ground-state sector corresponds to a uniform flux configuration. It possesses a representative free fermion model[43],

$$H_{\mathrm{CSL}} = \gamma \sum_{\mathbf{k}} \psi^{\dagger}_{\mathbf{k}\alpha} H^{(\mathrm{o})}_{\alpha\beta}(\mathbf{k}) \psi_{\mathbf{k}\beta} \tag{2.11}$$

and $\gamma = \pm 1$ specifies the way the time reversal symmetry is spontaneously broken. Here, $\psi^{(\dagger)}_{\mathbf{k}\alpha}$, $\alpha = 1, \ldots, 6$ are fermionic annihilation (creation) operators and we have

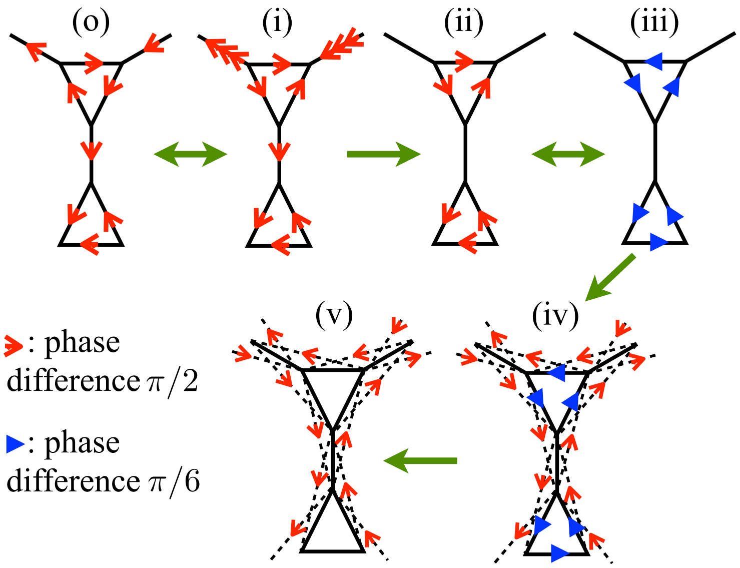

Figure 2.4: Schematic illustration of the continuous path which adiabatically connects the model (o) and (i) lacking second neighbor hopping but having complex t (the representative free fermion model of the ground state sector of the Kitaev model on the decorated Honeycomb lattice) with the spinless model (v) with real t, t' and λ_{SO}, denoted by (v). Along this path, the continuous deformation does not lead to a gap closing and the Chern number stays constant. This establishes the topological connection between the two models.

defined the matrix

$$
H^{(\mathrm{o})} =
\begin{pmatrix}
0 & iJ & iJ & -iJ'e^{-ik_2} & 0 & 0 \\
-iJ & 0 & -iJ & 0 & iJ'e^{ik_1} & 0 \\
-iJ & iJ & 0 & 0 & 0 & iJ' \\
iJ'e^{ik_2} & 0 & 0 & 0 & iJ & -iJ \\
0 & -iJ'e^{-ik_1} & 0 & -iJ & 0 & iJ \\
0 & 0 & -iJ' & iJ & -iJ & 0
\end{pmatrix}.
$$

The flux pattern derived from the matrix $H^{(\mathrm{o})}$ is illustrated in (o) of Fig. 2.4. The spectrum of Eq. (2.11) is gapped at half filling as long as $J' \neq \sqrt{3}J$ and the Chern number is $\nu = -\gamma$ for $J' < \sqrt{3}J$ and $\nu = 0$ for $J' > \sqrt{3}J$[17]. The two sectors connected by time reversal symmetry and characterized by the parameter $\gamma = \pm 1$ are similar to the two “copies” characterized by $s_z = \pm 1$ in the Kane-Mele type model. However, in the strongly interacting limit (Kitaev model) the system spontaneously chooses one sector whereas the non-interacting TBI model involves a summation over the two sectors (spin).

We now discuss the adiabatic connection of the model $H^{(\mathrm{o})}$ to the spinless model with real t, t' and λ_{SO}; model $H^{(\mathrm{v})}$ in Fig. 2.4. As the starting point for the continuous deformation we use a gauge equivalent pattern (i) obtained from (o) by replacing $\psi_{\mathbf{k}4} \to -\psi_{\mathbf{k}4}$ and $\psi_{\mathbf{k}5} \to -\psi_{\mathbf{k}5}$. From (i) to (ii) the phase difference for hopping between the triangles is gradually reduced to zero. This can be achieved by replacing $\pm iJ'$ in $H^{(\mathrm{i})}$ by $\exp(\pm is\pi)J'$ and continuously reducing s from 1 to 0. This process does not change the fluxes through the triangles and the dodecagons; instead the global fluxes are modified and the whole spectrum is moved in **k**-space according to $k_1 \to k_1 + (1-s)\pi$ and $k_2 \to k_2$. Consequently, the direct gap stays constant. From (ii) to (iii) a continuous gauge transformation is applied to change the phase difference for hopping within the triangles from $\pm\pi/2$ to $\pi/6$ (this does not modify any flux and the gap remains constant). From (iii) to (v) we turn on $\lambda_{\rm SO}$ as shown in (iv) and make t real. Along this path the value of the gap varies in general. Explicitly, we can define the set of matrices

$$\Gamma(\phi,\lambda_{\rm SO}) = \begin{pmatrix} 0 & e^{-i\phi}J & e^{i\phi}J & J'e^{-ik_2} & D & -E \\ e^{i\phi}J & 0 & e^{-i\phi}J & -D & J'e^{ik_1} & F \\ e^{-i\phi}J & e^{i\phi}J & 0 & E & -F & J' \\ J'e^{ik_2} & -D^* & E^* & 0 & e^{-i\phi}J & e^{i\phi}J \\ D^* & J'e^{-ik_1} & -F^* & e^{i\phi}J & 0 & e^{-i\phi}J \\ -E^* & F^* & J' & e^{-i\phi}J & e^{i\phi}J & 0 \end{pmatrix}.$$

Here we have introduced

$$\begin{aligned} D &= -i\lambda_{\rm SO}\left(e^{-ik_1}+e^{-ik_2}\right), \\ E &= -i\lambda_{\rm SO}\left(1+e^{-ik_1}\right), \\ F &= -i\lambda_{\rm SO}\left(1+e^{-ik_2}\right). \end{aligned}$$

Clearly, $\Gamma(\pi/6,0) = H^{\rm (iii)}$ and $\Gamma(0,\lambda_{\rm SO}) = H^{\rm (v)}$. By numerical examination of the gap and of the Chern number[51] at half-filling we find that there is a large range of parameters which allows one to adiabatically connect the model (iii) with the model (v). This is shown in Fig. 2.5 where we plot the Chern number in (a) and the value of the gap in (b) obtained for $J = J'$.

The model defined by $\Gamma(\phi, \lambda_{\mathrm{SO}})$ shows a complex phase diagram with a variety of topological phases distinguished by different values of the Chern number. As long as there is a direct gap, the Chern number is well-defined and regions with different values are necessarily separated by gap closings. However, there are also regions in parameter space where an indirect gap is closed indicating the presence of partially filled bands at half-filling, see Fig. 2.5(b). The phase diagram of $\Gamma(\phi, \lambda_{\mathrm{SO}})$ also depends on the ratio J'/J. For $J' > \sqrt{3}J$ the Chern number of $H^{(\mathrm{iii})}$ is zero and the connection (iii) to (v) holds between topologically trivial phases.

These arguments demonstrate the adiabatic connection between the strongly interacting chiral spin liquid phases of the Kitaev model and the phases obtained from the spinless model at half-filling with real t, t' and λ_{SO}. In this sense, we also establish a connection to the Z_2 TBI when two “copies” of the spinless model

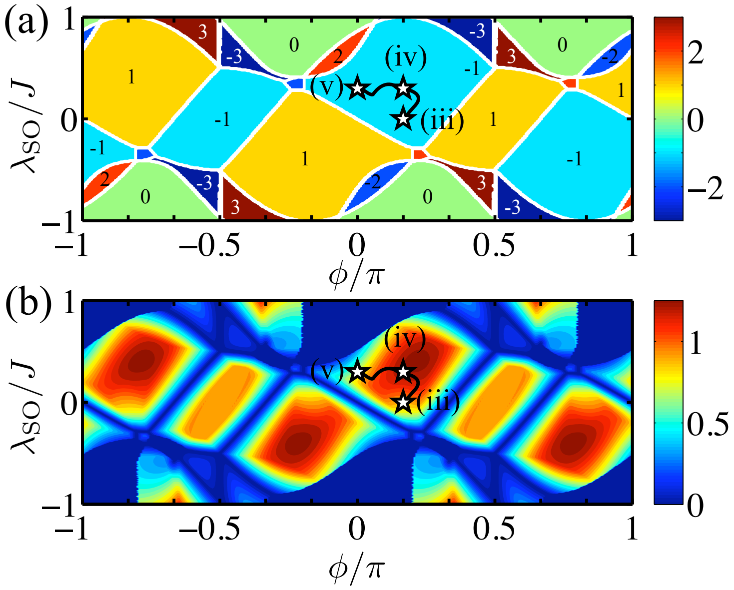

Figure 2.5: Contour plot of (a) the Chern number and (b) the gap of the model defined by $\Gamma(\phi, \lambda_{\mathrm{SO}})$ at half filling for $J = J'$. Also shown is a possible path which adiabatically connects the flux patterns (iii), (iv) and (v) defined in Fig. 2.4.

are taken. It can be shown that a generalized spin-3/2 Kitaev model on the kagome lattice also supports a chiral spin liquid ground state with non-Abelian excitations [52] and similar arguments can be made for connections to other topological phases[53, 54].

2.6 Summary

In summary, we have shown that the decorated honeycomb lattice supports Z_2 topological phases at various filling fractions, discussed their stability, and described the similarities and differences with the Z_2 topological phases on the kagome[33] and honeycomb lattices[3]. The limit of weak spin-orbit coupling yields phase diagrams which are very similar to the ones observed on the honeycomb or kagome lattice. This observation is in agreement with the conclusions drawn from the effective low-energy theory at the Dirac points. The situation for strong spin-orbit coupling can be quite different and leads to novel aspects. One surprising observation is that a large λ_{SO} can trigger a transition from a TBI to a trivial insulator.

We have also shown that the tight-binding models with real t, t' and λ_{SO} can be adiabatically connected to models without second-neighbor hopping but with complex t (and possibly also complex t'). This property was explicitly demonstrated at half filling by a calculation of the gap and the Chern number. Moreover, we have argued that this adiabatic connection allows us to topologically relate the chiral spin liquid phases recently discovered on the decorated honeycomb lattice to the phases obtained at half-filling in the non-interacting TBI model. Our work therefore provides an example of a non-interacting and a strongly interacting model defined on the same lattice which are both exactly solvable and show topologically related states. To determine the precise form of the spin-orbit interaction, the number, and the size (coupling strength) of the terms needed in a generalized extended Hubbard model at half filling to interpolate between the topological band insulator and the Kitaev model on the decorated honeycomb lattice is an interesting open problem beyond the scope of this work. However, based on our results here and related studies that realize Kitaev models in certain low energy limits[49, 55], we believe that such an interacting microscopic model can be found.

Finally, we note that an underlying "star" lattice has been experimentally reported for a polymeric Iron(III) acetate[56], and some of our results may be relevant for this solid state example of a decorated honeycomb lattice. We also believe it is possible to realize much of the discussed physics (including Kitaev models), in cold atomic gases, given that its two cousins, the honeycomb and kagome lattices, can be realized in optical lattices[57, 58].

Chapter 3

Interaction-driven Topological Insulators on the Kagome and the Decorated Honeycomb Lattices

3.1 Introduction

The study of topological properties of a quantum system with many degrees of freedom can provide insights into global features of ground states and can reveal physical behaviors which are robust against weak perturbations. While the terminology of *topological order* has been used to describe different aspects of a quantum system with interactions [22–24], we will focus on topological properties which are stored in the set of single-particle wave functions describing band structures of materials with a bulk gap. One famous example is the integer quantum Hall effect where the topological property is encapsulated in an integer called the *Chern number*. It has been shown that the Chern number is directly related to quantized values of the Hall conductivity[1]. A nonzero Chern number requires the breaking of time-reversal symmetry either by an external magnetic field or, in the absent of a net magnetic flux through a unit cell, by microscopically circling currents[14].

Breaking of time-reversal symmetry is not necessarily required to define topological invariants which distinguish different bulk insulators (or superconductors). Based on the random matrix theory, a comprehensive classification scheme for non-interacting systems has been worked out[59]. Among all classifications, *topological insulators* (TIs) with time-reversal symmetry have raised considerable interest in recent years (see Refs. [6–8]). TIs are well described by conventional band theory. However, they are a distinct phase of matter with bulk energy gaps and an odd number of time-reversal symmetry protected gapless modes on their edge (surface in three dimensions)[3–5]. In two dimensions, it is also termed the *quantum spin Hall state* (QSH). This state is distinct from ordinary insulators by a nonzero value of a Z_2 invariant[3, 4]. In three dimensions, there are four Z_2 invariants characterizing either a strong topological insulator, a weak topological insulator, or a trivial insulator[5, 60, 61]. The Z_2 invariants can be obtained via knowledge of the single-particle wave functions alone.

The key to experimental realizations of TIs (at least so far) is strong intrinsic spin-orbit interaction originating from relativistic effects. The topologically nontrivial behavior in these systems is stabilized by a strong spin-orbit coupling which leads to a “band inversion”[10, 25, 44]. While the experimental search for the TIs in real materials with strong spin-orbit coupling is still under way with a number of examples found to date[11–13, 29–31, 62, 63], the current theoretical research in TIs is quite diverse. On the one hand, there have been intensive first-principle studies to identify potential candidate materials for TIs[28, 64–67]. On the other hand, the study of TIs in the presence of disorder [68, 69] and interplay of spin-orbit coupling and electron-electron interaction [41, 70] have been carried out. New exotic phases have been proposed, such as a *topological Mott insulator*[41], which has a gapped charge sector but gapless spinon excitations on the boundary.

In this chapter, we focus on yet another class of systems in which the topologically nontrivial nature of the wave functions is a result of spontaneously broken symmetry in an interacting system[37, 38, 47]. These *interaction-driven topological insulators* possess conventional order parameters and the topological order is locked to those. Microscopically, the topological phases are described by the spontaneous generation of (spin) currents, a popular theoretical idea which has been used in many variants for describing the pseudogap phase of the cuprates[71–74]. However, in contrast to these cuprate models defined on the square lattice, a gap can be opened over the whole Brillouin zone in certain other lattices[37, 38, 42, 47] allowing one to characterize the phase by a topological invariant. For example, in Ref. [42] a double-exchange ferromagnet has been studied on the kagome lattice and the ground state has been described as a chiral spin state with a finite Chern number. Later, Raghu *et al.* studied an extended Hubbard model on the honeycomb lattice and showed that both a quantum anomalous Hall phase and a quantum spin Hall phase can be generated dynamically[37]. A similar idea has also been used to obtain a three-dimensional example of an interaction-driven topological insulator on the diamond lattice[38].

In this chapter, we study spinless and spinful extended Hubbard models with repulsive interactions on the kagome and decorated honeycomb lattice. Interacting electrons on the kagome lattice provide a model system where ferromagnetism can be rigorously shown for certain parameters (*flat-band*[75, 76] and *kinetic*[77] ferromagnetism). Furthermore, the Mott transition in the standard Hubbard model defined on this lattice has been studied[78]. In addition to these examples, a great deal of the theoretical work on Hubbard and extended Hubbard models has focused on the case of half-filling where the low-energy degrees of freedom are described by a frustrated quantum spin model[79–82]. These studies are motivated in part by the recent discovery that herbertsmithite, a spin-1/2 kagome antiferromagnet, might support a spin liquid ground state[83, 84]. Another system where the physics of interacting electrons on the kagome lattice might be important is $\mathrm{Na}_x\mathrm{CoO}_2$ where the orbital degrees of freedom give rise to four interpenetrating kagome systems[85, 86].

The decorated honeycomb lattice can be viewed as an interpolating lattice between honeycomb and kagome. While there are few known examples of this lattice in nature[56], the exact ground states of the Kitaev model on this lattice have been found by Yao *et.al* [17] and other higher symmetry spin models have been studied as well[87]. Yao has shown that the exact ground state of the Kitaev model on this lattice is a chiral spin liquid that spontaneously breaks time-reversal symmetry [17]. There are two topologically distinct chiral spin liquid phases: (i) a topologically nontrivial phase with odd Chern number and non-abelian vortex excitations and (ii) a topologically-trivial phase with even Chern number and abelian vortex excitations. In our previous work [16], we have found that this lattice also supports a TI phase in the presence of spin-orbit coupling at various filling fractions, and we established a connection between the topologically nontrivial chiral spin liquid state of the Kitaev model (appropriate for strongly interacting electrons with spin-orbit coupling) and the ground state of Z_2 topological band insulators (studied in the noninteracting limit).

Both the kagome and decorated honeycomb lattices support a TI in a single-orbital tight-binding model with spin-orbit coupling[16, 33]. In this paper we show that a TI (quantum anomalous Hall state for the spinless case) can also be interaction-driven on both lattices. We focus on filling fractions which either involve a pair of Dirac points ($1/3$ filling in the kagome system) or a quadratic band crossing point ($2/3$ filling in the kagome and $1/2$ filling in the decorated honeycomb system) in the noninteracting tight-binding model[54]. Using a Hartree-Fock mean-field approach, we discuss various possible symmetry broken states, present the phase diagrams and highlight the competition between various states. We find pronounced differences for different filling fractions. In particular, a topologically nontrivial phase is the leading instability at $2/3$ filling on the kagome lattice and 1/2 filling on the decorated honeycomb lattice. On the other hand, to stabilize a topologically nontrivial phase at $1/3$ filling on the kagome lattice, some fine tuning of the interaction parameters is required. We also point out that the kagome and decorated honeycomb lattices provide examples where topological phases can emerge solely due to a complex nearest neighbor hopping, in contrast to the honeycomb or diamond lattice in which a complex second neighbor hopping is required, at least within a single band model.

This chapter is organized as follows. In Sec. 3.2, we introduce spinless and spinful extended Hubbard models on the kagome and decorated honeycomb lattices, and review the tight-binding band structures and Hartree-Fock mean-field approach for the implementation of numerical calculations. In Sec. 3.3 and 3.4, we discuss several symmetry-breaking candidate phases and present phase diagrams of spinless and spinful extended Hubbard models at $1/3$ and $2/3$ filling fractions. We find the topologically nontrivial phases can be stabilized under suitable circumstances. Comparisons are also made to related work. Then, in Sec. 3.5 we briefly discuss the spinless extended Hubbard model on the decorated honeycomb lattice. Finally, we present our conclusions and summary in Sec. 3.6.

3.2 Models and Methods

We first introduce the models which will be studied later by means of the Hartree-Fock approximation. We consider both spinless (spin-polarized) and spinful interacting fermions in a single-orbital Hamiltonian on the kagome and the decorated honeycomb lattice.

3.2.1 Extended Hubbard models

The lattice model under consideration for spinless (spin-polarized) fermions takes the form

$$\begin{aligned} H_{\text{spinless}} &= -t \sum_{\langle i,j \rangle} c_i^\dagger c_j + V_1 \sum_{\langle i,j \rangle} n_i n_j \\ &+ V_2 \sum_{\langle\langle i,j \rangle\rangle} n_i n_j + V_3 \sum_{\langle\langle\langle i,j \rangle\rangle\rangle} n_i n_j . \end{aligned} \tag{3.1}$$

Here, $c_i^{(\dagger)}$ annihilates (creates) a spinless fermion on site i and $n_i = c_i^\dagger c_i$ is the fermion density operator on site i. The sums run over nearest-neighbor $\langle i,j \rangle$, second-neighbor $\langle\langle i,j \rangle\rangle$, or third-neighbor bonds $\langle\langle\langle i,j \rangle\rangle\rangle$. The hopping amplitude is denoted by t and the parameters V_1, V_2, and V_3 quantify the nearest-neighbor, second-neighbor and third-neighbor repulsion, respectively. For most parts of our work we set $V_3 = 0$. However, as we show later, a small but finite V_3 is necessary to stabilize a topologically non-trivial insulator for $1/3$ filling fraction on the kagome lattice.

The model for spinful fermions includes an additional on-site repulsive interaction U. The Hamiltonian reads

$$\begin{aligned} H_{\text{spinful}} = -t \sum_{\langle i,j \rangle} c^{\dagger}_{i\sigma} c_{j\sigma} + U \sum_{i} n_{i\uparrow} n_{i\downarrow} \\ + V_1 \sum_{\langle i,j \rangle} n_i n_j + V_2 \sum_{\langle\langle i,j \rangle\rangle} n_i n_j + V_3 \sum_{\langle\langle\langle i,j \rangle\rangle\rangle} n_i n_j. \end{aligned} \tag{3.2}$$

Here, $c^{(\dagger)}_{i\sigma}$ annihilates (creates) a fermion on site i with spin $\sigma = \uparrow, \downarrow$, $n_{i\sigma} = c^{\dagger}_{i\sigma} c_{i\sigma}$ and $n_i = \sum_{\sigma} n_{i\sigma}$. The summing convention and the meaning of the parameters V_1, V_2, and V_3 are the same as for the spinless model.

3.2.2 Kagome and decorated honeycomb lattice

The models in Eqs. (3.1) and (3.2) have been studied on the kagome and the decorated honeycomb lattice in the non-interacting limit[16, 33]. A section of the kagome lattice is shown in Fig. 3.1 and a section of the decorated honeycomb lattice is shown in Fig. 3.11. Both lattices share an underlying triangular lattice and we choose the unit cell vectors to be

$$a_1 = (a, 0) \quad \text{and} \quad a_2 = (\frac{a}{2}, \frac{\sqrt{3}}{2} a), \tag{3.3}$$

where a is their length. The kagome lattice has three sites in the unit cell whereas the decorated honeycomb lattice has six. The reciprocal lattice vectors are given by

$$b_1 = \frac{2\pi}{a}(1, \frac{-1}{\sqrt{3}}) \quad \text{and} \quad b_2 = \frac{2\pi}{a}(0, \frac{2}{\sqrt{3}}). \tag{3.4}$$

The first Brillouin zone forms a hexagon in momentum space for both lattices, similar to the honeycomb lattice which also shares the underlying triangular lattice.

Tight-binding band structure on kagome lattice

The noninteracting energy dispersion for a nearest-neighbor tight-binding model [first term in Eq. (3.1)] can be obtained analytically. On the kagome lattice, three bands are found with the following dispersion relation:

$$\varepsilon_1(k) = -t - tA_k, \quad \varepsilon_2(k) = -t + tA_k, \quad \varepsilon_3(k) = 2t. \tag{3.5}$$

In Eq. (3.5) we have defined

$$A_k = \sqrt{3 + 2\cos k_1 + 2\cos k_2 + 2\cos(k_1 - k_2)}, \tag{3.6}$$

where $k_1 = a_1 \cdot k$ and $k_2 = a_2 \cdot k$. There are two dispersing bands ($n = 1$ and 2) and a flat band ($n = 3$). At filling fraction $f = 1/3$, the two dispersing bands touch at two inequivalent Dirac points located at corners of the Brillouin zone

$$K_\pm = \pm(b_1 - b_2)/3. \tag{3.7}$$

At filling fraction $f = 2/3$, the second band touches the flat band at the Γ point [$k = (0,0)$]. This is a quadratic band crossing point (QBCP)[47]. Upon inclusion of an intrinsic spin-orbit coupling (modeled by a spin-dependent imaginary second-neighbor hopping) one finds that a gap is opened both at the Dirac points ($f = 1/3$) and the QBCP ($f = 2/3$)[33]. The resulting insulating state at $f = 1/3$ and $f = 2/3$ is a Z_2 topological insulator with time-reversal symmetry protected edge states[33]. In the following sections, we explore the possibility of dynamically generating a topological insulator phase from interactions and study its competition with other broken-symmetry phases. We therefore focus on $f = 1/3$ and $f = 2/3$ in this paper.

Tight-binding band structure on decorated honeycomb lattice

Diagonalization of the noninteracting tight-binding model on the decorated honeycomb lattice gives the following six bands:

$$\varepsilon_1(k) = -\frac{t}{2} - \sqrt{\frac{9}{4}t^2 + t'^2 + tt'A_k}, \tag{3.8a}$$

$$\varepsilon_2(k) = -\frac{t}{2} - \sqrt{\frac{9}{4}t^2 + t'^2 - tt'A_k}, \tag{3.8b}$$

$$\varepsilon_3(k) = t - t', \tag{3.8c}$$

$$\varepsilon_4(k) = -\frac{t}{2} + \sqrt{\frac{9}{4}t^2 + t'^2 - tt'A_k}, \tag{3.8d}$$

$$\varepsilon_5(k) = -\frac{t}{2} + \sqrt{\frac{9}{4}t^2 + t'^2 + tt'A_k}, \tag{3.8e}$$

$$\varepsilon_6(k) = t + t', \tag{3.8f}$$

and A_k is defined in Eq. (3.6). Here, we have introduced independent hopping amplitudes for hopping within a triangle (t) and between triangles (t')[16]. There are two flat bands ($n = 3, 6$) and four dispersing bands ($n = 1, 2, 4, 5$). For filling fractions $1/6$ and $2/3$, there are Dirac points located at $K_\pm$ in the momentum space. There are also two quadratic band touching points at $k = (0, 0)$. The lower QBCP appears at $f = 1/2$ if $t' < 3t/2$ and at $f = 1/3$ if $t' > 3t/2$. The upper QBCP appears at $f = 5/6$. In the presence of a spin-orbit coupling, TI phases are found at various filling fractions[16]. In this paper we set $t = t'$ and solely focus on $f = 1/2$. Half filling is of particular interest because a topological connection between the chiral spin liquid states recently found in the Kitaev model[17] and the Z_2 topological band insulator has been established[16].

3.2.3 Hartree-Fock mean-field approximation

We use the standard Hartree-Fock mean-field approach to decouple the interaction terms in Eqs. (3.1) and (3.2). In contrast to comparable studies on the honeycomb lattice[37, 88] and the diamond lattice[38], we treat the Hartree and Fock terms on equal footing in all phases.

Hartree-Fock approximation in the spinless models

For spinless fermions, we decouple the interaction both in the direct and the exchange channel:

$$\begin{aligned} n_i n_j &\approx n_i \langle n_j \rangle + \langle n_i \rangle n_j - \langle n_i \rangle \langle n_j \rangle \\ &\quad - c_i^\dagger c_j \langle c_j^\dagger c_i \rangle - \langle c_i^\dagger c_j \rangle c_j^\dagger c_i + \langle c_i^\dagger c_j \rangle \langle c_j^\dagger c_i \rangle. \end{aligned} \tag{3.9}$$

This procedure yields a mean-field Hamiltonian which is bilinear in the fermionic operators and can be diagonalized. In the following, we focus on uniform phases which are characterized by a (possibly enlarged) unit cell. We work in the canonical ensemble with a fixed number of electrons N_e. The free energy at temperature $k_B T = \beta^{-1}$ is given by

$$\begin{aligned} F &= -k_B T \sum_{k,n} \log\left[1 + e^{\beta(E_{kn} - \mu)}\right] + \mu N_e \\ &+ V_1 \sum_{\langle i,j \rangle} \left(\langle c_i^\dagger c_j \rangle \langle c_j^\dagger c_i \rangle - \langle n_i \rangle \langle n_j \rangle \right) \\ &+ (V_2, V_3)\text{−terms}, \end{aligned} \tag{3.10}$$

where the chemical potential $\mu = \mu(T, N_e)$. The terms in the second and third line of Eq. (3.10) arise from $\langle n_i \rangle \langle n_j \rangle$ and $\langle c_i^\dagger c_j \rangle \langle c_j^\dagger c_i \rangle$ in the decoupling Eq. (3.9) and are not included in the single-particle energies E_{kn}. The most general self-consistency (mean-field) equations are

$$\frac{\partial F}{\partial \langle n_i \rangle} = \frac{\partial F}{\partial \langle c_i^\dagger c_j \rangle} = \frac{\partial F}{\partial \langle c_j^\dagger c_i \rangle} = 0. \tag{3.11}$$

In the following sections, we discuss various solutions of these equations.

Hartree-Fock approximation in the spinful models

For spinful fermions, we decouple the on-site interaction according to

$$\begin{aligned} n_{i\uparrow} n_{i\downarrow} \approx{}& n_{i\uparrow} \langle n_{i\downarrow} \rangle + \langle n_{i\uparrow} \rangle n_{i\downarrow} - \langle n_{i\uparrow} \rangle \langle n_{i\downarrow} \rangle \\ & - c_{i\uparrow}^\dagger c_{i\downarrow} \langle c_{i\downarrow}^\dagger c_{i\uparrow} \rangle - \langle c_{i\uparrow}^\dagger c_{i\downarrow} \rangle c_{i\downarrow}^\dagger c_{i\uparrow} + \langle c_{i\uparrow}^\dagger c_{i\downarrow} \rangle \langle c_{i\downarrow}^\dagger c_{i\uparrow} \rangle. \end{aligned} \tag{3.12}$$

We assume the mean-field solutions are described by a co-linear spin alignment and therefore, without loss of generality, we set $\langle c_{i\uparrow}^\dagger c_{i\downarrow} \rangle = \langle c_{i\downarrow}^\dagger c_{i\uparrow} \rangle = 0$ in what follows. For the model on the kagome lattice with $V_1 = V_2 = V_3 = 0$, and at filling fractions $f = 1/3$ and $f = 2/3$, we have explicitly checked that with *all* the terms (including $\langle c_{i\uparrow}^\dagger c_{i\downarrow} \rangle$) all our self-consistent solutions indeed have a co-linear spin alignment. We expect this property will persist also for finite further neighbor interactions. However, the $\langle c_{i\uparrow}^\dagger c_{i\downarrow} \rangle$ term has to be kept if one works at half filling on the kagome lattice where at the mean-field level a coplanar 120° antiferromagnetic state arises in the large U limit. The same antiferromagnetic state has also been found on the triangular lattice[89–91].

The further-neighbor interaction is decoupled in a similar way:

$$\begin{aligned} n_i n_j \;\approx\;& n_i\langle n_j\rangle + \langle n_i\rangle n_j - \langle n_i\rangle\langle n_j\rangle - \sum_{\alpha\beta}\Big(c^\dagger_{i\alpha} c_{j\beta} \langle c^\dagger_{j\beta} c_{i\alpha}\rangle \\ & + \langle c^\dagger_{i\alpha} c_{j\beta}\rangle c^\dagger_{j\beta} c_{i\alpha} - \langle c^\dagger_{i\alpha} c_{j\beta}\rangle\langle c^\dagger_{j\beta} c_{i\alpha}\rangle\Big)\,. \end{aligned} \tag{3.13}$$

Again, as mentioned above, we set $\langle c^\dagger_{i\alpha} c_{j\beta}\rangle = 0$ for $\alpha \neq \beta$ which is justified if the spin alignment is co-linear in the physical solutions. The structure of the free energy and the self-consistency equations are similar to Eqs. (3.10) and (3.11) for the spinless models.

3.3 Spinless fermions on kagome lattice

In this section we discuss the zero temperature Hartree-Fock mean-field phase diagrams at filling fractions $f = 1/3$ and $f = 2/3$ for the spinless model on the kagome lattice. We first introduce the candidate phases and then show the V_1-V_2 phase diagrams with and without a finite V_3 for the two special filling fractions. Because at $f = 1/3$ there are Dirac points involved, and at $f = 2/3$ there is a QBCP, the phase diagrams look rather different for these two cases.

3.3.1 Candidate phases

Let us now introduce possible candidate phases for the spinless model. Besides the topologically non-trivial quantum anomalous Hall (QAH) phase we also take into account possible charge density wave (CDW) patterns.

Quantum anomalous Hall phase

A complex Fock term in Eq. (3.9) breaks time-reversal symmetry and can give rise to a topological phase characterized by a non-vanishing Chern number[37] even though there is no external magnetic field. In the present case, the total flux through the unit cell must be zero (this follows from periodic boundary conditions on the unit cell). However, there are finite fluxes through the elementary loops and the system shows an integer quantum Hall effect. This is in full analogy to Haldane's model on the honeycomb lattice[14]. Such a state of matter is called a quantum anomalous Hall phase and a schematic illustration of its microscopic current pattern on the kagome lattice with finite V_1 and V_2 is shown in Fig. 3.1.

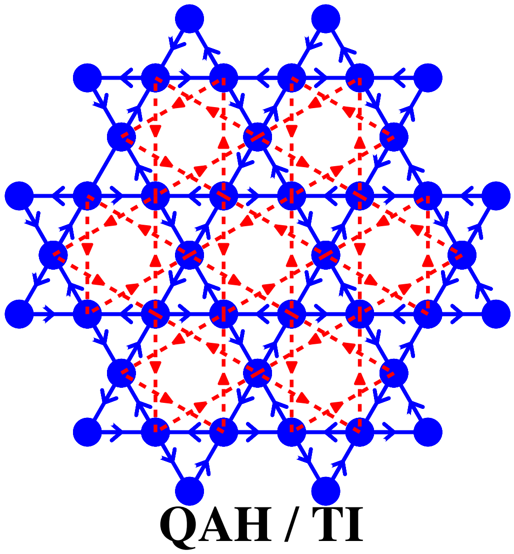

Figure 3.1: The spinless flux pattern developed by nearest and second nearest interactions that preserves lattice symmetry but spontaneously breaks time-reversal symmetry on the kagome lattice. Charges are uniform on all sites. The blue solid(red dash) line represents a (second)nearest neighbor complex hopping. For the spinful case, two copies of the same(opposite) flux patterns for spin-up and spin-down fermions form the quantum anomalous Hall (topological insulator) state.

The QAH phase preserves the translational symmetry of the noninteracting model but breaks time-reversal symmetry. A solution of the self-consistency Eqs. (3.11) is obtained by assuming a uniform charge distribution and introducing complex bond expectation values. For nearest neighbor bonds we make the following *ansatz*:

$$\langle c_i^\dagger c_j \rangle = \chi \exp(i\varphi_{ij}) = \chi_1 + i\chi_2. \tag{3.14}$$

A similar *ansatz* is also made for second-nearest neighbor bonds:

$$\langle c_i^\dagger c_j \rangle = \chi' \exp(i\varphi'_{ij}) = \chi'_1 + i\chi'_2. \tag{3.15}$$

There is a gauge freedom in choosing the phase factors φ_{ij} and φ'_{ij} because only the inclosed fluxes through elementary loops are gauge invariant. We choose a uniform gauge $\varphi_{ij}^{(\prime)} = \pm\varphi^{(\prime)}$ where the sign is fixed according to the dictions of the arrows in Fig. 3.1. We stress that on the kagome lattice a complex nearest-neighbor hopping can already stabilize a topologically non-trivial phase showing an integer quantum Hall effect. This possibility has been explored in a model of a ferromagnet with spin anisotropy[42]. Therefore, in contrast to the honeycomb[37, 88] and the diamond lattice[38], the nearest-neighbor interaction V_1 alone can in principle generate a QAH phase if the time reversal symmetry is spontaneously broken. Indeed, we show below that at $f = 2/3$ this is the case. However, at $f = 1/3$ we find it essential to have a finite V_2 and small V_3 in order to stabilize the QAH state.

Charge density waves

An effective way to lower the potential energy is to develop an inhomogeneous charge distribution. In the atomic limit $t = 0$ and in the absence of further neighbor interactions, $V_2 = V_3 = 0$, there is a macroscopically degenerate set of charge configurations which minimize the energy. At $f = 1/3$ ($f = 2/3$) these configurations obey the "one particle (hole) per triangle"- rule. A finite t lifts the degeneracy and in the limit $t/V_1 \ll 1$ the system is effectively described by a hardcore dimer model on the honeycomb lattice[77, 92, 93]. Its ground state is the "plaquette" phase with resonating plaquettes and a periodicity which triples the unit cell[94]. Physically, it is the ring exchange of order $|t|^3/V_1^2$ which stabilizes the plaquette phase. We also note that in the limit $t/V_1 \ll 1$ the system becomes particle-hole symmetric. This property is clearly lost for small to intermediate interactions, see below.

Further neighbor interactions $V_2, V_3 > 0$ lift the degeneracy of the charge configurations in the atomic limit. This fact complicates a mapping to an effective dimer model for finite t. In the following we study the mean-field solutions of a limited number of different classical charge distributions. Specifically, we consider three different charge density wave (CDW) patterns which we denote by I, II and III

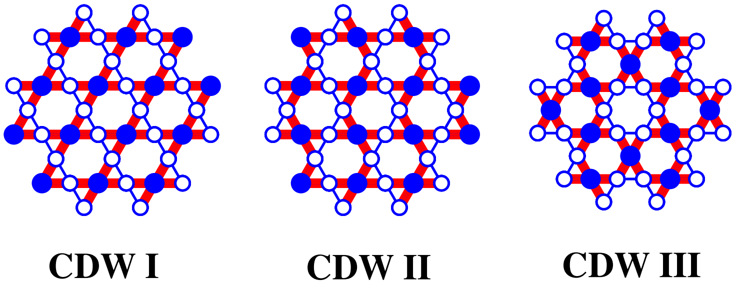

Figure 3.2: Three different charge density wave patterns on the kagome lattice studied in this paper. They are characterized by the wave vectors $q_{\mathrm{I}} = (0,0)$, $q_{\mathrm{II}} = b_2/2$ and $q_{\mathrm{III}} = (b_1 - b_2)/3$. Blue sites stand for the fermion-rich (poor) sites at 1/3 (2/3) filling fraction and white sites for the fermion-poor (rich) sites at 1/3 (2/3) filling fraction. The bond expectation values oscillate in the real space as well. We distinguish strong and weak bonds by thick and thin lines. For simplicity, we do not show the second neighbor bonds.

(see Fig. 3.2). They were introduced in Ref. [92] in order to numerically study the role of the ring exchange. For us it is important to realize that $V_2 > 0$ favors CDW I as compared to CDW II and III in the atomic limit. On the other hand, a third neighbor interaction $V_3 > 0$ favors CDW III over CDW I and CDW II. While the unit cell of pattern I is equal to the noninteracting unit cell, the unit cell of pattern II is doubled and the one of pattern III is tripled. Note that CDW III can be viewed as the classical charge distribution which corresponds to the plaquette phase of the effective dimer model in the limit $t/V_1 \ll 1$.

For the CDW I, the wave vector specifying its periodicity is $q_{\mathrm{I}} = (0,0)$ and the densities on the three inequivalent sites of the noninteracting unit cell are given by

$$\begin{aligned}
\langle n_1(r_{nm})\rangle_I &= f+\rho_1, \\
\langle n_2(r_{nm})\rangle_I &= f+\rho_2, \\
\langle n_3(r_{nm})\rangle_I &= f+\rho_3,
\end{aligned} \tag{3.16}$$

where $r_{nm} = na_1 + ma_2$ with $(n,m) \in \mathbb{Z} \times \mathbb{Z}$, f is the filling fraction and $\rho_1 + \rho_2 + \rho_3 = 0$. Similarly, the densities in the CDW II configuration can be written as

$$\begin{aligned}
\langle n_1(r_{nm})\rangle_{II} &= f+\rho_1 \cos(r_{nm}\cdot q_{II}), \\
\langle n_2(r_{nm})\rangle_{II} &= f+\rho_2 \cos(r_{nm}\cdot q_{II}), \\
\langle n_3(r_{nm})\rangle_{II} &= f+\rho_3 \cos(r_{nm}\cdot q_{II}),
\end{aligned} \tag{3.17}$$

where we have introduced the wave vector $q_{\mathrm{II}} = b_2/2$. In our mean-field calculations we find that mirror symmetric charge configurations are always favored. Such configurations are obtained by setting $\rho_1 = 2\rho$ and $\rho_2 = \rho_3 = -\rho$ (or cyclically permuted) in Eqs. (3.16) and (3.17). CDW I and II both break the six-fold rotations symmetry (C_6) of the kagome lattice; CDW I breaks it down to C_2, while CDW II breaks it down even further. In both cases, there are three different possibilities to choose a mirror symmetry plane. The CDW order parameter therefore has an additional Z_3 freedom.

Another phase with a mirror symmetric configuration of the densities in the non-interacting unit cell is described by the CDW III pattern:

$$\begin{aligned}
\langle n_1(r_{nm})\rangle_{III} &= f+2\rho\cos\left[r_{nm}\cdot q_{III}+s\frac{2\pi}{3}\right], \\
\langle n_2(r_{nm})\rangle_{III} &= f+2\rho\cos\left[r_{nm}\cdot q_{III}+(s-1)\frac{2\pi}{3}\right], \\
\langle n_3(r_{nm})\rangle_{III} &= f+2\rho\cos\left[r_{nm}\cdot q_{III}+(s+1)\frac{2\pi}{3}\right], \qquad (3.18)
\end{aligned}$$

where the wave vector is $q_{\mathrm{III}} = (b_1 - b_2)/3$. We have introduced the parameter $s = 0, 1, 2$ which characterizes the Z_3 freedom in the CDW III. Changing the value of s results in a shift of the pattern as a whole either by a_1 or a_2.

CDW I does not break the original translation symmetry and it can alternatively be viewed as a nematic phase[47]. The direction associated with the nematic order is given by

$$e = (Q_x, Q_y)/\sqrt{Q_x^2+Q_y^2}, \qquad (3.19)$$

where the components are obtained from the charge and bond order

$$\begin{aligned}
Q_x &= \frac{\langle n_1\rangle - \langle n_2\rangle}{\sqrt{3}} \pm 2\frac{\langle c_2^\dagger c_3\rangle - \langle c_1^\dagger c_3\rangle}{\sqrt{3}}, \qquad (3.20) \\
Q_y &= \frac{\langle n_1\rangle + \langle n_2\rangle - 2\langle n_3\rangle}{3} \pm 2\frac{\langle c_1^\dagger c_3\rangle + \langle c_2^\dagger c_3\rangle - 2\langle c_1^\dagger c_2\rangle}{3},
\end{aligned}$$

where the “$-$” sign refers to the case of 1/3 filling presently being considered, and the “$+$” sign refers to the case of 2/3 filling involving a quadratic band touching point. This definition of the nematic order parameter is in agreement with the definition given in Eq. (4) of Ref. [47] for the case of 2/3 filling.

In our study, we assume that the real hopping expectation values $\chi_{ij} = \langle c_i^\dagger c_j \rangle$ obey the same symmetry as the charge distribution. In Fig. 3.2, the weak and strong nearest-neighbor bonds are schematically shown. We find that taking into account this *bond order* can significantly lower the energy as compared to the case where only the Hartree term is kept. For the mirror symmetric solutions, the unit vector in Eq. (3.19) assumes only three different directions:

$$e_1 = (\sqrt{3}, 1)/2, \quad e_2 = (-\sqrt{3}, 1)/2, \quad e_3 = (0, -1). \tag{3.21}$$

These unit vectors will also appear in the low energy description of the CDW phases.

Other phases

Let us now briefly comment on other possible phases which are not stabilized in the present models. Dimerized and trimerized phases were considered in Ref. [33] as perturbations to the TI phase in the noninteracting limit. We find that for a self-consistency solution with dimerized or trimerized bonds, it is crucial to take into account the charge ordering which results from the bond order. However, our numerical results suggest that the charge density wave patterns shown in Fig. 3.2 (where the bond order has the same symmetry as the charge order) have lower energies than the dimerized or trimerized states. We also note that we do not find a mixed QAH and CDW phase on kagome lattice, which is in contrast to the findings on the checkerboard lattice[47].

3.3.2 Phase diagrams at $1/3$ filling fraction

Figure. 3.3 shows the V_1-V_2 phase diagrams for (a) $V_3 = 0$ and (b) $V_3 = 0.4t$. At $1/3$ filling, the noninteracting Fermi "surface" consists of a pair of Dirac points located at $K_\pm$ and the density of states vanishes linearly at the Fermi energy. As in related studies[37, 38], our mean-field calculations yield a stable semi-metallic (SM) phase for small to intermediate interactions which can be attributed to the absence of density of states at the Fermi level in the non-interacting limit.

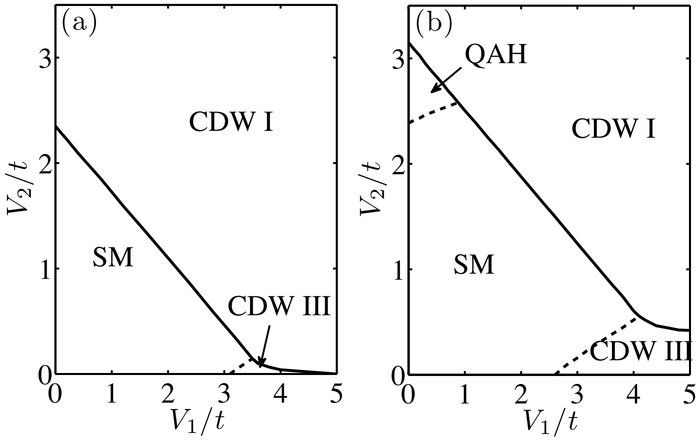

Figure 3.3: The phase diagram of the extended Hubbard model for spinless fermions at $1/3$ filling fraction on the kagome lattice. The third neighbor interaction is (a) $V_3 = 0$ and (b) $V_3 = 0.4t$. SM denotes the semi-metallic phase with two Dirac points, QAH denotes a time-reversal symmetry broken quantum anomalous Hall phase and CDW I and III are charge density waves with patterns shown in Fig. 3.2. Solid lines denote first and dashed lines second order transitions.

CDW phases and nematic order at $f = 1/3$

For large interactions, a CDW phase is stabilized. We find CDW I for large V_1 and V_2 because both the nearest neighbor and second neighbor interaction favors CDW I. The transition from the SM to the CDW I is first order which is different from the situation on the honeycomb lattice[37]. Below we discuss this aspect in more detail. On the other hand, CDW III is favored for small V_2 and large V_1. The transition from the SM to CDW III is second order.

The self-consistent CDW solutions at $f = 1/3$ are always gapped (this is in contrast to $f = 2/3$ where CDW phases with two nodes appear, see Sec. 3.3.3) and it is instructive to look at the corresponding low energy models. We first consider the possibility of a weak CDW I phase and then argue that it is energetically not favored. In fact, only for a large enough order parameter, does the CDW I solution have lower energy than the SM phase. For simplicity, we keep only the Hartree terms. In lowest order in $\bar{V}\rho$ ($\bar{V} = V_1 + V_2 - 2V_3$), the effective low energy Hamiltonian for the two nodes $l = \pm$ is given by

$$H_{\mathrm{I}} = v \sum_{k,l,\alpha,\beta} c^{\dagger}_{kl\alpha}[\tau \cdot (k - l\mathscr{A})]_{\alpha\beta} c_{kl\beta} + \frac{3v^2}{2\bar{V}} |\mathscr{A}|^2, \tag{3.22}$$

where the velocity is $v = \sqrt{3}ta/2$ and $\tau = (\tau_x, \tau_y)$ are Pauli matrices in the effective "sublattice" space. Furtherrmore, we have introduced an "axial gauge field"[33] $\mathscr{A}$ which can be expressed in terms of the CDW order parameter ρ and the vector e_n specifying the Z_3 freedom:

$$\mathscr{A} = -\frac{2\bar{V}}{v} \rho (\hat{n}_z \times e_n), \tag{3.23}$$

where the e_n are given by Eq. (3.21). This field shifts the position of the Dirac nodes with respect to their original position at $K_\pm$ and consequently, the CDW I described by Eq. (3.22) has nodes. However, Eq. (3.22) also includes the electron-electron interaction in the mean-field description which gives rise to the second term. This term is proportional to $v^2/\bar{V}$ and can be viewed as a mass-term for the gauge field. In other words, shifting the nodes by the vector $\mathscr{A}$ costs an energy proportional to $|\mathscr{A}|^2$. Therefore, it is energetically not favorable to built up a finite field $\mathscr{A}$ and the SM phase is stable. But once $\bar{V}$ is big enough, the description in terms of Eq. (3.22) breaks down. Solving the full self-consistency equations, we find a first order transition from the SM to the gapped CDW I phase.

Let us now consider CDW III which is stable for small V_2. The wave vector q_{III} of pattern III connects the two inequivalent Dirac points at $K_\pm$. From a weak-coupling point of view, CDW III therefore opens a gap by coupling the two Dirac points. This can be made explicit by studying the low energy mean-field Bloch Hamiltonian. For simplicity, we set $V_2 = V_3 = 0$ and consider only the Hartree terms. The Bloch Hamiltonian for the low energy degrees of freedom is expressed in the 4×4 matrix,

$$H_{\mathrm{III}}(k) = \begin{pmatrix} \hat{h}^{(+)}(k) & \hat{\Delta} \\ \hat{\Delta}^\dagger & \hat{h}^{(-)}(k) \end{pmatrix}. \tag{3.24}$$

Here, the Dirac Hamiltonians at $K_\pm$ are given by

$$\hat{h}^{(\pm)}(k) = vk \cdot \tau. \tag{3.25}$$

The coupling between the two Dirac cones can be brought into the following form

$$\hat{\Delta} = 2V_1\rho \begin{pmatrix} 1 & 0 \\ 0 & -1 \end{pmatrix}. \tag{3.26}$$

Equation (3.24) can be diagonalized and we find the following doubly degenerate energy bands

$$E_{\pm}(k) = \pm\sqrt{v^2k^2 + 4\rho^2 V_1^2}. \tag{3.27}$$

In particular, an arbitrarily small coupling $V_1\rho$ continuously opens a gap $4V_1|\rho|$ at the Γ point in the reduced Brillouin zone. (The enlarged unit cell of CDW III moves the low-energy point from $K_\pm$ to Γ.) This means that the CDW III is a low-energy instability of the SM phase and explains why we observe a second order transition at a critical interaction strength. We also note that the low-energy theory for the CDW III, Eq. (3.24), carries similarities with the one found for the Kekulé texture on the honeycomb lattice[48] or in the π-flux model on the square lattice[88]. In analogy with these examples, we expect that topological defects of the CDW III pattern in the form of a Z_3 vortex can give rise to interesting physics; potentially including charge fractionalization and anyon statistics[95].

Topological phase at $f = 1/3$

As shown in Fig. 3.3(b) we find that a QAH phase can be stabilized in a certain region of parameter space. Nevertheless, it requires some fine tuning of the different interaction strengths. First, we do not find a QAH solution for V_1 alone in the parameter space we considered (which is different from what we find at $2/3$ filling, see Sec. 3.3.3). Second, for a moderate V_2 there exists a self-consistent solution of Eqs. (3.11) which breaks time reversal symmetry. This QAH phase is triggered by χ_2 and χ_2', the imaginary part of the nearest and second-neighbor hopping expectation values (which in general also acquire finite real parts). It turns out that for $V_3 = 0$, the CDW I phase has lower energy compared to the QAH solution. However, a finite V_3 increases the energy of the CDW I solution making the

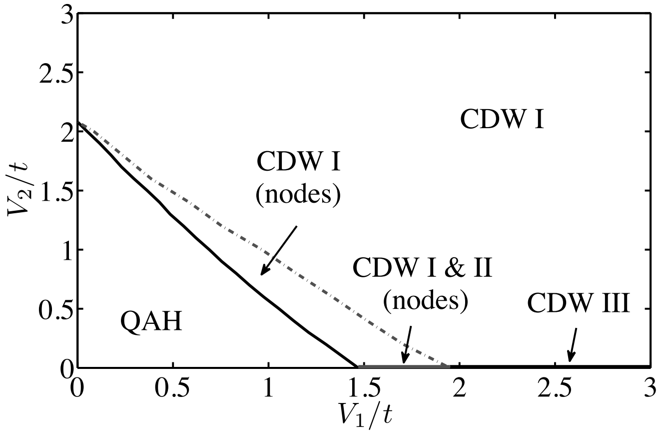

Figure 3.4: The phase diagram of the extended Hubbard model for spinless fermions at $2/3$ filling on the kagome lattice. The dotted line indicates where the gap opens in the CDW I phase. For $V_2 = 0$, CDW I and II coexist in the gray region and CDW III in the black region. We set $V_3 = 0$.

interaction-driven QAH phase the ground state for small V_1 and V_3 and moderate V_2, as shown in Fig. 3.3(b).

3.3.3 Phase diagram at $2/3$ filling

The phase diagram of the extended Hubbard model for spinless fermions at $2/3$ filling is shown in Fig 3.4. Here, we set $V_3 = 0$. The important difference with $1/3$ filling is that the Fermi energy in the noninteracting case lies at a QBCP between a dispersing and a flat band. As a consequence, the density of states is finite at the Fermi energy and the system is unstable to arbitrarily weak interactions[47]. In particular, the semi-metallic phase does not survive even for small values of the interactions. The phase diagram for low to intermediate interactions looks therefore quite different than the corresponding phase diagram at $1/3$ filling.

Topological phase at $f = 2/3$

For small to intermediate interactions we find that the QAH phase has the lowest energy. This is in agreement with quite general arguments made about the stability of a QBCP[47]. We have numerically calculated the Chern number [51] associated with this state and found that it is ± 1, indicating it is indeed a topological state displaying an integer quantum Hall effect. Note that V_1 alone is enough to generate the QAH phase because of the particular geometry of the kagome lattice with a triangle in the unit cell.

Although the QAH phase is the ground state in a rather large region of parameter space, its gap is exponentially small. The exponential dependence in mean-field theory can be found by analyzing the gap equation derived from an effective two band Hamiltonian describing the low-energy behavior around the QBCP. Let us for simplicity set $V_2 = 0$ in the following. A finite imaginary part of the nearest-neighbor bond hopping, $\chi_2 = \mathrm{Im}\langle c_i^\dagger c_j \rangle \neq 0$, couples the two bands thereby opening a gap. In lowest order in V_1, the matrix describing this coupling is given by

$$H_{\mathrm{QAH}}(k) = \begin{pmatrix} \varepsilon_2^*(k) & 2i\sqrt{3}V_1\chi_2 \\ -2i\sqrt{3}V_1\chi_2 & \varepsilon_3^*(k) \end{pmatrix}, \tag{3.28}$$

where $\varepsilon_{2,3}^*(k)$ is obtained from Eq. (3.5) by replacing t by

$$t^* = t + V_1\chi_0. \tag{3.29}$$

Here, $\chi_0 = \langle c_i^\dagger c_j \rangle_0 = 1/6$ denotes the nearest neighbor hopping expectation value in the noninteracting model and Eq. (3.29) takes into account the effect of the Fock term in lowest order in V_1. The self-consistency equation for χ_2 reads

$$1 = V_1 \int_{2t^*-\Lambda/2}^{2t^*+\Lambda/2} d\varepsilon \frac{N(\varepsilon)}{\sqrt{(2t^* - \varepsilon)^2 + 48 V_1^2 \chi_2^2}}, \tag{3.30}$$

where Λ is a cutoff energy of the order of t^* which is not accessible in the low energy description, and $N(\varepsilon)$ is the noninteracting density of states. Solving Eq. (3.30) for the order parameter χ_2 yields

$$\chi_2 = \frac{\Lambda}{2\sqrt{3}V_1} e^{-1/(V_1 N_0)}, \tag{3.31}$$

which holds for small values of the dimensionless coupling constant $V_1 N_0$. Here, we have introduced the density of states at the QBCP:[86]

$$N_0 = N(2t^*) = \frac{\sqrt{3}}{2\pi t^*}. \tag{3.32}$$

The gap is proportional to the order parameter χ_2 and from the result Eq. (3.31) and the eigenvalues of Eq. (3.28) it follows that

$$\Delta_{\text{QAH}} = 4\sqrt{3} V_1 \chi_2 = 2\Lambda e^{-1/(V_1 N_0)}. \tag{3.33}$$

We have checked that the exponential dependence given in Eq. (3.31) is indeed consistent with our full numerical evaluation of the self-consistency equations. A similar exponential dependence is also found in a one-loop renormalization group treatment [47] although the dimensionless coupling is renormalized compared to Eq. (3.33).

We now come back to the general situation where both V_1 and V_2 are finite. In general, the QAH phase is driven by both a complex first and second neighbor hopping expectation value. Furthermore, one can define an explicit deformation[16] of a tight-binding model with complex nearest neighbor hopping on the kagome lattice to show that its ground state is adiabatically connected to the ground state of a model with real nearest-neighbor hopping and only complex second nearest neighbor hopping. Therefore, the QAH phase generated by V_2 belongs to the same topological class as the one generated by V_1. Figure 3.5 shows the fluxes $\Phi_{1,2,3}$ through three elementary triangles forming the unit cell. In this figure, we set $V_2 = V_1/2$. Because of the periodic boundary conditions on a unit cell, the fluxes satisfy $2\Phi_1 + \Phi_2 + 3\Phi_3 = 0$. Moreover, they are all finite indicating the presence of an imaginary hopping amplitude in both the first and the second neighbor effective hopping.

CDW phases at $2/3$ filling

For intermediate to large interaction strengths, a CDW phase is stable. At $V_2 = 0$ and large V_1, the CDW III phase has the lowest energy. However, the difference in energy per site compared to CDW I is only of the order $10^{-3}t$ and becomes smaller the bigger V_1. As a result, a very small but finite V_2 is sufficient to stabilize CDW I over CDW III. In contrast to the situation at filling fraction $f = 1/3$, at $f = 2/3$ CDW III can not profit from a "nesting" condition. The energy gain compared to CDW I is therefore very small. At $V_2 = 0$, a first-order phase transition from a QAH state to a CDW I (II) state takes place at $V_1 \approx 1.47t$. Numerically, we can not resolve any difference in the energy between CDW I and II for $V_2 = 0$. Interestingly, there are nodes in the CDW I (II) phase where the gap vanishes. The transition from the QAH phase to the CDW I state with nodes is an example where a transition from a gapped phase (QAH) to a gapless phase (CDW I) occurs by increasing the interaction strength, [see Fig. 3.6(c)].

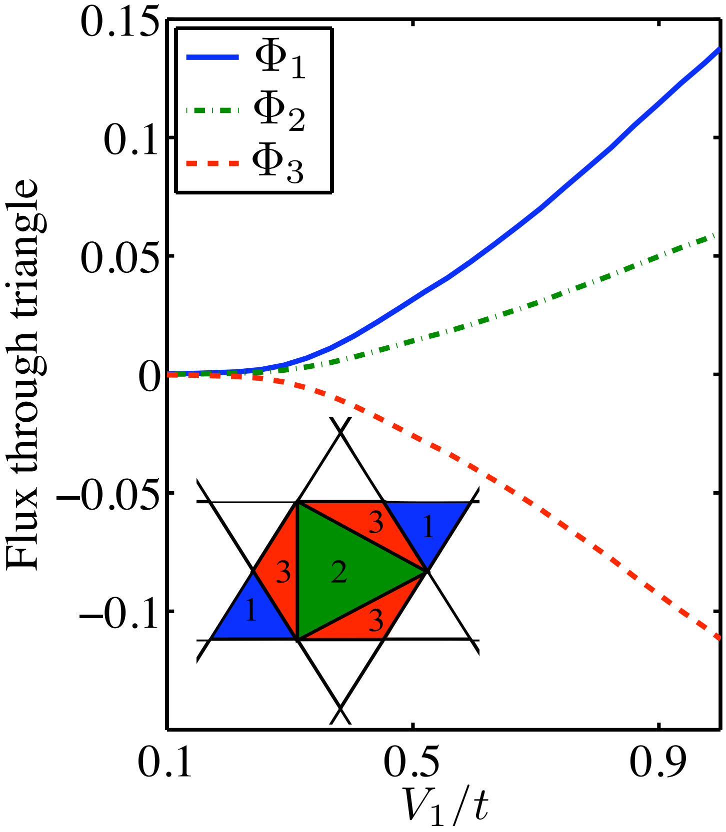

Figure 3.5: The fluxes $\Phi_{1,2,3}$ through elementary triangles in the QAH phase at filling fraction $f = 2/3$. These elementary triangles form the unit cell, as shown in the inset. Because of the periodic boundary conditions on the unit cell, the net flux is zero and the individual fluxes satisfy $2\Phi_1 + \Phi_2 + 3\Phi_3 = 0$. We have set $V_2 = V_1/2$ and $V_3 = 0$.

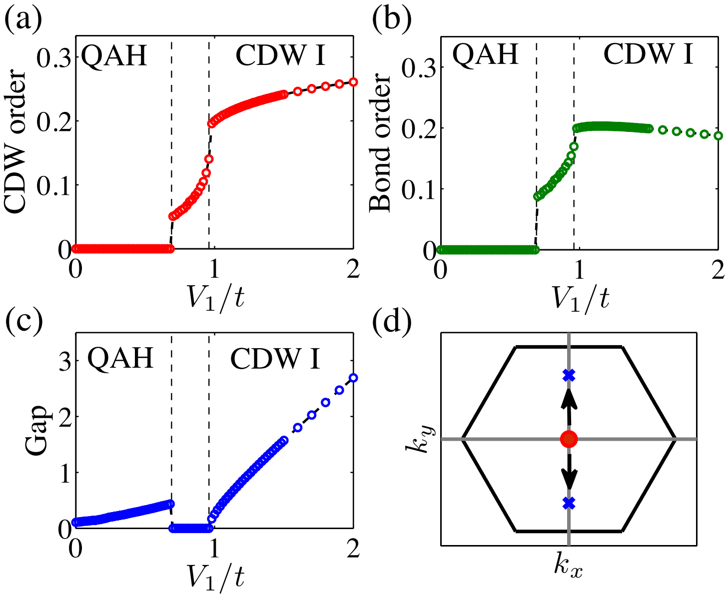

Figure 3.6: (a) the CDW order parameter ρ (b) the bond order defined as the difference between two nearest strong and weak bonds (c) the gap at $2/3$ filling fraction on the kagome lattice. We have set $V_2 = t$. (d) the splitting of a QBCP(red circle) into two Dirac points(blue cross) for gapless CDW I.

The gapless CDW I persists even for finite V_2. Figure 3.6 shows the CDW order parameter ρ, the bond order $\nu = \chi_s - \chi_w$ defined as the difference between two nearest strong and weak bonds and the magnitude of the gap as a function of V_1 for fixed $V_2 = t$. We can see that a finite CDW order is accompanied by a finite bond order. In fact, both types of orders jump to a finite value at the transition V_{1c_1} from the QAH to the CDW I phase. Note, however, that the gap is zero up to a second critical interaction strength V_{1c_2} indicating the presence of band degeneracy points below V_{1c_2}. At V_{1c_2} a kink is observed in the order parameters and the gap gradually starts to increase.

In the following, we show that the gapless CDW I phase results from the splitting of the QBCP into two nodes[47]. We notice that the change of bond-order is one order of magnitude smaller than t and therefore can be neglected for the moment. We find the following low-energy Bloch Hamiltonian

$$H_{\mathrm{CDW}}(k) = \begin{pmatrix} \varepsilon_2^*(k)+t^*u\cos(2\phi) & \frac{t^*u}{2}\sin(2\phi) \\ \frac{t^*u}{2}\sin(2\phi) & \varepsilon_3^*(k)-t^*u\cos(2\phi) \end{pmatrix}, \tag{3.34}$$

where $u = 2(V_1 + V_2)(\rho + 3\nu)/t^*$. The renormalized hopping t^* is given by Eq. (3.29) with χ_0 replaced by $\bar{\chi} = (\chi_s + 2\chi_w)/3$ and we have neglected the Fock-terms generated by the V_2 interaction (this term is negligible in practice). In Eq. (3.34) we have introduced polar coordinates (k, ϕ) which are defined by $k \cdot e_n = k\cos\phi$. Note that right at the Γ-point the angle ϕ is not well-defined. Equation (3.34) should be contrasted with Eq. (3.28) for the QAH phase: as opposed to the QAH order parameter, the CDW order parameter introduces an anisotropic *angle dependent* effective coupling between the two bands. Expanding the dispersion around the Γ point we find for the eigenvalues of Eq. (3.34),

$$E_2(k,\phi)/t^* = 2 - [k^2 + \sqrt{B(k,\phi)}]/8, \tag{3.35}$$

$$E_3(k,\phi)/t^* = 2 - [k^2 - \sqrt{B(k,\phi)}]/8. \tag{3.36}$$

The function $B(k,\phi)$ is given by

$$B(k,\phi) = k^4 - 16k^2 u\cos(2\phi) + 64u^2. \tag{3.37}$$

It has roots at two points where the two bands touches:

$$k_u = \sqrt{8u}, \quad \phi = 0, \pi. \tag{3.38}$$

This analysis shows that a finite CDW I order splits the QBCP into two nodes moving along the line defined by the vector e_n. The bottom right panel of Fig. 3.6 illustrates the situation for e_3. We have calculated the Berry phase (winding number)[47] of the QBCP and found that it is 2π ($= 0 \bmod 2\pi$). The corresponding Berry phases (winding numbers) of the two nodes appearing in the gapless CDW I are both π. Thus, the QBCP does splits into two Dirac points with Berry phases π conserving to total winding number, as it was suggested in Ref. [47].

3.3.4 Comparison with existing work

Recently, several numerical works[92, 93] appeared dealing with the charge density wave order on the kagome lattice at $f = 1/3$ or $f = 2/3$. Here, we want to briefly relate our results with their findings. In Nishimoto *et.al.*'s work[92], the authors considered the large V_1 limit with vanishing V_2. They showed that CDW III is the ground state that is consistent with the "plaquette" state obtained from an effective quantum dimer model on the honeycomb lattice. [94] In this strong interacting limit, $f = 1/3$ and $f = 2/3$ are equivalent and numerical calculations[92] confirm that CDW III is stabilized by the ring exchange process proportional to $|t|^3/V^2$. Interestingly, fractionalized excitations with charge $e/2$ have recently also been reported in the strong coupling limit[93].

Our mean-field calculation cannot capture the resonating nature of the quantum dimer model and is not valid in the strongly interacting limit. However, CDW III in the mean-field treatment can be viewed as the "classical" configuration of plaquette states. At $1/3$ filling fraction, the CDW III is found to be more stable than either CDW II or I at large V_1, and the energy difference between them becomes smaller as V_1 grows. This is consistent with Nishimoto *et.al.*'s work. Furthermore, we predict a metal-insulator transition takes places at $V_{1c} = 3.1t$ at $1/3$ filling, which is in quite good agreement with their result $V_{1c} = 4.0t$. However, at $2/3$ filling, our mean-field results differ significantly from theirs. We find that the leading instability at small interactions is the QAH state that spontaneously breaks time-reversal symmetry and has an exponentially small gap. [47] A metal-insulator transition takes place around $V_{1c} = 2t$ in our study while Nishimoto *et.al.* reported a metal-insulator transition at finite $V_{1c} = 2.6t$.

3.4 Spinful model on the kagome lattice

Let us now turn to the spinful model on the kagome lattice. The additional spin degrees of freedom add considerable complexity to the problem and introduce several more potential phases.

3.4.1 Candidate phases

The SM and the CDW phase are equivalent to those in the spinless model. Here, we discuss additional phases which appear in the spinful model.

Topological insulator and quantum anomalous Hall state

The topological insulator and quantum anomalous Hall state are both stabilized by a complex Fock term of nearest or second neighbor interaction which gives rise to a complex hopping amplitude. The difference between TI and QAH phases can be described by the 2×2 matrix $\langle c^\dagger_{i\alpha} c_{j\beta}\rangle$ defined in the spin space as discussed below.

The QAH state breaks the time reversal symmetry but not the spin rotation SU(2) symmetry. Therefore, the most general form of the uniform phase consistent with these requirements is

$$\langle c^\dagger_{i\alpha} c_{j\beta}\rangle = [(\chi_1 + i\chi_2)\sigma_0]_{\alpha\beta}\,, \tag{3.39}$$

where χ_1 and χ_2 are real numbers and $\sigma_0 = \hat{1}$ is the identity matrix. A phase with a finite χ_2 shows an anomalous quantum Hall effect and a non-zero Chern number.

On the other hand, the TI does not break time reversal symmetry but breaks the SU(2) spin rotation symmetry down to U(1). The most general form is therefore

$$\langle c^\dagger_{i\alpha} c_{j\beta}\rangle = [\chi_1\sigma_0 + i\chi_2(\vec{n}\cdot\vec{\sigma})]_{\alpha\beta}\,, \tag{3.40}$$

where χ_1 and χ_2 are both real numbers and $\vec{n}$ is a unit vector describing how the SU(2) spin rotation symmetry is broken. In other words, spin-rotation symmetry is only preserved for rotations around $\vec{n}$. Without loss of generality we can assume $\vec{n} = \hat{n}_z$. We note that allowing χ_1, χ_2 and $\vec{n}$ to be spatially dependent allows one to study topological defects of the order parameter, such as skyrmions, providing a potential route for exotic superconductivity[39]. On the other hand, in contrast to their two-dimensional counterpart, three-dimensional interaction-driven TIs completely break the spin-rotation symmetry and their order parameter involves a rotation matrix. Again, it is possible to study topological defects which host protected modes[38].

A short inspection of the mean-field free energy of the TI and the QAH phase shows that these two phases are degenerate on the mean-field level. It is likely that fluctuations around the mean-field state might favor one phase over the other. Because the TI breaks the continuous spin-rotation symmetry, there are Goldstone modes in the ordered phase[37]. It was suggested[37] that quantum fluctuations associated with these modes lower the ground state energy of the TI as compared with the QAH phase which does not have Goldstone modes. This argument appears to be confirmed via “unbiased” functional renormalization group methods[37]. We don’t see any reason for those arguments not to hold in the present case as well.

Spin-charge-density waves

There is another class of phases that emerges as a result of the special filling fractions, the non-bipartite nature of the kagome lattice and the additional spin degrees of freedom. We term it “spin charge density wave” (SCDW) because it involves both a spin and a charge density wave. In our mean-field calculations we restrict to phases which do not break the translational symmetry. By solving self-consistency equations we identify two types of SCDWs which are stable for some interaction parameters.

The first pattern, SCDW I, is characterized by the following distribution:

$$\langle n_{1\uparrow}\rangle = f+\rho+m, \tag{3.41a}$$

$$\langle n_{1\downarrow}\rangle = f+\rho-m, \tag{3.41b}$$

$$\langle n_{2\uparrow}\rangle = f+\rho-m, \tag{3.41c}$$

$$\langle n_{2\downarrow}\rangle = f+\rho+m, \tag{3.41d}$$

$$\langle n_{3\uparrow}\rangle = f-2\rho, \tag{3.41e}$$

$$\langle n_{3\downarrow}\rangle = f-2\rho. \tag{3.41f}$$

Here, ρ and m are the charge density and spin density order parameter, respectively. Furthermore, we assume that the symmetry of the bond expectation values is determined by the symmetry of the spin-charge configuration and therefore, three different spin-resolved bond expectation values have to be introduced. The phase SCDW I is schematically shown in Fig. 3.7(a).

The other configuration, SCDW II, is characterized by the following distribution:

$$\langle n_{1\uparrow}\rangle = f-\rho+m, \tag{3.42a}$$

$$\langle n_{1\downarrow}\rangle = f-\rho-m, \tag{3.42b}$$

$$\langle n_{2\uparrow}\rangle = f-\rho+m, \tag{3.42c}$$

$$\langle n_{2\downarrow}\rangle = f-\rho-m, \tag{3.42d}$$

$$\langle n_{3\uparrow}\rangle = f+2\rho-2m, \tag{3.42e}$$

$$\langle n_{3\downarrow}\rangle = f+2\rho+2m. \tag{3.42f}$$

The schematics of the SCDW II is shown in Fig. 3.7(b). In addition, we also introduce four different spin-resolved bond expectation values to make it consistent with the above spin-charge distribution.

Both SCDWs have zero magnetization in the unit cell. However, they differ in that SCDW I has antiferromagnetic order in the a_1 direction, ferromagnetic order in the a_2 and $a_1 - a_2$ directions, while SCDW II has ferromagnetic ordering in the a_1 direction but antiferromagnetic ordering in the a_2 and $a_1 - a_2$ directions.

In the next section, we will see that SCDWs arise in the case of large U but small or moderate V_1 and V_2. At $1/3$ filling fraction, SCDWs can be understood as a means to reduce the on-site interactions by single occupancy at two sites in a unit cell. Therefore they become unstable when V_1 or V_2 becomes large and CDW dominates. We stress that the solutions of SCDWs are saddle points of the free energy instead of a global minimum in the usual situation, therefore, one has to solve self-consistency equations directly to obtain the SCDW solutions.

Bond-order wave

Next we consider the bond-order wave (BOW) as has been found in Ref. [96] for the t-J model at $f = 1/3$ under quite general conditions. The BOW is characterized by a uniform charge distribution and a bond order which breaks the inversion symmetry of the unit cell by establishing strong bonds χ_s for the up triangles and weak bonds for the down triangles χ_w. It is schematically shown in Fig. 3.7(c).

Ferromagnet

The ferromagnetic state (FM) is characterized by a uniform magnetization density m. The spin densities are given by

$$\langle n_{i\uparrow} \rangle = f + m/2, \quad \langle n_{i\downarrow} \rangle = f - m/2, \tag{3.43}$$

and we introduce the Fock terms

$$\chi_\uparrow = \langle c^\dagger_{i\uparrow} c_{j\uparrow} \rangle, \quad \chi_\downarrow = \langle c^\dagger_{i\downarrow} c_{j\downarrow} \rangle. \tag{3.44}$$

The Fock terms are different for nearest-neighbor and second-neighbor bonds. Equations (3.43) and (3.44) are used as an *ansatz* to solve the self-consistency e-

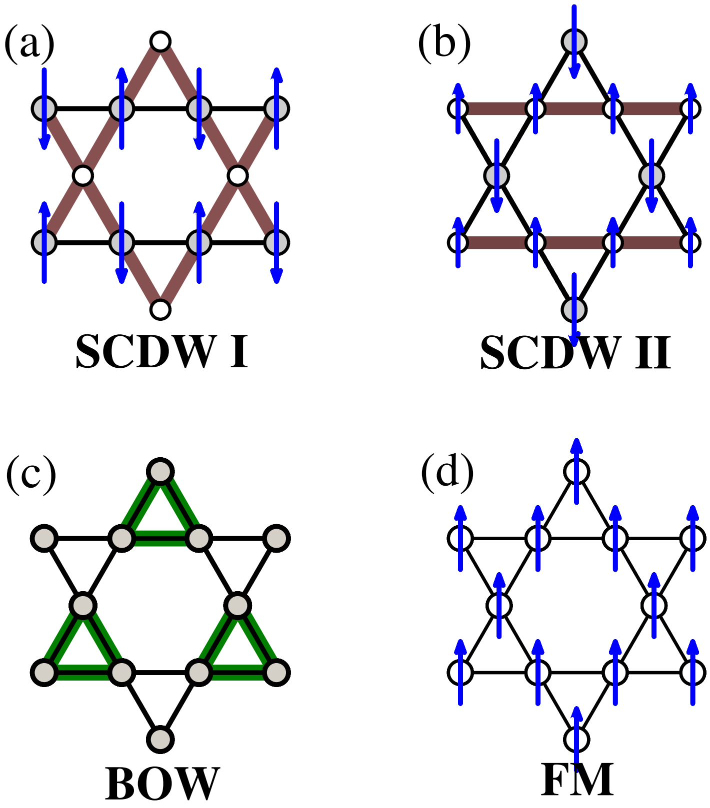

Figure 3.7: Schematic of four types of candidate phases on the kagome lattice for $1/3$ filling fraction: (a) SCDW I (b) SCDW II (c) bond-order wave (BOW) and (d) ferromagnet (FM). Upward arrows and downward arrows denote the magnetization on each site. The same/different circles represent same/different numbers of fermions on corresponding sites. For simplicity we only show nearest bonds (the addition of two spin-resolved bonds) and do not show the second nearest bonds. Stronger bonds are shown in bold.

quations numerically. A finite magnetization of the form Eq. (3.43) introduces a Zeeman field which uniformly lowers the energy of the spin-$\uparrow$ electrons with respect to the spin-$\downarrow$ electrons by Um. At $f = 1/3$ the maximally polarized state is obtained when there are two up electrons per unit cell. At $f = 2/3$, the maximally polarized state corresponds to 3 up electrons and one down electron per unit cell. At both filling fractions the saturated value of the magnetization is $m_{\mathrm{sat}} = 2/3$. In the next section, we will see that the maximally polarized FM state arises in the large U limit.

3.4.2 Phase diagrams at $1/3$ filling

We first discuss the role of U and V_1 and set $V_2 = V_3 = 0$. This allows for a direct comparison with the phase diagram at 2/3 filling shown below.

U-V_1 phase diagram at 1/3 filling

The U-V_1-phase diagram is shown in Fig. 3.8. Similar to the spinless model, we find that the SM is stable for small to intermediate interactions which we again attribute to the vanishing density of states at the Fermi energy in the noninteracting limit. For dominant V_1 interaction, we find that the CDW III is stable and the transition from SM to the CDW III is second order. For dominant onsite interaction U, a SCDW phase is stabilized. Both patterns SCDW I and SCDW II are stable for some values of the interaction. We note that for small V_1 there is a second order transition from the SM to the SCDW II with nodes.

For intermediate U and V_1 we find BOW is the favored ground state on kagome lattice at 1/3 filling[96]. It requires that U is of the same order as V_1 to suppress the CDW III. On the other hand, it requires a reasonable value of V_1 to generate the bond order at all. However, we expect that the superexchange mechanism (second order in t/U), which is not captured in our mean-field treatment, could stabilize this phase also for smaller V_1[96].

At quite large onsite interactions ($U \sim 20t$) a FM phase is stabilized (not shown). The FM state is fully polarized at the mean-field level and has an energy gain of

$$e_{\mathrm{FM}} - e_{\mathrm{SM}} = \bar{\varepsilon}_2 - \bar{\varepsilon}_1 + \frac{V}{24t}(\bar{\varepsilon}_1^2 - \bar{\varepsilon}_2^2 - 2\bar{\varepsilon}_1\bar{\varepsilon}_2) - \frac{U}{3} \tag{3.45}$$

per unit cell as compared to the SM phase. In Eq. (3.45), we have introduced the average kinetic energy of the filled band n,

$$\bar{\varepsilon}_n = \frac{1}{N}\sum_k \varepsilon_n(k), \tag{3.46}$$

where N is the number of unit cells in the lattice, and the dispersion relation $\varepsilon_n(k)$ is given in Eq. (3.5). We note that the presence of a FM state for large interactions is consistent with numerical studies[77]. Finally, we note that the QAH/TI phase does not occur in the absent of a finite V_2. Again, this is in agreement with the spinless case.

U-V_2 phase diagram at $1/3$ filling

The U-V_2 phase diagram of is shown in Fig. 3.9. Like in the spinless case at $1/3$ filling fraction, we add a small V_3 interaction to suppress CDW I for finite V_2 and stabilize TI/QAH. The overall structure is quite similar to the U-V_1 phase diagram. However, the charge density wave has pattern I for large V_2 since large V_2 does not favor CDW III but CDW I. BOW phase is now replaced by the QAH/TI phase. That the topological phase appears in the middle of the phase space seems to be a rather

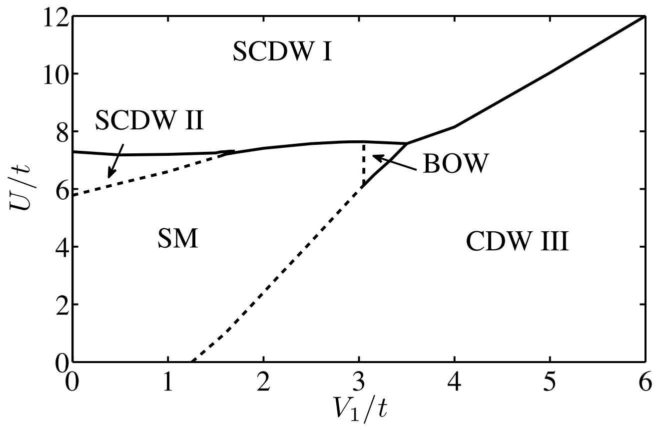

Figure 3.8: The phase diagram of the spinful model at 1/3 filling on the kagome lattice. The SCDW I and II phase involve both a finite charge and spin density wave order parameter. Furthermore, when U competes with V_1 a bond-order wave (BOW) is found. Solid lines indicate first order and dashed lines second order transitions.

universal feature in systems which have a Dirac point and has also been reported on the honeycomb and the diamond lattice[37, 38]. For large $U \sim 6t$, SCDW II is stabilized and we find that it is gapless. A first-order phase transition from SCDW II to SCDW I occurs when V_2 increases and finally CDW I dominates for large V_1. Note a FM state occurs at even larger $U \sim 20t$ (not shown).

3.4.3 Phase diagram at $2/3$ filling

For 2/3 filling we focus only on the U-V_1 phase-diagram. The phase diagram is shown in Fig. 3.10. Most importantly, we found that the dominant instability for arbitrarily small V_1 is to the QAH/TI phase and this phase survives also for finite U. Increasing V_1 further, there is a first order transition to a gapless and then gapped CDW.

We note that for $V_1 \lesssim 0.3t$ the energy difference between various states is

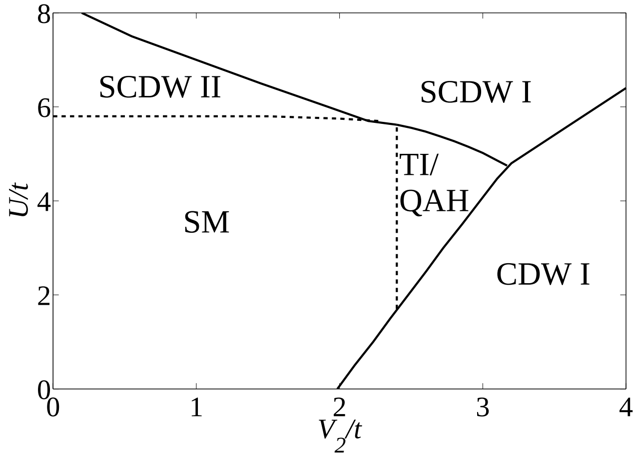

Figure 3.9: The U-V_2 phase diagram for $V_1 = 0$ and $V_3 = 0.4t$. An interaction-driven TI appears for finite U and V_2. Solid lines indicate first order and dashed lines second order transitions

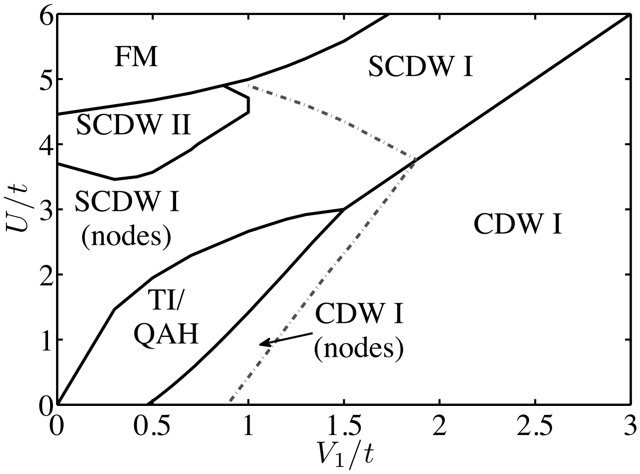

Figure 3.10: The $U - V_1$ phase diagram for $V_2 = V_3 = 0$ at $2/3$ filling fraction. Similar to the spinless case at $2/3$ filling fraction, CDW I has nodes which separates itself from gapped phase by a dash-dot line. Similarly, SCDW I has nodes for small interaction strengths.

very small: SCDW I and II as well as QAH/TI have energy differences of less than $10^{-6}t$ per unit cell and we had to use a very high precision in the numerical calculation to resolve the phase diagram. However, for larger values of U the FM phase is clearly favored in the mean-field calculation. This is again a maximally polarized FM state. The energy density as compared to the SM phase is

$$e_{\mathrm{FM}} - e_0 = -(\bar{\varepsilon}_1 + 2\bar{\varepsilon}_2) - \frac{V_1}{24t}(\bar{\varepsilon}_1^2 - \bar{\varepsilon}_2^2 - 2\bar{\varepsilon}_1\bar{\varepsilon}_2) - \frac{U}{3}, \tag{3.47}$$

and we have used the definition Eq. (3.46). While the energy gain for the onsite repulsion U is the same in the SCDWs, it is the kinetic energy which favors the FM phase over the SCDWs for large U.

3.5 Spinless Fermions on Decorated Honeycomb Lattice

In this section, we briefly examine the possibility of an interaction-driven QAH state for spinless fermions on the decorated honeycomb lattice and discuss the relationship of the QAH phase with other competing phases. The study of interaction effects on this lattice is partially motivated by a recent paper that exactly solved[17] the Kitaev model on this lattice in the strongly interacting limit of the underlying fermions; our previous paper established the existence of TIs on this lattice in the noninteracting limit[16]. One natural question to ask is what will happen for intermediate interaction strengths where the Hartree-Fock mean-field approximation is still valid. We work at half filling and $t' = t$ and show that the QAH state is the leading instability in the presence of interactions. Moreover, it occupies a rather wide region in the phase diagram.

The Fermi surface at $1/2$ filling lies at a quadratic band crossing point in the center of the Brillouin zone, where a flat band crosses a quadratic band. It allows the emergence of a QAH phase quite easily without any fine tuning of interaction strengths. We consider the nearest-neighbor interaction V_1 and second nearest-neighbor interaction V_2 on this lattice. For the V_1 interaction, we can introduce a dynamically generated flux pattern in the two triangles. We also introduce a second-neighbor flux in the same way as in the kagome lattice [see Fig. 3.11(a)]. One key difference, however, is that we have to allow the possibility of different values of inter-triangle complex hopping parameters and intra-triangle complex hopping parameters due to nonequivalence of the two hopping parameters in the non-interacting limit. One can easily show that if the flux through a unit cell is zero and time-reversal symmetry is broken, a QAH state is realized similar to the one on kagome lattice. In our calculation, we also find it is possible to have a BOW state if the phase of the flux is zero or π. The BOW is very close in energy to the QAH state ($10^{-6}t$), but appears to lose out for the parameter ranges we studied.

We will restrict ourselves to $q = 0$ CDW that originates from the Hartree term of the mean-field Hamiltonian. At $1/2$ filling, one can see that V_1 and V_2 frustrate each other, in contrast to the kagome lattice at $1/3$ filling where V_1 and V_2 both stabilize a CDW state. The CDW pattern we found based on the mean-field self-consistency equations is shown in Fig 3.11(b). Among several CDW solutions we have found, we identify this particular CDW with a mirror symmetry as having the lowest ground state energy. Real bond orders from the Fock term have also been introduced implicitly to be consistent with this CDW pattern.

The phase diagram is shown in Fig. 3.12. Along the horizontal axis where $V_2 = 0$, a BOW phase competes with the QAH for small interaction but is higher in energy by $\sim 10^{-6}t$. A CDW phase develops for $V_1 > 1.9t$. Generally, the energy

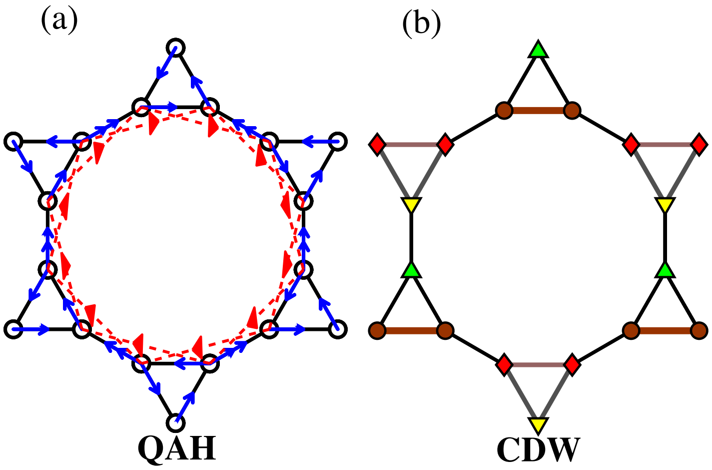

Figure 3.11: (a) the flux pattern developed by interactions that preserves the lattice symmetry but spontaneously breaks time reversal symmetry on decorated honeycomb ("star") lattice. The blue solid line with an arrow (two arrows) represents a nearest neighbor intra-triangle(inter-triangle) complex hopping while the red dash line with an arrow represents the second neighbor complex hopping. (b) the favorable CDW pattern from solutions of self-consistency equations. We have used different combinations of color and markers to show the mirror symmetry. Real first neighbor bonds consistent with symmetry of the CDW pattern have been assumed (second neighbor bonds not shown).

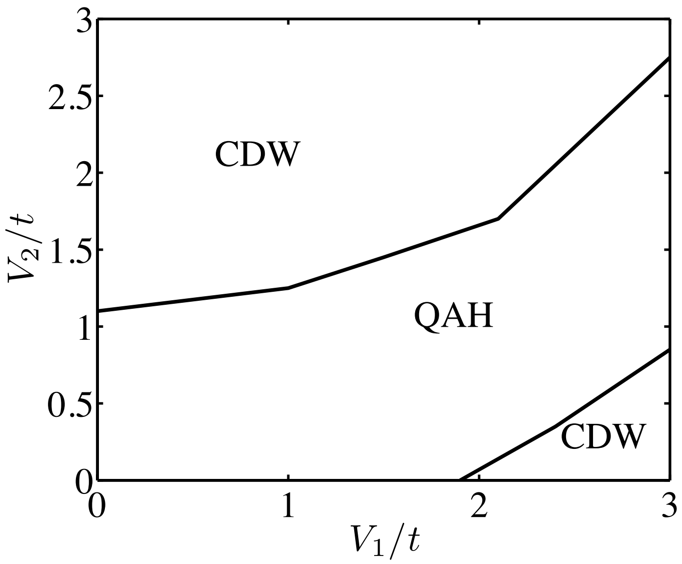

Figure 3.12: The phase diagram of the extended Hubbard model of spinless fermions at 1/2 filling on the decorated honeycomb lattice. Due to the mutual frustration of V_1 and V_2, the QAH phase occupies the middle part of phase diagram and the regions of CDW phase have been split into two parts. We have set $t' = t$.

gain from forming a uniform distribution of fermions and complex bonds between neighbor sites is very small compared to that in the CDW phases. Therefore, the QAH phase is the only favorable ground state when either (i) there are no CDW solutions, or (ii) the CDW states are frustrated or suppressed and therefore have much higher ground state energy. The first case has been seen in the kagome lattice at $2/3$ filling fraction for small interactions, and the second situation is realized in the present case of the decorated honeycomb lattice at 1/2 filling where a QAH phase occupies a large region of the phase diagram. This is intimately related to the mutual frustration between the V_1 and V_2 interaction at $1/2$ filling. To see this, let us consider the large $V_2 \gg V_1$ limit. One finds that in order to minimize the interaction V_2, the preferred ground state is the CDW configuration where three sites in a top triangle are almost occupied while the three sites in the bottom triangle in the same unit cell are almost empty. This is exactly the sublattice potential perturbation considered in Ref. [16] that destabilizes the quantum spin Hall phase. Though this sublattice potential appears artificial at first sight, we show here that it can result from a many-body interaction. Clearly this configuration is not stable if V_1 is increased beyond a critical value. This explains the fact that at large V_1 or V_2 the CDW phase is the ground state, while the QAH state is the ground state when V_1 is comparable to V_2.

It is possible to perform a similar mean-field calculation for the spinful case, and one expects that a TI/QAH phase will dominate at small interactions strengths for 1/2 filling. However, the details are beyond the scope of this paper and is left to future work.

3.6 Summary

We have presented comprehensive Hartree-Fock mean-field calculations of the phase diagram for spinless and spinful fermions described by the extended Hubbard model on the kagome lattice and decorated honeycomb lattice. We have established the existence of interaction-driven topological phases at filling fractions where either Dirac points or quadratic band crossing points are involved. We find that both TI and QAH phases can be described by conventional complex bond order parameters. Quite generally, we find that at $2/3$ filling on the kagome lattice and 1/2 filing on the decorated honeycomb lattice (where a quadratic band crossing point is involved in the non-interacting limit), the TI/QAH phase is the leading instability for small interaction strengths. We have observed also that interaction-driven topological phases only exist beyond a critical interaction value when the Fermi surface lies at Dirac points at $1/3$ filling on kagome lattice (in the zero interaction limit). Furthermore, we discuss in detail various other phases including charge density wave, spin-charge density wave, bond-ordered wave, and ferromagnets on the two lattices.

An important lesson drawn from this study is that systems whose non-interacting band structures involve quadratic band crossing points can be unstable to topological phases with arbitrarily weak interactions, even in the absence of microscopic spin-orbit coupling. We hope this work will aid in the search for topological states of matter by enlarging the class of candidate materials to include those which *do not* have strong microscopic spin-orbit coupling but do have certain features (such as quadratic band touching points) in their non-interacting band structure.

Chapter 4

Competing Exotic Topological Insulator Phases in Transition Metal Oxides on the Pyrochlore Lattice with Distortion

4.1 Introduction

Transition metal oxides have been an active topic of research for decades[97, 98]. In particular, the interplay between Coulomb interaction, spin-orbit coupling, and lattice degrees of freedom have made transition metal oxides an ideal playground to test new theories and discover exotic behaviors. Notable examples are high temperature superconductivity[99, 100], colossal magnetoresistance[101], heavy fermion physics[102–104] and many other possibilities[97, 98, 105]. The rather localized nature of 3*d* orbitals (compared to 4*d* and 5*d*) in some transition metal oxides enhances the on-site electron-electron interaction and typically makes it a dominant energy scale[97, 98]. In the 3d transition metal oxides other interactions such as spin-orbit and electron-lattice coupling are typically small compared to the on-site Coulomb interaction and ground states with antiferromagnetic order are typical[106].

However, 4d and 5d orbitals in layered perovskites such as Sr_2RuO_4, Sr_2RhO_4, Sr_2IrO_4, Na_2IrO_3, and the hyperkagome $Na_4Ir_3O_8$ are more spatially extended and thus the Coulomb interaction is typically weaker than those with 3d orbitals[107]. The more extended nature of the 4d and 5d orbitals compared to the 3d orbitals leads to a greater level splitting in a crystal field, and enhances their sensitivity to lattice distortions. In many oxides, the transition ions are surrounded by an octahedron of oxygen atoms, MO_6, where M represents a transition metal ion. The crystal field splits the 5 degenerate (neglecting spin for the moment) d-orbitals into two manifolds (see Fig.4.1c): a lower lying t_{2g} (d_{xy}, d_{yz}, d_{zx}) manifold and a higher lying e_g $(d_{3z^2-r^2}, d_{x^2-y^2})$ manifold[97, 98]. The energy separation between the t_{2g} and e_g levels is conventionally denoted "10Dq" and is typically on the order of $\sim$1-4 eV, which is large compared to many 3d compounds[108].

Besides the crystal field, the relativistic spin-orbit coupling is another energy scale that results from the large atomic numbers of heavy transition elements. While in the absence of spin-orbit coupling the on-site Coulomb interaction is of the same order as the band width[109, 110], inclusion of strong spin-orbit coupling modifies the relative energy scales[41]. Thus, for materials with 4d and particularly 5d electrons, one expects the appearance of novel phases with unconventional electronic structure due to the characteristic energy of spin-orbit coupling approaching that of the Coulomb interactions[41].

In a cubic environment, the $L = 2$ orbital angular momentum of the d-

orbitals is projected down to an effective angular momentum $l = 1$ (with a minus sign) in the t_{2g} manifold[41]. When the spin-orbit coupling is also strong, neither spin nor orbital angular momentum is a good quantum number. Instead, the total angular momentum, *i.e.* $j = l + s$, is a conserved quantity, where s is the spin of the electron. Thus, spin-orbit coupling splits the t_{2g} orbitals with spin into a $j = 1/2$ doublet and $j = 3/2$ quadruplet separated by an energy gap proportional to the strength of the spin-orbit coupling, λ. (See Fig.4.1c.) For large enough spin-orbit coupling, the new effective spin states lead to a great deal of novel Mott insulating states[111–116], possible spin liquids in the hyper-kagome lattice [117–124], orbital-oriented exchange coupling in Kitaev-type models[49, 125], Dirac semimetal with Fermi arcs[21], the quantum spin Hall effect[126], topological Mott insulators[41], topological magnetic insulators with axionic excitations[127, 128], and possibly high temperature superconductivity[129].

Of particular interest in this paper are the topological phases that occur in weak to moderately strongly interacting systems with strong spin-orbit coupling[3–5, 10–12, 25, 27, 28, 31, 62]. (For excellent recent reviews see Refs. [7] and [6].) The possible time-reversal invariant topological phases of matter have nontrivial topological features in their global band structure and robust edge (surface) states. When strong electron correlations are taken into account, spin-orbit coupling can give rise to a topological Mott insulating phase in which the charge degrees of freedom are completely gapped (even on the surface), but where the spin degrees of freedom inherit the non-trivial band topology from the weakly interacting limit[40, 41, 70]. Thus, the spin degrees of freedom form gapless spin-only edge (surface) modes. Such edge (surface) states can in principle be detected in thermal transport measurements (but not so readily in spin transport as the spin-orbit coupling generically destroys all spin conservation laws).

In this work we focus on the interplay and competition between strong correlation effects, spin-orbit coupling, and lattice distortion that is expected to be important in heavy transition metal oxides. In the heavy transition metal oxides one expects both the spin-orbit coupling[126, 130] and the lattice distortion energies[131] to be of the order of $0.05-0.5$ eV, while the interaction energy is typically at the higher end of this scale to somewhat larger, $0.5-2$ eV[21, 132]. While the phase diagram of an interacting undistorted pyrochlore model with $j=1/2$ has already been studied[41], we expand those results to include the effects of distortions of the local octahedra on the phase diagram. We also investigate pyrochlore oxides at different d-level fillings with the Fermi energy lying in the quadruplet $j=3/2$ manifold, which has not been considered in previous works. One of our motivations is to see if the $j=3/2$ manifold can also realize the interesting Mott phases of the $j=1/2$ manifold[41]. We find that, indeed, these exotic phases can be realized for the $j=3/2$ manifold. Moreover, we find that for the $j=1/2$ manifold "weak" topological variants of the exotic Mott phases can also appear in the phase diagram when certain types of lattice distortion are present.

This chapter is organized as follows. In Sec. 4.2 we derive an effective nearest-neighbor tight-binding Hamiltonian that properly captures the non-interacting limit of the physics, and include an on-site Hubbard interaction term to describe electron correlations. In the absence of interactions and distortions, the ground state is metallic for weak spin-orbit coupling, and becomes a strong topological insulator as spin-orbit coupling grows. In Sec. 4.3, 4.4, and 4.5 we study the effects of Coulomb interaction and lattice distortion on equal footing using the slave-rotor mean-field theory[133, 134]. As the strong correlation limit is approached, a Mott transition occurs and exotic phases are realized. We discuss the conditions that favor these unusual phases. Finally, we conclude in Sec.4.7 and outline interesting topics for further study.

4.2 Derivation of the effective Hamiltonian

In this work, we restrict our attention to pyrochlore oxides of the form $A_2M_2O_7$, where A is a rare earth element and M is a transition metal element. Examples include $A_2Ir_2O_7$ (A=Y, Pr, Eu or other rear-earth elements), $Cd_2Os_2O_7$, and $Cd_2Re_2O_7$. In these materials, the transition metal elements form a pyrochlore lattice and each M sits in the center of an oxygen octahedron[135]. The relevant geometry and coordinate system we use, along with the important level splittings, are shown in Fig. 4.1.

For strong spin-orbit coupling and with $d^{\alpha}(\alpha \leq 4$, *i.e.*, less than 4 electrons) the upper $j = 1/2$ manifold is empty and the important electronic structure is given by the lower $j = 3/2$ manifold. In ordered double perovskites with a local quadruplet, *strong on-site interactions* add bi-quadratic and bi-cubic exchange interactions to the effective spin exchange Hamiltonian deep in the Mott regime[136]. It is also argued that the same local C_3 distortion that we consider in subsequent sections maps the exchange Hamiltonian into a pseduo-spin-$1/2$ model that favors magnetic order[130].

Here we focus on the weak to moderately strongly interaction regimes[41, 135]. We begin by deriving an effective tight-binding Hamiltonian between transition ions located at the vertices of the corner-shared tetrahedrons in the pyrochlore lattice shown in Fig.4.1a. The transition ions we consider have $5d$ orbitals with three or five electrons in the triply degenerate (neglecting spin) t_{2g} manifold. The spin-orbit coupling in this manifold has the following form[97]

$$H_{so} = -\lambda l \cdot s, \tag{4.1}$$

where $l = 1$ and $s = 1/2$ describe the orbital and spin degrees of freedom, and $\lambda > 0$ parameterizes the strength of the spin-orbit coupling. That the t_{2g} orbitals can be

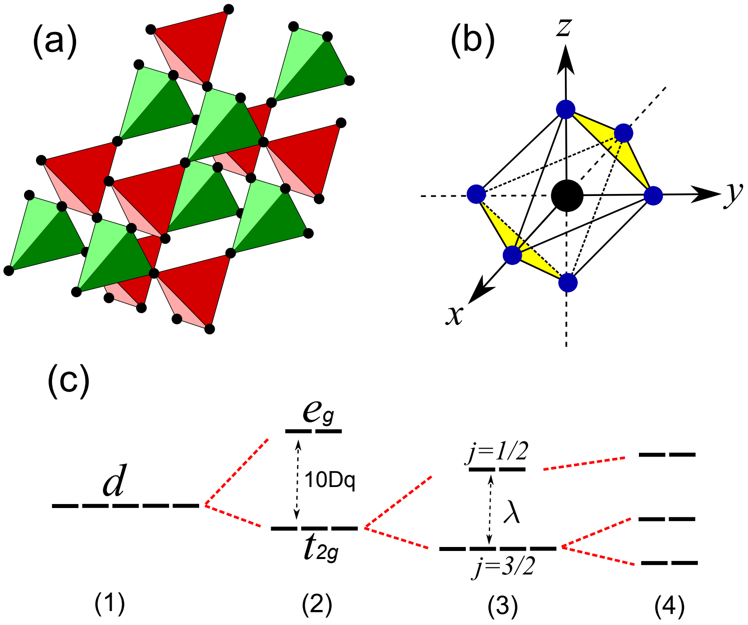

Figure 4.1: (a) An illustration of the pyrochlore lattice which is composed of corner sharing tetrahedra. Transition elements are indicated by black solid circles. (b) Each transition ion is surrounded by an oxygen octahedron shown by six solid blue (dark grey) circles. A transition ion is located at the origin of the local coordinate and is shown in black. We study a trigonal distortion preserving C_3 symmetry applied along the [111] direction (or its equivalent), shown by two yellow (grey) faces, and an elongation preserving C_4 symmetry along the z-axis of the local coordinate. (c) A schematic representation of the splitting of the bare atomic d-levels (1), due to a cubic crystal field arising from the octahedral environment (2), unquenched spin-orbit coupling in the t_{2g} manifold (3), and a distortion of the octahedron (4). The values of the splittings in (4) depend on λ and $\Delta_{3,4}$.

effectively described by angular momentum $l = 1$ comes from the projection of the d-orbital angular momentum into the local basis of t_{2g} manifold[41, 136].

To study the effects of lattice deformations[137], we assume that the octahedron surrounding an ion can be distorted in two ways: (1) a trigonal distortion preserving local C_3 symmetry and (2) an elongation (expansion) of octahedra preserving local C_4 symmetry. (See Fig.4.1b.) The former has been argued to be rather common and can be described by the following Hamiltonian on each transition metal ion site[135]:

$$H_{tri} = -\Delta_3(d_{yz}^\dagger d_{zx} + d_{yz}^\dagger d_{xy} + d_{zx}^\dagger d_{xy}) + h.c., \tag{4.2}$$

where Δ_3 parameterizes the strength and sign of the C_3 preserving distortion, and the C_4 elongation/contraction splitting is described by[136]

$$H_{el} = \Delta_4 l_z^2 = \Delta_4(n_{yz} + n_{zx}), \tag{4.3}$$

where Δ_4 parametrizes the strength and sign of the distortion, and l_z is the z component of the effective angular momentum of the t_{2g} orbitals related to the occupation of the d_{xy} orbital by $n_{xy} = n_d - (l_z)^2$ which follows from the constraint $n_d = n_{xy} + n_{yz} + n_{zx}$[136]. (See also Appendix.) For an elongation of the tetrahedron, $\Delta_4 < 0$, and for a compression of the tetrahedron, $\Delta_4 > 0$. Trigonal distortions appear to be more common in real materials, and the magnitude of the energy splittings can be crudely estimated from density functional theory calculations based on X-ray determined positions of oxygen atoms around the transition metals. We are not aware of detailed calculations of this type for the 4d and 5d pyrochlore oxides, but closely related 3d systems appear to have splittings on the level of $0.01 - 0.5$

eV[131]. We take this as crude estimate, with the larger end of the energy scale probably more likely for the more extended 4d and 5d orbitals.

Thus, the local Hamiltonian describing the t_{2g} orbitals on each site is

$$H_{local} = H_{so} + H_{tri} + H_{el}. \tag{4.4}$$

The Hamiltonian (4.4) can be easily diagonalized and its eigenvectors describe a projection onto the spin-orbit plus distortion basis. We will denote the projection by a matrix M, which contains all the information about the spin-orbit coupling and the distortion of the octahedra (all assumed identical so translational invariance is preserved). Moreover, due to the presence of time-reversal symmetry, the eigenvectors form Kramers pairs. A schematic representation of splitting t_{2g} upon including the terms in Eq.(4.4) is shown in Fig.4.1c.

We now turn to a derivation of the effective Hamiltonian. We first assume $\lambda = \Delta_3 = \Delta_4 = 0$, *i.e.* neglect the contributions in (4.4). To obtain the kinetic terms of the Hamiltonian, we need to describe the t_{2g} orbitals of a single ion in the local coordinate system defined by the octahedron of oxygen atoms surrounded the ion, and we need the p-orbitals of oxygen in the global coordinate system. The hopping of electrons from one transition metal ion to a nearest-neighbor transition metal ion is mediated by the oxygen p-orbitals. (We note that for the relatively extended 5d orbitals direct overlap may also be important, as well as further neighbor hopping[115].) We thus compute the p-d overlaps to determine the hopping matrix elements. The local and global axes are related by a set of rotation matrices[41, 135]. The combination of rotation matrices and d-p overlaps gives rise to the following Hamiltonian:

$$H_d = \varepsilon_d \sum_{i\gamma\sigma} d^{\dagger}_{i\gamma\sigma} d_{i\gamma\sigma} + t \sum_{<i\gamma\sigma, i'\gamma'\sigma'>} T^{ii'}_{\gamma\sigma,\gamma'\sigma'} d^{\dagger}_{i\gamma\sigma} d_{i'\gamma'\sigma'}, \tag{4.5}$$

where i, γ, and σ in the sums run over lattice sites, t_{2g} orbitals (xy, yz, zx), and spin degrees of freedom, respectively. The ε_d stands for the onsite energy of the degenerate t_{2g} orbitals, and $t = \frac{V^2_{pd\pi}}{\varepsilon_p - \varepsilon_d}$ is the unrotated hopping amplitude depending on the overlap integral $V_{pd\pi}$ and the energy difference between p and d orbitals. The parameter t sets the basic hopping energy scale in the problem. Without loss of generality we set $\varepsilon_d = 0$.

The effect of spin-orbit coupling and distortion are included via the projection of Hamiltonian in Eq.(4.5) into the eigenvectors of the local Hamiltonian in Eq.(4.4) using matrix M as follows:

$$H_0 = \sum_{i\alpha} \upsilon_\alpha c^{\dagger}_{i\alpha} c_{i\alpha} + t \sum_{<i\alpha, i'\alpha'>} \Gamma^{ii'}_{\alpha,\alpha'} c^{\dagger}_{i\alpha} c_{i'\alpha'}, \tag{4.6}$$

where υ_α $(\alpha = 1, ..., 6)$ stands for the six eigenvalues of local Hamiltonian (4.4), and the matrix Γ describes the hopping between sites given in the local basis via $\Gamma = M^* T M^T$. The $c^{\dagger}_{i\alpha}(c_{i\alpha})$ is the creation (annihilation) operator of an electron at site i and in local state α. Finally, we add a Coulomb interaction to obtain

$$H = H_0 + \frac{U}{2} \sum_i (\sum_\alpha c^{\dagger}_{i\alpha} c_{i\alpha} - n_d)^2, \tag{4.7}$$

where U is the on-site Coulomb interaction and n_d is the number of electrons on the 5d orbital of the transition metal ion. In the remainder of this paper, we investigate the zero-temperature phase diagram of the full Hamiltonian (4.7), which includes the spin-orbit coupling and lattice distortions in (4.4).

Before closing this section, it is instructive to take a look at the non-interacting limit of our model. In the absence of distortion, small spin-orbit coupling favors a metallic state for all fillings we consider (because they correspond to partially filled bands). However, strong spin-orbit coupling opens a gap at $\lambda/t = 2.8$ for filling $n_d = 5$[41], and for $\lambda/t = 2.5$ at filling $n_d = 3$ (see Fig.4.3). The two fillings correspond to the $j = 1/2$ and $j = 3/2$ manifolds in the bands, with one hole/ion in each case. Therefore, strong spin-orbit coupling can turn the metallic band structure arising from the quadruplet $j = 3/2$ manifold into a band insulating phase.

By using the Fu and Kane[5] construction, we can determine whether the insulating phase is trivial or topological. We make use of the inversion symmetry of the model and look for the parity of eigenstates at the time reversal invariant momenta. Those parities are related to the strong topological Z_2 index ν_0 via the following relation,

$$(-1)^{\nu_0} = \prod_m \prod_i \xi_{2m}(\Gamma_i), \tag{4.8}$$

where the first product is taken over filled bands, the second one over the time reversal invariant momenta Γ_i, and $\xi_m(\Gamma_i)$ is the corresponding parity eigenvalue of band m at time-reversal invariant momentum Γ_i. (Note that only one band from each set of Kramer's pairs is included in the product. Note also, that we have followed convention and used Γ_i with a single subscript for the time-reversal invariant momenta. It should not be confused with the multi-indexed $\Gamma^{ii}_{\alpha,\alpha'}$ in (4.6) that describes the hopping.) The index i is a collective index, *i.e.* $i \in \{i_1, i_2, i_3\}$, in terms of reciprocal lattice vectors K of the pyrochlore lattice: $\Gamma_i = 1/2(i_1\mathrm{K}_1 + i_2\mathrm{K}_2 + i_3\mathrm{K}_3)$ so that $i_1, i_2, i_3 = 0, 1$. The week indices are defined in a similar way to the strong index:

$$(-1)^{\nu_j} = \prod_{m} \prod_{i(i_j=1)} \xi_{2m}(\Gamma_i), \tag{4.9}$$

where $j = 1,2,3$. Thus, the index $(\nu_0;\nu_1\nu_2\nu_3)$ defines sixteen classes of band insulators. If $\nu_0 = 1$, the state is said to be a strong topological insulator (STI) and it has time-reversal symmetry protected gapless boundary excitations described by an odd number of Dirac cones in the surface state Brillouin zone[5]. On the other hand, if $\nu_0 = 0$ but $\nu_j \neq 0$ for at least one $j \in (1,2,3)$ then the state is said to be a weak topological insulator (WTI). In this case, gapless surface modes may be present in a clean system, but can be destroyed with disorder. As we will see, we find both STI and WTI (including strong correlation generalizations) in our model when lattice distortions are present. (See Fig.4.2 lower panel.)

4.3 Slave-rotor mean-field theory and self-consistent equations

In this section we apply the slave-rotor mean-field theory developed by Florens and Georges[133, 134] to treat the effect of weak to intermediate strength Coulomb interactions in the regime where the charge fluctuations remain important. In this theory each electron operator is represented in terms of a collective phase, conjugate to charge, called a rotor and an auxiliary fermion called a spinon as

$$c_{i\alpha} = e^{i\theta_i} f_{i\alpha}, \tag{4.10}$$

where $c_{i\alpha}$ is the electron destruction operator at site i with quantum number α, representing the states in (4.7). The factor $e^{i\theta_i}$ acting on the charge sector is a rotor lowering operator (with θ_i a bosonic field), and $f_{i\alpha}$ is the fermionic spinon operator. The product of the two results in an object with fermi statistics, need for the electron. Note the rotor part only carries the charge degree of freedom while the spinon part carries the remaining degrees of freedom α. Therefore, an electron has natural spin-charge separation if α is spin in this representation.

A constraint should be imposed to retain the physical states as

$$L_i + \sum_{\alpha} f_{i\alpha}^{\dagger} f_{i\alpha} = n_d, \tag{4.11}$$

where L_i is number of rotors. Using this representation, the interacting Hamiltonian (4.7) can be written as,

$$\begin{aligned} H = \sum_{i\alpha} (\upsilon_\alpha - \mu) f_{i\alpha}^{\dagger} f_{i\alpha} + t \sum_{<i,i'>} \Gamma_{\alpha,\alpha'}^{ii'} e^{-i(\theta_i - \theta_{i'})} f_{i\alpha}^{\dagger} f_{i'\alpha'} \\ + \frac{U}{2} \sum_i L_i^2, \end{aligned} \tag{4.12}$$

where a chemical potential μ has been introduced. In order to treat the phase θ and angular momentum L on an equal footing, we need to switch from (θ, L) to fields $(\theta, i\partial_\theta)$[134] so that $i\partial_\tau \theta = \frac{\partial H}{\partial L}$, which gives $L = (i/U)\partial_\tau \theta$. The corresponding action is

$$S = \int_0^{\beta} d\tau [-iL\partial_\tau \theta + H + f^{\dagger} \partial_\tau f]. \tag{4.13}$$

We next introduce bosonic operators $X_i = e^{i\theta_i}$ and recast the action into

$$\begin{aligned} S = \int_0^{\beta} d\tau \Bigg[\sum_{i\alpha} f_{i\alpha}^{\dagger} (\partial_\tau + \upsilon_\alpha - \mu - h_i) f_{i\alpha} + \sum_i [\tfrac{1}{2U} \partial_\tau X_i^* \partial_\tau X_i + \tfrac{h_i}{2U} (X_i^* \partial_\tau X_i - c.c) \\ + \rho_i (|X_i|^2 - 1)] + t \sum_{<i,i'>} \Gamma_{\alpha,\alpha'}^{ii'} X_i^* X_{i'} f_{i\alpha}^{\dagger} f_{i'\alpha'} \Bigg], \end{aligned} \tag{4.14}$$

where h_i and ρ_i are Lagrange multipliers imposing the constraints $L_i + \sum_\sigma f^\dagger_{i\sigma} f_{i\alpha} = n_d$ and $|X_i|^2 = 1$, respectively on each site. We have effectively carried out the integration over L by using the relation $L = (i/U)\partial_\tau \theta$. The action (4.14) describes the coupled spinon and rotor degrees of freedom. We will assume that translational symmetry is preserved and decompose (4.14) into two parts by use of the following mean-field ansatz:

$$\begin{aligned} Q_f &= \langle X_i^* X_{i'} \rangle, \\ Q_\theta &= \sum_{\alpha\alpha'} \Gamma^{ii'}_{\alpha,\alpha'} \langle f^\dagger_{i\alpha} f_{i'\alpha'} \rangle. \end{aligned} \tag{4.15}$$

Then, the action in Eq.(4.14) can be written as $S = S_f + S_\theta$, in which

$$S_f = \int_0^\beta d\tau \left[\sum_{i\alpha} f^\dagger_{i\alpha}(\partial_\tau + \upsilon_\alpha - \mu - h) f_{i\alpha} + tQ_f \sum_{<i,i'>} \Gamma^{ii'}_{\alpha,\alpha'} f^\dagger_{i\alpha} f_{i'\alpha'} \right], \tag{4.16}$$

$$\begin{aligned} S_\theta = \int_0^\beta d\tau \Bigg[\sum_i \Big[\frac{1}{2U} \partial_\tau X_i^* \partial_\tau X_i + \frac{h}{2U}(X_i^* \partial_\tau X_i - c.c) \\ + \rho(|X_i|^2 - 1) \Big] + tQ_\theta \sum_{<i,i'>} X_i^* X_{i'} \Bigg]. \end{aligned} \tag{4.17}$$

The chief benefit of the above actions S_f and S_θ is that they are quadratic in spinon and rotor fields, and therefore the calculation of the corresponding Green's function is straightforward. One can simply use Fourier transformation and go to the eigenfunction basis to obtain

$$S_f = \sum_{k,n,j} [\widetilde{f}^\dagger_{knj}(i\omega_n + \varepsilon_j(k))\widetilde{f}_{knj}], \tag{4.18}$$

where k is the momentum, j labels the four sites in a unit cell as well as the effective spin degrees of freedom, and the dispersion of band j is given by $\varepsilon_j(k)$. The $i\omega_n$ are fermionic Matsubara frequencies and $\widetilde{f_{knj}}$ is a linear combination of $f_{k\alpha}$ that diagonalizes the spinon part of the Hamiltonian:

$$H_f = \sum_{i\alpha} f^\dagger_{i\alpha}(\upsilon_\alpha - \mu) f_{i\alpha} + tQ_f \sum_{<i,i'>} \Gamma^{ii'}_{\alpha,\alpha'} f^\dagger_{i\alpha} f_{i'\alpha'}.$$

The rotor action reads

$$S_\theta = \sum_{k,n,j} \left[\widetilde{X}^*_j(k,\nu_n) \left[\frac{\nu_n^2}{U} + \rho + tQ_\theta \xi(k) \right] \widetilde{X}_j(k,\nu_n) \right],$$

where the parameter U has been replaced by $U/2$, so that the atomic limit is treated correctly[133]. Note that we have set $h = 0$, which guaranties that the constraint Eq.(4.11) is satisfied on the mean-field level[133]. The ν_n are bosonic Matsubara frequencies and $\xi(k)$ is related to the spectrum of the rotor Hamiltonian[41] via $\xi_{1,2}(k) = 2\left(1 \pm \sqrt{1 + \sum_{\mu<\nu} \cos(k_\mu/2)\cos(k_\nu/2)}\right)$, and $\xi_{3,4} = -2$. In the sum under the radical, μ, ν run over three values and give max$\{|\xi_i|\}$=6.

The spinon and rotor Green's function can be readily written as

$$G_f(k, i\omega_n) = \frac{1}{i\omega_n + \varepsilon(k)}, \tag{4.19}$$

$$G_\theta(k, i\nu) = \frac{1}{\frac{\nu_n^2}{U} + \rho + tQ_\theta \xi(k)}, \tag{4.20}$$

which can be used to to determine the character of spinon and rotor excitations. We note that the spinons are single-particle-like excitations, while the rotors represent collective excitations.

The self-consistent equations that should be solved to determine the phase boundaries in the phase diagram are (where the rotors are assumed condensed)

$$1 = |X_i|^2 = \frac{1}{4N}\frac{1}{\beta}\sum_{n,j,k}\frac{1}{\frac{\nu_n^2}{U}+\rho+tQ_\theta\xi_j(k)}, \tag{4.21}$$

$$Q_f = -\frac{1}{24N}\frac{1}{\beta}\sum_{n,j,k}\frac{\xi_j(k)}{\frac{\nu_n^2}{U}+\rho+tQ_\theta\xi_j(k)}, \tag{4.22}$$

$$Q_\theta = \sum_{\alpha\alpha'}\Gamma^{ii'}_{\alpha,\alpha'}\langle f^\dagger_{i\alpha}f_{i'\alpha'}\rangle, \tag{4.23}$$

$$4n_d = \frac{1}{N}\sum_{j,k}\Theta(\mu-\varepsilon_j(k)), \tag{4.24}$$

where N is the number of unit cells in the lattice, β is the inverse temperature, and $\Theta(x)$ is the step function. By use of the Matsubara sum[70] $1/\beta\sum_n G_\theta(k,i\nu_n) = \frac{U}{2\sqrt{U(\rho+\xi(k))}}$, the first two equations above in the set starting with (4.21) can be simplified as[41]

$$1 = \frac{1}{4N}\sum_{j,k}\sqrt{\frac{U}{4(\rho+tQ_\theta\xi_j(k))}}, \tag{4.25}$$

$$Q_f = -\frac{1}{24N}\sum_{j,k}\xi_j(k)\sqrt{\frac{U}{4(\rho+tQ_\theta\xi_j(k))}}. \tag{4.26}$$

The rotor condensed phase is characterized by a nonzero value of $Z \equiv \langle e^{i\theta}\rangle$, where the electron operator is proportional to the spinon operator: $c_{i\alpha} = Zf_{i\alpha}$. The condition for condensation is that the gap of the rotor's spectrum $\Delta_g = 2\sqrt{U(\rho+6tQ_\theta)}$ closes. Therefore, right at the phase boundary $\rho = -6tQ_\theta$. Combined with equations Eq.(4.25) and Eq.(4.26), Q_f and the critical U can be determined[41, 70].

4.4 $j = 1/2$-band model: Effect of trigonal distortion

In this section we discuss the slave-rotor mean-field phase diagram of the $j = 1/2$ model studied in Ref. [41] when a C_3 symmetry preserving trigonal distortion of the oxygen octahedra is included[135]. The effect of the trigonal distortion on the atomic t_{2g} levels is given by Eq.(4.2), which describes the compression or expansion of the octahedra along the [111] direction or any equivalent direction in the local coordinate. Fig. 4.1b shows a schematic of this deformation as indicated by the shaded faces of the octagon. This distortion splits the t_{2g} manifold into a singlet $|a\rangle$ with energy $\varepsilon_a = -2\Delta_3$ and doublet $|e'_g\rangle$ with energy $\varepsilon_e = \Delta_3$.

The effect of spin-orbit coupling on the doublet can be understood by noting that the spin-orbit coupling in the subspace spanned by the doublet states acts like a Zeeman field[115],

$$\langle H_{so}\rangle_{e'_g} = \frac{\lambda}{2}\tau^z \otimes \vec{\sigma}\cdot\vec{n}, \tag{4.27}$$

where τ^z and $\vec{\sigma}$ act on the pseudospin space spanned by e'_g states and real spin, respectively. The unit vector $\vec{n}$ points in the direction of the trigonal distortion. Thus a gap may open by tuning the spin-orbit coupling in the presence of a strong distortion, which is consistent with density functional calculations for the iridate $\mathrm{Na_2IrO_3}$[115].

As discussed in Ref. [135], in the non-interacting limit a strong trigonal distortion can turn a strong topological insulator into a metal. We would like to understand to what degree this happens in the presence of interactions, and to what degree the undistorted, interacting phase diagram of Pesin and Balents[41] is changed by distortions. We thus study both interaction and distortion on equal footing. After verifying that our calculations successfully reproduce the phase diagram in Ref. [41], we first consider the case of $\Delta_3 > 0$. Our results are shown in Fig.4.2. The upper panel exhibits the phase diagram with positive distortion. The thick dashed line separates the rotor condensed phase (below the line) from the uncondensed part (above the line). At the non-interacting level and for weak spin-orbit coupling, the system is in the metallic phase. However, a small window of gap opening exists for $\lambda \approx 2.8t - 3.3t$, which is a strong topological insulating (STI) phase with Z_2 invariant (1;000). This small window forms a narrow gapped region in the phase diagram along the $U = 0$ axis. Note the "re-entrant" metallic phase in the presence of distortion is different from the robust insulating phase found in Ref.[41] for large λ, and is qualitatively similar to the non-interacting distortion results found in Ref. [135].

Within the slave-rotor mean-field theory, one finds that a narrow window of STI persists to interactions of order the bandwidth, after which it becomes a tiny sliver. A metallic phase has mostly replaced what would be the STI in the absence of distortions. As interactions are further increased, and a Mott transition occurs to gap out the rotor degree of freedom (above the dashed line), one finds the metal is converted into a gapless Mott insulator (GMI), which is a type of spin liquid with gapless bulk spin excitations[41] described by the spinon Hamiltonian in Eq.(4.19). The only effect of the interaction U is to renormalize Q_f through the self-consistent equations. The large regions of GMI indicates that lattice distortions of $\Delta_3 > 0$ type may be helpful in the realization of a gapless spin liquid state in this class of materials. A very tiny sliver of STI is converted into a topological Mott insulator (TMI) above the line for which the rotors are no longer condensed[41]. Thus, distortions of this type are detrimental to the realization of the TMI phase and suggest this phase may not be stable against lattice distortions.

Next we consider the case of $\Delta_3 < 0$. The phase diagram is shown in the lower panel of Fig.4.2. One distinctive feature compared to the case of positive distortion is that the critical U_c for the Mott transition (dashed line) grows as the spin-orbit coupling strength is increased. A second feature is that a variety of phases appear from the interplay of spin-orbit coupling and correlation effects. At zero interaction,

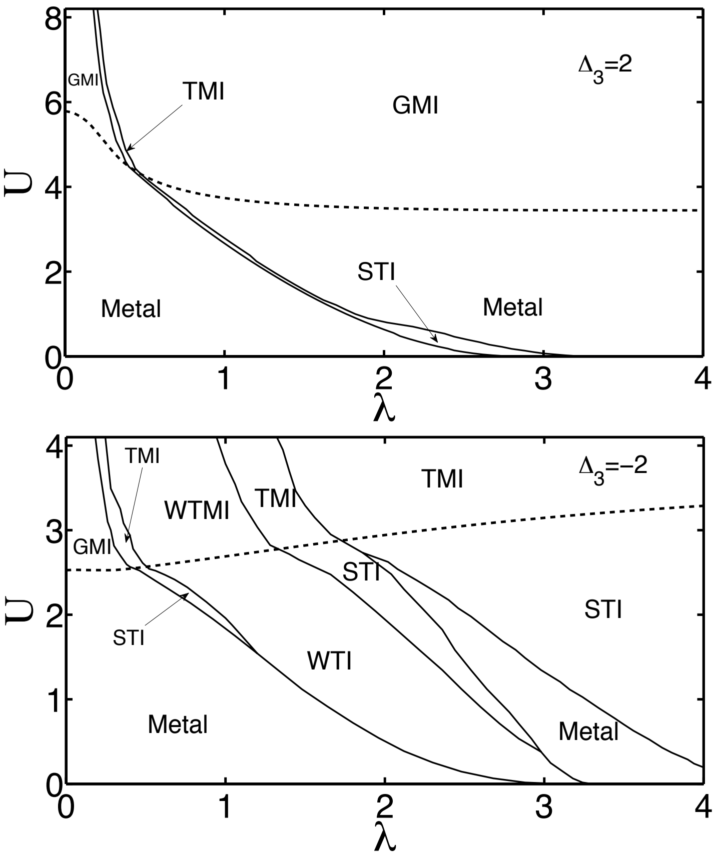

Figure 4.2: Phase diagram of the $j_{eff} = 1/2$-band model corresponding to $n_d = 5$ with positive $\Delta_3 = 2t$ (upper panel) and negative trigonal distortion $\Delta_3 = -2t$ (lower panel). The dashed line separates the rotor condensed phases (below) from the uncondensed phases (above). We set $t = 1$, and the phases labeled are as follows: Strong topological insulator (STI), Weak topological insulator (WTI), Gappless Mott insulator (GMI), Topological Mott insulator (TMI), Weak topological Mott insulator (WTMI) and Metallic phases.

while small and intermediate values of spin-orbit coupling favor the metallic phase, a gap is opened for $\lambda \approx 3.1t - 3.3t$. According to the Z_2 classification[4] this insulating phase is a weak topological insulator (WTI) with Z_2 invariant (0;010), and the small window survives and persists up to intermediate interactions. To the best of our knowledge, this is the first identification of a weak topological insulator in an interacting model. Gapless modes along certain classes of defects may be a way to identify this state in experiment[138].

Another interesting feature of the phase diagram for $\Delta_3 < 0$ is that the correlation effect can drive the metallic and weak topological insulator phases into a strong topological insulating phase. All realized phases in the condensed rotor phase (below the dashed line) have carriers with both spin and charge. When the correlation is strong enough to strip the charge degree of freedom (above the dashed line), those phases will turn into the corresponding phases with only spin degrees of freedom. As before, the metallic and strong topological insulator phases are transformed into the GMI and TMI phases, respectively. Moreover, the weak topological insulator phases realize a novel the weak topological Mott insulator (WTMI) with increased interactions. These latter phases are absent on the undistorted lattice[41] and to the best of our knowledge, is the first time the WTMI phase has been identified in a calculation. It will have gapless thermal transport along the same class of defects that would have gapless charge (and thermal) transport in the WTI phase[138]. We note that there is an accidental gap closing in the TMI phase where two TMI phases are separated by a boundary. However, since the gap closing occurs at an even number of Dirac-like nodes, the topological properties remain unchanged through the gap closing points.

4.5 $j = 3/2$-band model: phase diagram of undistorted lattice

To date, the search for time-reversal invariant insulators in transition metal oxides has primarily focused on the $j = 1/2$ manifold because of its obvious connection to the $s = 1/2$ manifold heavily studied in the theoretical literature thus far[21, 41, 111, 132, 135]. While the $j = 1/2$ manifold is relevant for 1/2-filling ($n_d = 5$), the $j = 3/2$ manifold is relevant for $n_d = 2$ which occurs in $Cd_2Re_2O_7$ and $n_d = 3$ which occurs in $Cd_2Os_2O_7$[139, 140]. In this section we investigate whether topological phases are still possible in the $j = 3/2$ manifold for some range of λ and study the phase diagram in the presence interactions, as was done for $j = 1/2$ in Ref.[41]. In the next section, we will consider the effects of distortion on the $j = 3/2$ phase diagram.

In our calculations, we find that the non-interacting model with $5d^2$ remains metallic for all physical spin-orbit coupling, though we can open a gap by distortion. A direct evaluation of the Z_2 invariant shows that the distortion-induced insulating phase is a trivial insulator. So we will focus on the case with a $5d^3$ electron configuration, with $Cd_2Os_2O_7$ one possible example[139, 140]. In the non-interacting limit and for small values of spin-orbit coupling, we find a metallic phase. However, for $\lambda \approx 2.5t$ a gap opens and a STI appears. The STI phase is characterized by the Z_2 indices $(1;000)$ and survives to moderate interaction. The corresponding phase diagram is shown in Fig. 4.3. The metallic phase is still present in a large portion of the phase diagram if the spin-orbit coupling is not too strong. It results in part from the fact that corresponding band structure coming from the $j = 3/2$ manifold has a larger band width than the upper $j = 1/2$ manifold and therefore has a weaker correlation effect for the same value of U.

The phase boundary that separates the STI phase from the weakly interacting metallic phase can be determined analytically[41]. One notes that in the non-interacting limit a gap is opened at $\lambda \approx 2.5t$. Therefore, the λ and U that respect $\lambda \approx 2.5 Q_f(U)$ form the critical line between the STI and the metal. As in the case of the $j = 1/2$ manifold, the Mott transition between the metallic (STI) phase and the GMI (TMI) phase is characterized by a vanishing amplitude of the rotor condensate at some critical value $U_c(\lambda)$ (given by the dashed line). The GMI-metal transition and its extension to finite temperature, which appears to be a possible Mott transition between a spin-liquid insulator and metal, has already been studied with a possible connection to the experimental observations in $Na_4Ir_3O_8$[120, 121, 141].

The TMI phase is described by a gapped bulk spectrum of the spinon Hamil-

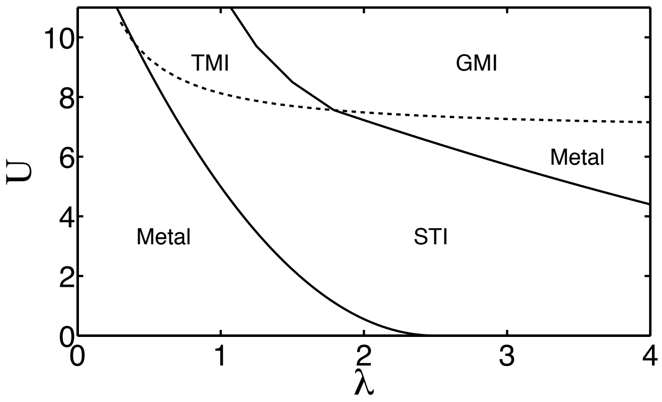

Figure 4.3: Phase diagram of $j = 3/2$-band model on the undistorted lattice for $n_d = 3$. The abbreviations used are the same as those in Fig.4.2. The dashed line separates the rotor condensed phase (below) from rotor uncondensed phase (above). All energies are expressed in units of t, as before. Compared to the corresponding phase diagram for $j = 1/2$ with n_d=5, the STI and TMI occupy a much smaller portion of the phase diagram[41]. The phase diagram for $j = 2/3$ with $n_d = 2$ has no topologically non-trivial phases within our model, even in the presence of distortion.

tonian, and is in the same topological phase appearing in the $j = 1/2$ manifold[41]. It supports gapless surface states of charge-neutral spinons. The same spin-charge separation also occurs in 2D cases[40, 70], where a quantum spin Hall state turns into an exotic quantum spin Hall effect at an intermediate regime of on-site Hubbard interaction. However, the 2D nature of the phase suffers from an instability due to fluctuations of the gauge field[40, 70].

An analysis of symmetries reveals that the Hubbard model in Eq.(4.7) has a $U(1)$ gauge symmetry as the slave-rotor representation of the physical electron in Eq.(4.10) is invariant under the following gauge transformation: $f_{i\alpha} \to e^{i\varphi_i} f_{i\alpha}$ and $\theta_i \to \theta_i - \varphi_i$. In the insulating exotic state, the rotors can be integrated out since the charges are gapped. The resulting theory is a compact $U(1)$ gauge theory coupled to the spinons[142]. The later theory is not stable against the fluctuations of the gauge field as it is a confining compact theory in 2D[143]. Such confinement renders the states unstable in 2D as the gauge fields confine the free spinon-like excitations, effectively removing them as legitimate low-energy excitations[143–145]. While it is believed that the extension of the spin index to N flavors renders it deconfining for sufficiently large N, the value of the critical N is not known[146]. In order to stabilize the edge modes, the gauge fluctuations must be screened by other gapless degrees of freedom. In the 2D case, this can be done by use of a bilayer structure in which the "second" layer contains the necessary gapless degrees of freedom[40]. In spite of the shortcomings of the slave-rotor mean-field theory in 2D, we note that recent quantum Monte Carlo calculations on the Kane-Mele-Hubbard model show a similar phenomenology in some respects at intermediate interaction strength[147–149].

Returning to 3D, we note that in the TMI phase the gapless spinon surface states are coupled to the bulk 3D gauge fields[150]. Thus, the low energy theory of the TMI phase is given by the spinon surface states coupled to the 3D gauge fields. This theory is believed to be stable[41], as the gauge propagator is suppressed so that the spinons become better defined (the self-energy scales as the energy itself, up to logarithmic corrections)[150]. Thus, the lowest order calculation in the U(1) gauge fluctuations suggests they are marginal; a more careful scaling analysis suggest they are actually marginally irrelevant[150].

Unlike the STI phase, the surface states of the TMI phase can not be characterized by electrical transport measurements due to the charge neutrality of the spinons on the surface of the TMI. Moreover, because this neutrality, there are no Friedel oscillations around a charged impurity on the surface. However, spinon surface states of the TMI can be detected in thermal measurements, and by the way in which they modify the RKKY interaction between magnetic impurities at the surface[150]. In the GMI phase, on the other hand, the bulk specific heat behaves[141] as $C \sim T\ln(1/T)$, while in the metallic state it behaves as $C \sim T$.

4.6 $j = 3/2$-band model: effect of distortions

Having obtained the phase diagram of the undistorted $j = 3/2$ model in Fig.4.3, we now study the effect of the local distortion of octahedra introduced in Sec.4.2. We focus on two kinds of distortion with different symmetries: (1) a trigonal distortion of oxygen octahedra that preserves the C_3 symmetry, and (2) a compression and elongation of the oxygen octahedra that preserves the C_4 symmetry. We use parameter Δ_3 to describe the C_3 distortion and Δ_4 to describe the C_4 distortions. The relevant Hamiltonians are given in (4.2) and (4.3).

We restrict our attention to the weak and intermediate interaction limit, so we neglect possible magnetic phases that could become favorable in the strong correlation limit. In that limit geometrical distortions could alter the isotropic antiferromagnetic superexchange and the combined effects of spin-orbit coupling and distortion can give rise to an anisotropic pseudo-spin Heisenberg model for some perovskites[130].

4.6.1 Trigonal Distortion of Oxygen Octahedra

We first consider the trigonal distortion in Eq.(4.2) on the $j = 3/2, n_d = 3$ manifold. The resulting phase diagrams for fixed Δ_3 and fixed U are shown in Fig.4.4. We find the general structure of the phase diagram depends on Δ_3 in a complicated way. As one example, in the upper panel of Fig.4.4 we show the case of fixed trigonal distortion $\Delta_3 = 2t$. In that case, we find that the non-interacting model is dominated by the metallic phase, which is analogous to the trigonal distortion driven metallic phase on the $j = 1/2$-band model, as discussed in Sec.4.4 and also in Ref. [135]. The gap opens at $\lambda \approx 1.8t$ and closes at $\lambda \approx 2.4t$. Therefore, in the presence of trigonal distortion only a small window of λ admits the STI phase in the non-interacting limit. However, this small window grows with small but increasing interaction strength which helps to stabilize the STI phase[41]. The metallic phase, however, remains dominant for $\lambda \gtrsim 2.4t$, even in the presence of interaction. We note that the boundary separating STI phase from the metallic phase around $\lambda \approx 2.4t$ is not exactly but very close to a straight line.

From the phase diagrams shown in Fig.4.4, it is clear that trigonal distortion has two remarkable effects. First, compared with the undistorted phase diagram in Fig.4.3, it is evident that the distortion drives the system across the Mott transition (indicated by the dashed line) at rather smaller critical values of interaction $U_c(\lambda)$. This finding suggests that the distortion may help stabilize the TMI phase in a physically realistic range of interactions before the system undergoes a transition to a magnetically ordered phase at strong interaction. The considerable decrease of the critical Mott transition point can be traced back to the effect of distortion on the $j = 3/2$ manifold. Without distortion this manifold represents four degenerate states which in turn contribute to the formation of bands. However, upon the inclusion of distortion this degenerate manifold splits into two Kramers pairs separated by amount of energy related to the strength of the distortion, *i.e.* Δ_3. The corresponding bands will also be separated by the same energy scale. Thus with distortion, we are dealing with a half-filled band, with an effective bandwidth is reduction. So, a smaller Hubbard interaction is needed for the Mott transition[111].

Second, distortion stabilizes the TMI phase by extending its region of the phase diagram in comparison with the small region seen around $U \approx 9$ in the undistorted lattice. (See Fig.4.3.) We note that the GMI phase is found at both small and large spin-orbit coupling in the presence of a trigonal distortion.

The lower panel in Fig.4.4 explicitly shows the effect of distortion at fixed interaction $U = 4t$, which is relevant to the application of pressure, for example. At small distortions $\Delta_3 \lesssim t$, most of the phase diagram is dominated by metallic and STI phases. One can think of distortion as a driving parameter that transfers system from the rotor condensed phase (below the dashed line) into uncondensed phase (above the dashed line). Although the actual form of the geometrical distortion could be more complicated than the one we considered here, the result is appealing as this minimal distortion can drive the system across a variety of phases. Starting from the STI phase at zero distortion, the ground state of the system can exhibit a metallic behavior or perhaps transits to GMI and TMI phases with increased distortion. We hope this observation will help motivate new classes of experiments searching for exotic quantum phases in correlated materials with strong spin-orbit coupling.

4.6.2 Compression and Elongation of the Oxygen Octahedra

In this subsection we study the effects of the second type of distortion, Eq.(4.3), which describes a tetragonal distortion of the octahedron along one of its axes. This distortion preserves the C_4 rotation of an octahedron about the elongated axis, say the z-axis in Fig.4.1b. At zero spin-orbit coupling, the degeneracy of the t_{2g} manifold will be lifted by this distortion. Compression of the octahedron, $\Delta_4 > 0$, lowers the energy of the d_{xy} orbital (which is at zero energy by our convention) below that of the doubly degenerate d_{yz} and d_{zx} orbitals, with energy Δ_4. An elongation (expansion), $\Delta_4 < 0$, of an octahedron lowers the energy of the d_{yz} and d_{zx} orbitals relative to d_{xy}. This rearranging orbitals strongly affects the magnetic properties of the double perovskites in the strong interaction limit[130].

When spin-orbit coupling is present, the levels split in a more complicated way. Similar to Eq.(4.27) for the e_g' manifold, the spin-orbit coupling results in the following effective Hamiltonian for a proper linear combination of $|yz\rangle$ and $|zx\rangle$ states[115]:

$$\langle H_{so}\rangle_{yz,zx} = -\frac{\lambda}{2}\tau^z \otimes \sigma^z, \tag{4.28}$$

where τ acts within the doublet $\{-\frac{1}{\sqrt{2}}(|yz\rangle + i|zx\rangle), \frac{1}{\sqrt{2}}(|yz\rangle - i|zx\rangle)\}$, and σ is the usual Pauli matrix of real spin. Note that the spin-orbit coupling acts like a Zeeman coupling so that the effective magnetic field has opposite direction in different states of the doublet, therefore, the time-reversal symmetry is preserved (evident as well from the Hamiltonian (4.7)).

The effect of distortion on the spin-orbit basis can also be treated in the same way. In particular, we consider its effect on the quadruplet $j = 3/2$ manifold. (See Appendix.) With distortion the following states are obtained:

$$\begin{aligned}
|\psi_1\rangle &= -\frac{1}{\sqrt{2}}(|yz\uparrow\rangle + i|zx\uparrow\rangle), \\
|\psi_2\rangle &= \frac{1}{\sqrt{2}}(|yz\downarrow\rangle - i|zx\downarrow\rangle),
\end{aligned} \tag{4.29}$$

with energy $\varepsilon_{1,2} = \frac{1}{2}(2\Delta_4 - \lambda)$ and

$$\begin{aligned}
|\psi_3\rangle = C\,[-f(\lambda,\Delta_4)|yz\downarrow\rangle - if(\lambda,\Delta_4)|zx\downarrow\rangle + |xy\uparrow\rangle]\,, \\
|\psi_4\rangle = C\,[f(\lambda,\Delta_4)|yz\uparrow\rangle - if(\lambda,\Delta_4)|zx\uparrow\rangle + |xy\downarrow\rangle]\,,
\end{aligned} \tag{4.30}$$

with energy $\varepsilon_{3,4} = \frac{1}{4}(2\Delta_4 + \lambda - \sqrt{4\Delta_4^2 + 4\Delta_4\lambda + 9\lambda^2})$. Here C is a normalization constant depending on f. Note that in Eq.(4.30) f is a function of its arguments with $f \to 1$ as $\Delta_4 \to 0$. In the limit of vanishing distortion, the above sates $|\psi_{1,2}\rangle$ and $|\psi_{3,4}\rangle$ reduce to the four sates $|\frac{3}{2}, \pm\frac{3}{2}\rangle$ and $|\frac{3}{2}, \pm\frac{1}{2}\rangle$ of the quadruplet $j = 3/2$ manifold, respectively. Note the $|\psi_{1,2}\rangle$ keeps the character of $j^z = \pm\frac{3}{2}$ states even for $\Delta_4 \neq 0$. With electron occupation $n_d = 3$ and for $\Delta_4 > 0$ ($\Delta_4 < 0$), the states $|\psi_{1,2}\rangle$ ($|\psi_{3,4}\rangle$) form a half filled band, and we will see that the C_4 distortions strongly affect the phase diagram found in Fig.4.3 for the undistorted lattice.

Fig.4.5 depicts the phase diagram of the $j = 3/2$ model with compression (elongation) distortion in upper (lower) panel. While both compression and elongation of octahedra possess almost the same critical (dashed) line for the Mott transition, the topological phases occupy rather different regions. For example, the case of compression does not support a STI phase, while elongation does. For strong compressional distortion $\Delta_4 > 0$, the bands are mainly comprised of the states $|\psi_{1,2}\rangle$, which are not spin-orbital *entangled*. The states $|\psi_{3,4}\rangle$, on the other hand, are spin-orbital entangled states. Even for elongation, most portions of the condensed phase (below the dashed line) is dominated by the metallic phase even in the presence of interaction.

For both signs of the C_4 distortions, strong interactions open up a gap in the bulk spinon spectrum turning the GMI phase into the TMI phase as shown Fig.4.5. For $\Delta_4 > 0$, a weaker distortion may extend the boundary of the TMI phase towards weaker interactions, and perhaps open a region with a STI phase. This is because at weaker distortion there would be a considerable contribution from unentangled states in the formation of the bands. This is clearly seen in the lower panel of Fig.4.5, where a finite region with a STI phase is established. If the spin-orbit coupling is kept fixed, at very strong distortion the coefficient f in Eq.(4.30) tends to zero, and therefore the states become unentangled. This may partly explain why at small interaction the metallic phase is dominant. However, the lower panel of Fig.4.5 reveals that interactions can drive the formation of strong topological insulators even when the STI phase is not present in the non-interacting limit, as it is in most of the cases considered previously. A two dimensional analogue of this problem has been studied elsewhere[18, 37, 38, 47, 151, 152], where it is shown that the interaction-driven insulating phases with nontrivial topology can be found on a variety of different lattices.

While the distortion favors the metallic phase in the weak interaction limit and the GMI phase in the strong limit (above the Mott transition) compared to the non-distorted case (Fig.4.3), it is possible that strong disorder can transform the metallic phase and GMI into topological phases, the so called topological Anderson insulator[68, 69, 153]. In particular, the effect of disorder on the GMI phase would be an interesting problem.

4.7 Summary

In this work we investigated the phase diagram of some transition metal oxides with 5*d* orbitals on the pyrochlore lattice. We focused on the interplay between electron correlation, spin-orbit coupling, and distortion. Our main results are summarized in the phase diagrams presented in Figs. 4.2-4.5 obtained within the slave-rotor mean-field theory.

Examples of pyrochlore transition metal oxides include $A_2Ir_2O_7$ (A=Y, Pr, Eu or other rear-earth elements), $Cd_2Os_2O_7$, and $Cd_2Re_2O_7$, in which different transition ions favors either $j = 1/2$ or $j = 3/2$ manifolds to be partially occupied[139, 140]. A central feature of our work was to considered distortion of local oxygen octahedra surrounded the transition ion in the presence of interactions. Such distortions are inherent to the systems we studied[135, 154].

We first studied the effect of trigonal distortion on the $j = 1/2$ phase diagram already obtained in Ref. [41]. In the noninteracting limit, we found the distortion destabilized the STI phase and turned it into a metallic phase[135]. (See Fig.4.2.) However, a $\Delta_3 < 0$ can also help stabilize a weak topological insulating (WTI) phase which becomes a weak topological Mott insulator (WTMI) above the Mott transition line. To the best of our knowledge, these features have not been obtained in previous interacting models before.

We also extended the study of interacting topological insulators in transition metal oxides to include the case where the $j = 3/2$ manifold is partially filled. (See Fig.4.3.) We found that strong spin-orbit coupling opens a gap in the non-interacting spectrum and the STI appears, along with a metallic phase at small spin-orbit coupling. These phases persist in the presence rather large interactions interaction due to the large band width of the non-interacting model, and eventually at large enough interactions the Mott phases appear. Most portions of the Mott phase are identified as a gapless Mott insulator (GMI). However, at some intermediate regime of spin-orbit coupling, $1 \lesssim \lambda \lesssim 2$, the TMI phase is obtained.

Trigonal distortion extends the TMI phase to a wider range of interaction and spin-orbit coupling. (Fig.4.4.) Trigonal distortion also decreases the critical interaction for the Mott transition. Moreover, we showed that the distortion can serve as a tuning parameter in which the transition between a variety of phases could occur by distorting the lattice, though a more realistic form of distortion could have a more complicated evolution of the phases. We also examined the effect of tetragonal distortion of octahedra caused by an elongation or compression of an octahedra along one of its axis. (Fig.4.5.) The STI phase is found to be very delicate with respect to this type of distortion, and most of the phase diagram is occupied by either the metallic phase the the GMI. For strong enough distortion, however, interaction can restore both STI and TMI phases. The restoration of these phases is an example of "interaction-induced" topological phases as these phases do not persist down to zero interaction.

One might wonder to what extent the slave-rotor mean-field results should be trusted. Is there an alternative method that can be used to obtain a TMI phase? As we mentioned earlier, quantum Monte Carlo methods applied to the 2-d Hubbard model on the honeycomb lattice seem to suggest[147–149] that there is an intermediate, gapped phase that lives over a similar region of the phase diagram that the slave-rotor method predicts a 2-d TMI (recall that the slave-rotor method is not expected to be reliable in 2-d). This may suggest that there is indeed a state with fully gapped bulk excitations, but with gapless spin excitations on the boundary. However, it may be that the slave-rotor method fails to correctly capture the collective nature of the "true" low-energy spin-excitations by forcing them into a single-particle mean-field formalism. One may also ask about the reliability of the slave-rotor method more generally. The original work of Florens and Georges[133, 134] on Hubbard models shows a favorable comparison with dynamical mean-field theory and Gutzwiller projection for quantities like the quasi-particle weight and effective mass below and just above the Mott transition. Finally, the references contained in the work of Pesin and Balents[41] provide further support for the reliability of the slave-rotor method when compared with path-integral renormalization group calculations and variational cluster methods on frustrated lattices. Taken together, it seems the method works reasonably well in situations where interactions are not too strong and no magnetic order is expected. Nevertheless, a more careful study of the possibility of a TMI phase within a more sophisticated class of calculations remains highly desirable and we hope this work will help to inspire such studies.

Regarding the physics of pyrochlore oxides, a number of interesting directions for future study remain. For example, it would be highly desirable to have a better understanding of the specific form of lattice distortions that occur in nature and what their influence is in terms of candidate topological phases. It would also be interesting to obtain a better understanding of disorder on the interplay of correlations, spin-orbit coupling, and lattice distortions. Finally, we note that even more exotic possibilities exist for novel phases when certain conditions are met[155–157]. An improved understanding of how likely the conditions for these “fractional” phases with non-trivial ground state degeneracy are to be met in real materials would be welcome.

As we restricted ourselves to interactions that were not too strong, we did not invoke the possible magnetic phases that could be more favorable at very strong Coulomb interaction. The magnetic phase is interesting in its own right as the pyrochlore lattice has a geometrically frustrated structure. The latter property along with the proximity to the metallic phases can enhance the quantum fluctuations. Hence, even the nearest-neighbor antiferromagnetic interaction may stabilize a spin-liquid phase on the pyrochlore lattice[158–160]. Besides the antiferromagnetic interaction, $j = 1/2$ magnetic models that include some additional interactions such as Dyzaloshinsky-Moriya and other anisotropic interactions can help sustain ordering on the pyrochlore lattice at low temperatures[161, 162]. However, the situation is more complicated for the $j = 3/2$ model: because of orbitally-dependent exchange, biquadratic (forth order in spin operators) and triquadratic (sixth order in spin operators) interactions arise[136]. These new interactions give rise to some exotic phases in double perovskites[136] and tetragonal distortion of octahedra can result in an anisotropic pseudo-spin antiferromagnetic exchange Heisenberg model[130]. Such models can be developed for our model with distortion, too. Indeed, what magnetic phases become favorable and how they are related to the topological phases we addressed here are interesting open problems.

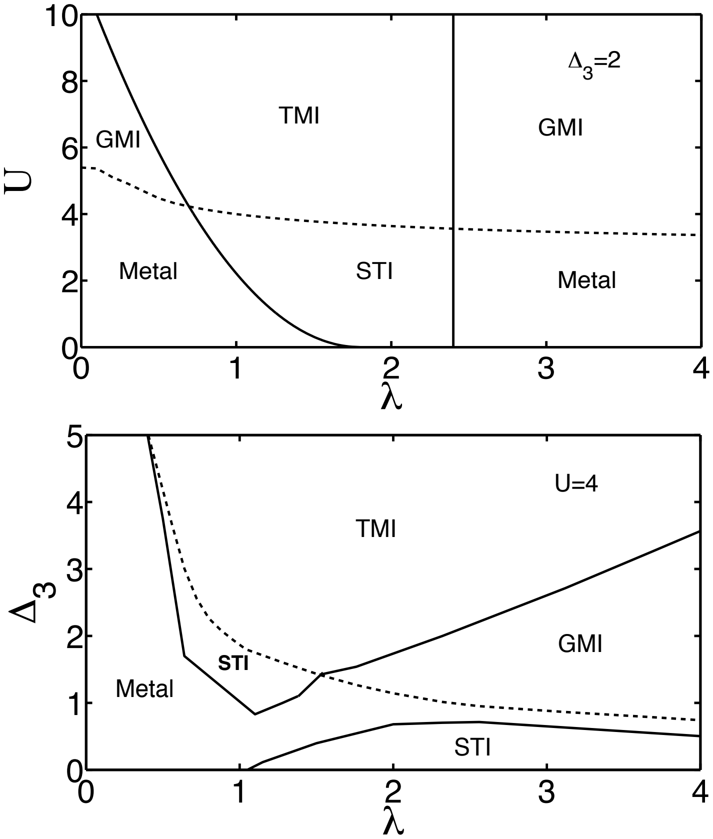

Figure 4.4: Phase diagram of the $j = 3/2$ band model with $n_d = 3$, including the trigonal distortion of the octahedra. The labeling of the phases is the same as that used in Fig.4.2. In the upper panel $\Delta_3 = 2t$. In the lower panel the interaction is fixed at $U = 4t$ and the strength Δ_3 of the trigonal distortion is varied, illustrating possible phases that may arise upon the application of pressure to a real system. All energies are expressed in units of t. In both phase diagrams the dashed line separates the rotor uncondensed phase (above) from the condensed phase (below). We note the "pocket" of STI around $\lambda \approx 1, \Delta_3 \approx 1.5$ in the lower figure has a numerically difficult to determine boundary with the metallic phase; we have present our best assessment.

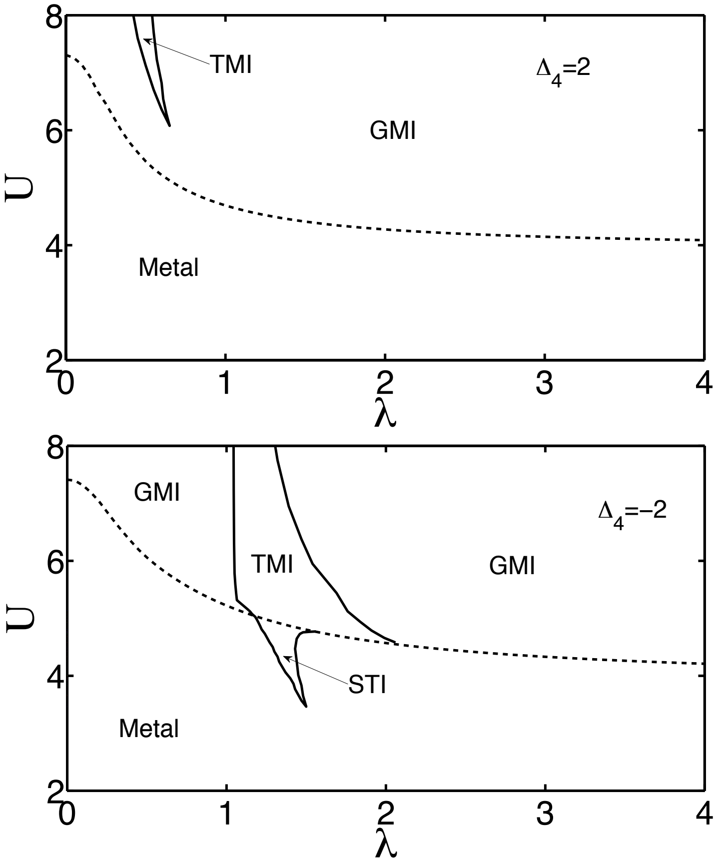

Figure 4.5: Phase diagram of the $j = 3/2$-band model with C_4 tetragonal distortion. The upper and lower panel correspond to compression and elongation distortion of octahedra, respectively. We set $\Delta_4 = 2t$ for compression and $\Delta_4 = -2t$ for elongation. All energies are expressed in units of t. In both phase diagrams the dashed line separates the rotor uncondensed phase (above) from the condensed phase (below). Note that for these values of distortion, the topological phases are interaction-driven, *i.e.* they do not extend down to the non-interacting limit as they do in Figs. 2-4.

Chapter 5

Doping the Kane-Mele-Hubbard Model: A Slave-Boson Approach

5.1 Introduction

Recent years have seen growing interest in topological band insulators (TBI)[6–8]. While in the fractional quantum Hall effect the Coulomb interaction is necessary for the topological order, the concept of TBIs can be readily appreciated in the framework of noninteracting Bloch band theory where spin-orbit coupling is responsible for a possibly nontrivial Z_2 topological order[6–8]. A TBI has a gap in the bulk excitation spectrum and time-reversal symmetry protected gapless modes on the boundary. Because in nature all materials possess Coulomb interactions, understanding the role of interactions is one of the fundamental challenges in the field of topological insulators.

One can ask if it is possible for interactions to induce TBIs. The answer is affirmative. Indeed, there have been a number of works that address this question with different models that contain *no intrinsic spin-orbit coupling*. For example, Raghu *et al.*[37] showed it is possible to have an interaction-driven TBI with spontaneously broken SU(2) symmetry (with spontaneously generated spin-orbit coupling) from an extended Hubbard model on the honeycomb lattice. This idea has been successfully applied to the kagome lattice[18] and the decorated honeycomb lattice[18] in 2D[47, 151, 163–166], and the diamond lattice in 3D[38]. The key is to have the correct amount of "generalized" spin-orbit coupling that originates from the Hartree-Fock mean-field decoupling of the interaction terms on nearby sites.

Another equally important question is the fate of TBIs with intrinsic spin-orbit coupling upon the inclusion of Coulomb interaction. On one hand, by the argument of adiabatic continuity, it is argued that a TBI should be stable to weak interactions as long as the bulk gap is not closed[3, 4]. However, when interactions grow too strong, one has a good reason to believe that spin-charge separation develops and Mott physics will appear[41]. In this regime, one expects that a slave particle approach which starts with an explicit decomposition of the electron into charge and spin degrees of freedom would qualitatively capture the physics of the interactions. Indeed, back in 2008 Young *et al.*[40] employed a slave-rotor mean-field approach to study a double layer honeycomb lattice where a fractionalized quantum spin Hall (FQSH) effect could be found. A FQSH state differs from a quantum spin Hall state in that neutral spinons instead of physical electrons carry a nontrivial Z_2 topology. As a result, a gapless spinon excitation is guaranteed to appear along the edge. Applying similar methods, others[70, 167] used the same approach to study the Kane-Mele-Hubbard model [our Eq.(5.1)] on the single-layer honeycomb lattice and concluded that this phase could be stabilized if the two dimensional U(1) gauge field is screened by an additional metallic layer so that the gauge fluctuations are suppressed.

In three dimensional systems, Pesin and Balents[41] studied heavy transition-metal oxides on the pyrochlore lattice and proposed a three dimensional counterpart of the FQSH, termed as a "topological Mott insulator" (TMI). A TMI is one example of a U(1) spin liquid (SL) in three dimension and is believed to be more stable to gauge fluctuations than its two dimensional counterpart[150]. Later, Kargarian[19] extended Pesin and Balent's results and investigated the interplay between interactions and distortion in the same system. Based on these works, it may appear that the concept of the FQSH in two dimensions and the TMI in three dimensions depends crucially on the slave-rotor approach, which by its construction transfers the topology of physical electrons to neutral spinons and makes access to fractionalized states possible.

The extent to which a slave-rotor mean-field approach is reliable can be checked with more controlled numerical simulations. Recent quantum Monte Carlo and cellular dynamical mean-field studies have shed light on the weak and intermediate interaction regimes in two dimensions[147, 149, 168, 169, 169]. In a pioneering quantum Monte Carlo study, Meng *et al.*[168] investigated the Hubbard model on the honeycomb lattice at half-filling and discovered the existence of a gapped spin liquid in a small window in the intermediate interaction regime ($3.5t < U < 4.3t$). Later, spin-orbit coupling was included and the spin liquid phase was found to be stable for small spin-orbit coupling [147] and for finite temperatures.[169] At half-filling, the above quantum Monte Carlo studies are free of the sign problem and considered to be accurate. Of particular interest is the nature of the spin liquid, which has been addressed in a number of works[55, 170–172]. Very recent work has indicated that beyond a critical interaction strength and spin-orbit coupling strength (larger than that explored in quantum Monte Carlo) yet another novel phase may appear with fractionized excitations and a non-trivial ground-state degeneracy[173] and attention has been drawn to transition metal oxide interfaces[164–166, 174].

In this paper we aim to better understand the intermediate interaction regime where a gapped SL phase appears. We are particularly interested in the fate of the SL[175] upon doping. This is a regime where quantum Monte Carlo simulations suffer from the sign problem[176] and the slave-rotor mean-field approach may encounter severe limitations[133] leaving few tools available for its study. We will follow Ref. [171] and use a generalized U(1) slave-boson mean-field approach to study the cases of half-filling *and* doping. Such an approach has been widely used in doped *t*-*J* models in the context of high temperature superconductivity[99]. *We stress that we do not expect the slave-boson mean-field approach to represent a good solution to the Kane-Mele-Hubbard model in all regimes.* Instead, we argue that it gives a reasonably good description of the gapped SL at intermediate regime (based on a quantitative comparison with QMC and CMDFT) and its transition to a superconducting state upon doping. For a general review of Hubbard model, we refer interested readers to Ref. [177].

This chapter is organized as follows. In Sec. 5.2 we introduce the slave-boson representation for the Kane-Mele-Hubbard model. In Sec. 5.3 we describe our slave-boson mean-field results for the cases of half-filling and doping. Finally, in Sec. 5.4 we give the main conclusions of this work. In App.6 we provide some lengthy self-consistency formulas used to obtain our results.

5.2 The slave-boson approach

We start with the Kane-Mele-Hubbard model on the honeycomb lattice,

$$H = -t\sum_{\langle ij\rangle} c^\dagger_{i,\sigma}c_{j,\sigma} + U\sum_i n_{i\uparrow}n_{i\downarrow} + i\lambda_{SO}\sum_{\langle\langle i,j\rangle\rangle,\sigma}\sigma\nu_{ij}c^\dagger_{i,\sigma}c_{j,\sigma} \tag{5.1}$$

where t, U, and $\lambda_{\rm SO}$ are the nearest neighbor hopping energy, the strength of the on-site repulsion, and the second-neighbor spin-orbit coupling strength, respectively. Here $c_{i\sigma}$ ($c^\dagger_{i\sigma}$) annihilates (creates) an electron with spin σ on site i and $\nu_{ij} = \pm 1$ depending on if the electron makes as "right" or "left" turn when going from i to j[3, 4].

The general U(1) slave-boson approach decomposes an electron operator into a bosonic operator that carries the charge degree of freedom and a fermionic spinon operator that carries the spin degree of freedom:[99, 171, 178–180]

$$c^\dagger_{i,\sigma} = f^\dagger_{i,\sigma}h_i + \sigma d^\dagger_i f_{i,-\sigma}, \tag{5.2}$$

where i is the site index, and h_i and d_i are the bosonic holon operator and the bosonic doublon operator, respectively. Such a decomposition makes the idea of spin-charge separation explicit and one expects that it will describe the physics of intermediate (and possibly strong) interactions reasonably well.

There are four states, $|0\rangle, |\uparrow\rangle, |\downarrow\rangle$, and $|\uparrow\downarrow\rangle$, at each site. Each state can be thought to have some new particle operator acting on some vacuum state: $|0\rangle = h^\dagger|vac\rangle$, $|\uparrow\rangle = f^\dagger_\uparrow|vac\rangle$, $|\downarrow\rangle = f^\dagger_\downarrow|vac\rangle$ and $|\uparrow\downarrow\rangle = d^\dagger|vac\rangle$. Physically, one can think of $h^\dagger_i h_i$ as the number of empty occupancies at site i, $f^\dagger_{i\sigma}f_{i\sigma}$ the single occupancy with spin σ, and $d^\dagger_i d_i$ the double occupancy. One can show that Eq. (5.2) guarantees that the matrix elements of physical states are correct. The completeness of the basis implies the constraint

$$h_i^\dagger h_i + \sum_\sigma f_{i,\sigma}^\dagger f_{i,\sigma} + d_i^\dagger d_i = 1, \tag{5.3}$$

which also preserves the anticommunication relations of $c_{i,\sigma}$ and $c_{i,\sigma}^\dagger$. This constrain can be enforced with a Lagrange multiplier λ_i in the Hamiltonian.

There is also another constraint related to the filling fraction of electrons: $c_{i\sigma}^\dagger c_{i\sigma} = f_{i\sigma}^\dagger f_{i\sigma} + d_i^\dagger d_i$ where some extra terms which have zero matrix elements in the physical states have been thrown away[99, 171, 178–180]. Therefore,

$$\sum_\sigma \langle c_{i\sigma}^\dagger c_{i\sigma} \rangle = 1 + \langle d_i^\dagger d_i \rangle - \langle h_i^\dagger h_i \rangle \equiv 1 + x, \tag{5.4}$$

where x is the electron doping. We can incorporate the constraint (5.4) by another Lagrange multiplier μ_i in the Hamiltonian.

With the slave-boson representation described above, the Kane-Mele-Hubbard model can be written as

$$\begin{aligned} H = -t \sum_{\langle ij \rangle} [\chi_{ij}^f \chi_{ji}^b + \Delta_{ij}^{f\dagger} \Delta_{ij}^b + h.c.] + \lambda_{\mathrm{SO}} \sum_{\langle\langle ij \rangle\rangle} [\chi_{ij}^{f\prime} \chi_{ji}^{b\prime} + \Delta_{ij}^{f\dagger\prime} \Delta_{ij}^{b\prime} + h.c.] + U \sum_i d_i^\dagger d_i \\ - \sum_i \lambda_i (h_i^\dagger h_i + \sum_\sigma f_{i\sigma}^\dagger f_{i\sigma} + d_i^\dagger d_i - 1) - \sum_i \mu_i d_i^\dagger d_i - h_i^\dagger h_i - x) \end{aligned} \tag{5.5}$$

where the following order parameters are defined for nearest neighbor (NN) sites $\langle ij \rangle$: $\chi_{ij}^f = \sum_\sigma f_{i\sigma}^\dagger f_{j\sigma}$, $\chi_{ij}^b = h_i^\dagger h_j - d_i^\dagger d_j$, $\Delta_{ij}^f = \sum_\sigma \sigma f_{i-\sigma} f_{j\sigma}$, $\Delta_{ij}^b = d_i h_j + h_i d_j$ and for the next nearest neighbor (NNN) sites $\langle\langle ij \rangle\rangle$: $\chi_{ij}^{f\prime} = \sum_\sigma i\nu_{ij} \sigma f_{i\sigma}^\dagger f_{j\sigma}$, $\chi_{ij}^{b\prime} = h_i^\dagger h_j - d_i^\dagger d_j$, $\Delta_{ij}^{f\prime} = \sum_\sigma i\nu_{ij} f_{i-\sigma} f_{j\sigma}$ and $\Delta_{ij}^{b\prime} = d_i h_j + h_i d_j$.

We proceed with a mean-field approximation in which the spinon part and the boson part decouple from each other. We will restrict ourselves to a search for phases preserving translational symmetry. The simplest phase is the one that does not break any symmetry of the Hamiltonian. In this case each type of order parameter does not depend on the site indices. For example,for any $\langle ij \rangle$. We then have $H_{MF} = H_f + H_b + H_{const}$ where

$$H_f = \sum_{\mathbf{k}\sigma} [-t\chi_b g(\mathbf{k}) f^\dagger_{\mathbf{k}A\sigma} f_{\mathbf{k}B\sigma} - t\Delta_b g(\mathbf{k})\sigma f^\dagger_{\mathbf{k}A\sigma} f^\dagger_{-\mathbf{k}B-\sigma} + \lambda_{\mathrm{SO}}\chi'_b \sigma(f^\dagger_{\mathbf{k}A\sigma} f_{\mathbf{k}A\sigma}$$
$$-f^\dagger_{\mathbf{k}B\sigma} f_{\mathbf{k}B\sigma}) g_1(\mathbf{k})] - \lambda \sum_{\mathbf{k}\sigma\alpha} f^\dagger_{\mathbf{k}\alpha\sigma} f_{\mathbf{k}\alpha\sigma} + \lambda_{\mathrm{SO}}\Delta'_b \sum_{\mathbf{k}} (f^\dagger_{\mathbf{k}A\uparrow} f^\dagger_{-\mathbf{k}A\downarrow} - f^\dagger_{\mathbf{k}B\uparrow} f^\dagger_{-\mathbf{k}B\downarrow}) + h.c.,$$

$$H_b = \sum_{\mathbf{k}\alpha} [(U - \lambda - \mu - \lambda_{\mathrm{SO}}\chi'_f g_2(\mathbf{k})) d^\dagger_{\mathbf{k}\alpha} d_{\mathbf{k}\alpha} + (\mu - \lambda + \lambda_{\mathrm{SO}}\chi'_f g_2(\mathbf{k})) h^\dagger_{\mathbf{k}\alpha} h_{\mathbf{k}\alpha}$$
$$+\lambda_{\mathrm{SO}}\Delta'_f g_2(\mathbf{k}) d_{\mathbf{k},\alpha} h_{-\mathbf{k},\alpha}] - \sum_{\mathbf{k}} g(\mathbf{k}) [t\chi_f (h^\dagger_{\mathbf{k}A} h_{\mathbf{k}B} - d^\dagger_{\mathbf{k}A} d_{\mathbf{k}B}) + t\Delta_f(-d_{\mathbf{k}A} h_{\mathbf{k}B} + h_{-\mathbf{k}A} d_{\mathbf{k}B})] + h.c.$$

and the constant energy term $H_{const} = 6Nt(\chi_b\chi_f + \Delta_b\Delta_f) + 2N(\lambda + x\mu) - 12N(\chi'_b\chi'_f + \Delta'_b\Delta'_f)$ where N is the number of unit cells. In Eq.(5.6) and (5.6) we have used $\alpha = A, B$ to denote the two sublattices of the honeycomb lattice. We have defined $g(\mathbf{k}) \equiv 1 + \exp(-ik_2) + \exp(ik_1 - ik_2)$, $g_1(\mathbf{k}) \equiv 2[\sin k_2 - \sin k_1 + \sin(k_1 - k_2)]$ and $g_2(\mathbf{k}) \equiv 2\,[\cos k_1 + \cos k_2 + \cos(k_1 - k_2)]$ with $k_i = \mathbf{k}\cdot\mathbf{a}_i$. *We stress that both spinon and bosonic Hamiltonians have generic hopping terms and pairing terms and they are not identical to the pairing of physical electrons, as we will explain later in our paper.*

After a mean-field approximation, it is straightforward to solve the spinon Hamiltonian (5.6) and the bosonic Hamiltonian (5.6) to obtain the ground state energy at zero temperature. Self-consistency equations are obtained via the first derivative of the ground state energy with respect to various order parameters. (See the Appendix for details.) However, one has to consider possible Bose-Einstein condensations when dealing with a bosonic Hamiltonian. Since we have assumed that the translation symmetry remains unbroken, we expect a Bose-Einstein condensation can only take place at $\mathbf{k} = 0$. Bearing this in mind, we can explicitly separate the $\mathbf{k} = 0$ term from the $\mathbf{k} \neq 0$ terms. We define $d_\alpha \equiv 1/\sqrt{N}\langle d_{\mathbf{k}=0,\alpha}\rangle$ and $h_\alpha \equiv 1/\sqrt{N}\langle h_{\mathbf{k}=0,\alpha}\rangle$, both of which can acquire finite values in a condensed phase of the bosons. Thus, d_α^2 and h_α^2 are the fraction of doublons and holons on sublattice $\alpha = A, B$.

We will also consider phases that break certain symmetries (lattice rotational symmetry, for example) at large U. This allows us to make connections to an antiferromagnetic state, which is difficult to capture within the slave-boson mean-field approach to the Kane-Mele-Hubbard model[171]. In the next section we turn to a detailed description of the results of our mean-field study. We find many features reminiscent of previous studies at half-filling, but we also obtain new results for the doped case.

5.3 Mean-field results

In this section we discuss our mean-field results for the cases of half-filling and doping away from half-filling. We begin with the half-filled case.

5.3.1 Half-filling case

For the case of half-filling our results are summarized in Fig. 5.1. There are many similarities with results obtained in the literature via different techniques[70, 147, 149, 168, 169, 169]. Most importantly, we find a gapped spin-liquid phase at intermediate coupling that extends to finite spin-orbit coupling. In order of increasing

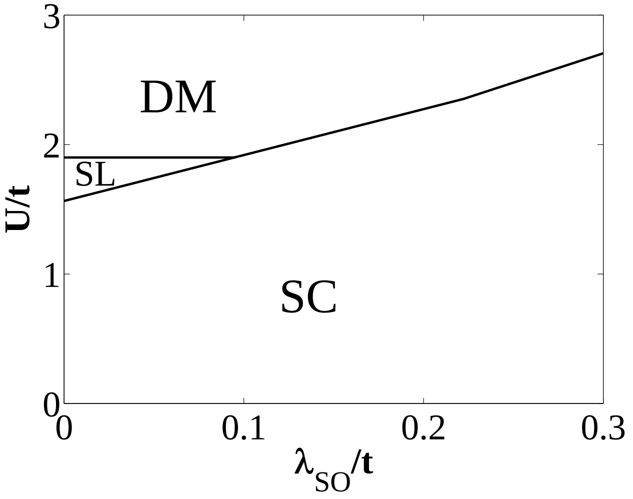

Figure 5.1: Phase diagram of Kane-Mele-Hubbard model at half filling within the slave-boson mean-field approach. SC stands for the superconducting phase, SL is the spin liquid phase and DM is the dimerized phase. The DM phase may be considered as the closest relative to the spin density wave (SDW)/antiferromagnetic state obtained in previous studies[70, 147, 149, 168, 169, 169]. Importantly, the slave-boson treatment also produces a gapped spin liquid at intermediate coupling (which was found in earlier numerical studies[147, 149, 168, 169, 169]). We note, however, that the slave-boson treatment does not smoothly connect to the non-interacting limit since it predicts a SC phase rather than a TBI. This is a shortcoming of the slave-boson mean-field method which is designed to capture the physics of intermediate U values where the SL phase appears.

interactions, the phases we find are:

(1) *Superconducting states* (SC)–When the interaction strength U is small, there is a finite probability of double occupancy and empty occupancy at each site. Therefore, we expect Bose-Einstein condensation of holons and doublons could take place for small U. Indeed, we find a critical interaction strength $U_c(\lambda_{\text{SO}})$ and $U_c \approx 1.5t$ at $\lambda_{\text{SO}} = 0$ above which the SC phase does not survive, which is about half of the value that has been reported in the quantum Monte Carlo simulation[168].

(Although in that case it is a semi-metal that persists up to a critical interaction strength.) The SC phase persists even for a negative interaction, as one might expect. One can view the $U > 0$ SC region as an “extension” from the $U < 0$ region to “small” repulsive interactions. Recent arguments have shown that SC can, surprisingly, be expected even for (small) repulsive interactions[181]. However, as we emphasized earlier, the slave-boson mean-field treatment does not properly capture the small $U > 0$ physics properly in the model *at half-filling*. We do expect SC states to be likely for small U upon doping, and for that reason also discuss the technical details of the half-filled case here which will only be slightly modified upon doping.

From mean-field self-consistency equations, we find that this superconducting state can be described by four finite condensates h_A, h_B, d_A and d_B and finite Δ_f, Δ_b, Δ'_f and Δ'_b (SC I). The four condensates are related via $h_A = -h_B$ and $d_A = -d_B$ (or other equivalent configurations). All other order parameters (*i.e.* the χ) are zero. The physical picture for small interaction is then as follows: the spinons are paired at nearest and second nearest sites and cannot hop freely on the lattice; bosons (doublons and holons) condense independently at $\mathbf{k} = 0$ in momentum space. The ground state has gapless charge excitations and gapped spinon excitations. In terms of the physical electrons pairing, one can show that generally,

$$\begin{aligned}\langle c^\dagger_{i\uparrow} c^\dagger_{j\downarrow}\rangle &= \langle f^\dagger_{i\uparrow} f^\dagger_{j\downarrow}\rangle\langle h_i h_j\rangle - \langle f_{i\downarrow} f_{j\uparrow}\rangle\langle d^\dagger_i d^\dagger_j\rangle \\ &\quad -\langle f^\dagger_{i\uparrow} f_{j\uparrow}\rangle\langle h_i d^\dagger_j\rangle + \langle f_{i\downarrow} f^\dagger_{j\downarrow}\rangle\langle d^\dagger_i h_j\rangle. \qquad (5.6)\end{aligned}$$

To further discuss the properties of this SC phase, let’s consider singlet pairing between the same sublattices in the absence of spin-orbit coupling and we find

$$\langle c^{\dagger}_{0\alpha\uparrow} c^{\dagger}_{\mathbf{r}\alpha\downarrow} \rangle = h_{\alpha} d_{\alpha} \sum_{\mathbf{k}} \frac{-\lambda e^{-i\mathbf{k}\cdot\mathbf{r}}}{\sqrt{\lambda^2 + t^2 |g|^2 \Delta_b^2}}, \tag{5.7}$$

where we have used fact that the Bose-Einstein condensation takes places at weak interactions so that we can replace bosonic operators with their averages. Therefore, one has finite on-site and NNN singlet pairings between same sublattices and also for neighbors arbitrarily far away. On the other hand, we find singlet pairings between different sublattices vanish. It is also possible to obtain another SC solution with finite χs and condensates but zero Δs (SC II)[171]. The spinon sector is the effective noninteracting Kane-Mele model with physical electron operators replaced by neutral spinon operators. Clearly this spinon Hamiltonian possesses non-trivial Z_2 topology and has time-reversal symmetry protected gapless edge states. However, singlet pairings for electrons between same sublattices are finite,

$$\langle c^{\dagger}_{0\alpha\uparrow} c^{\dagger}_{\mathbf{r}\alpha\downarrow} \rangle = h_{\alpha} d_{\alpha} \left[\delta_{0\mathbf{r}} - \sum_{\mathbf{k}, s=\pm 1} \Theta[E_s(\mathbf{k})] e^{i\mathbf{k}\cdot\mathbf{r}} \right], \tag{5.8}$$

where $E_s(\mathbf{k}) \equiv -\lambda + st\chi_b |g(\mathbf{k})|$ and Θ is the Heaviside step function. Similar to SC I, SC II has zero singlet pairings between different sublattices. That's the reason we identify it as a SC state. However, we find SC II is not energetically favorable. In Fig. 5.2, we explicitly show the difference of two mean-field solutions. Note: our mean-field solutions at half filling only admit the above two solutions and there exists no phase with $\chi \neq 0$ and $\Delta \neq 0$ at half filling.

As pointed out in Ref. [171], in the weak interacting limit the Bose gas of doublons and holons is dense (large amplitude of condensates) and one should

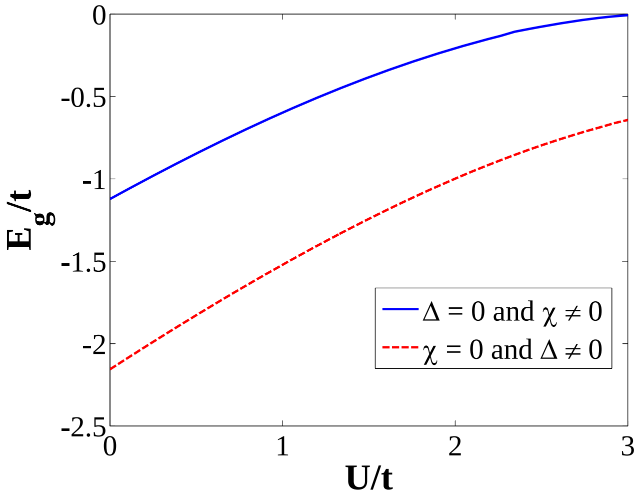

Figure 5.2: The ground state energies for two slave-boson mean-field solutions.

expect the existence of strong interactions between them. Therefore, the slave-boson mean-field approach is not reliable for weak interactions. Indeed, the ground state for weak interactions in the absence (presence) of spin-orbit coupling is a Fermi liquid (TBI). This is confirmed in a recent quantum Monte Carlo study[147].

Another popular approach to handle interactions, the slave-rotor mean-field approach, is believed to be able to reasonably capture the qualitative features of physics at small interactions[133, 134]. It has been applied to the Hubbard model on the honeycomb lattice and predicts a nodal spin liquid phase for $1.68t < U < 1.74t$[142]. Later, it was applied to Kane-Mele-Hubbard model on the same lattice and successfully predicted a TBI phase for weak interactions, though the gauge field has to be screened out to stabilize it[70]. The mathematical structure of slave-rotor approach allows a direct transfer of topology from physical electron bands to neutral spinons; this is the key to predicting a TBI at weak interactions and a TMI at intermediate to strong interactions. However, the slave-rotor method suffers from severe limitations for finite doping[133]. The slave-boson mean-field approach, on the other hand, allows in principle nontrivial band topology embedded in its spinon sector. Unfortunately, in our case we obtain only finite paring terms. As a result, the slave-boson mean-field approximation falsely predicts a SC for half-filling and weak interactions. We also want to mention the Kotliar-Ruckenstein slave-boson mean-field approach describes the weak interacting limit well[182, 183], though it might be difficult to address the intermediate coupling regime and obtain a gapped spin liquid. Furthermore, it predicts the opening of an AF gap for $U \simeq 3t$[177, 184]. It would be interesting to study the interplay of spin-orbit coupling and interaction and this will be left as a future work.

(2) *Spin liquid states* (SL)–As the interaction grows, the Bose gas becomes less dense, and one expects that the slave-boson approach is better able to describe the intermediate interaction regime. We find a spin liquid phase appears between $1.5t < U < 1.9t$ for $\lambda_{\mathrm{SO}} = 0$. In the absence of spin-orbit coupling, this phase is characterized by finite Δ_f and Δ_b. Both the spinon sector and the chargeon sector are gapped and no Bose-Einstein condensation takes place. We find the singlet pairings between any two sites vanish. The expectation value of the spin at each site is also zero, and the spin-spin correlation decays exponentially due to a finite spinon gap. Therefore, we obtain a spin liquid phase in a small interaction window. Furthermore, we find it can survive over a small range of spin-orbit coupling. This feature is quite similar (even numerically) to the quantum Monte Carlo result, though the specific phase boundary differs[147].

To substantiate our assertion that the slave-boson mean-field approach gets better when the interaction grows, we follow Ref. [169] and plot the double occupancy $D_{occ} \equiv \langle n_{i\uparrow} n_{i\downarrow} \rangle$ for $\lambda_{\mathrm{SO}} = 0.02t$ and half-filling at zero temperature in

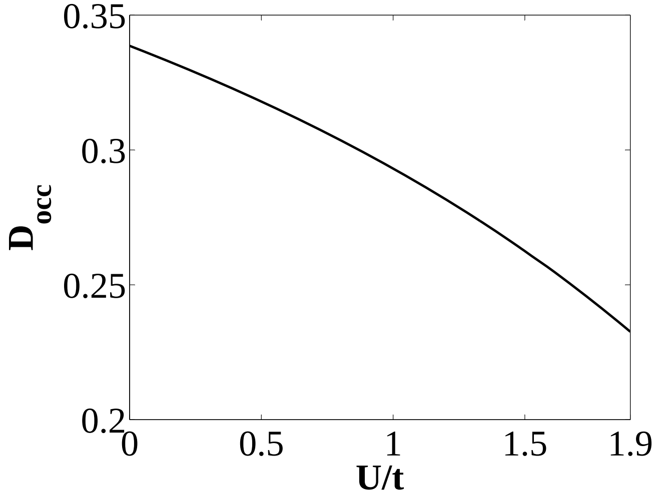

Figure 5.3: Double occupancy as a function of U for $\lambda = 0.02t$ and half-filling at zero temperature from slave-boson mean-field approach. Note the double occupancy at the weak interacting limit is not correct since it is larger than $1/4$, but it gets better as the interaction grows.

Fig. 5.3. As one can see, in the weak interacting regime, D_{occ} is larger than 1/4 (which is the exact values for $U = 0$) and this is another evidence that slave-boson mean-field approach does not work well in the weak interacting regime. However, as the interaction grows, for example, at $U = 1.9t$, our $D_{occ} = 0.23$ at zero temperature and this can be compared with Ref. [169]'s $D_{occ} \approx 0.21$ at $T = 0.025t$. Since a finite temperature tends to reduce the double occupancy, we expect that our result will be very close to that of Ref. [169] if a zero-temperature cellular dynamical mean-field study is performed.

To study the SL phase in more detail, we calculate the single particle retarded Green's function $G^r_{\alpha\sigma}(\mathbf{k},\tau) \equiv -i\theta(t)\langle\{c_{\mathbf{k}\alpha\sigma}(t), c^\dagger_{\mathbf{k}\alpha\sigma}\}\rangle$ in the absence of spin-orbit coupling for the SL phase and the result is

$$G^r_{\alpha\sigma}(\mathbf{k},\omega) = \sum_{\mathbf{q},s=\pm 1} \frac{|v_{\mathbf{q}\text{-}\mathbf{k}}|^2 + |V_{\mathbf{q}}|^2}{\omega + i\eta + sE(\mathbf{q},\mathbf{k})}, \tag{5.9}$$

where $E(\mathbf{q},\mathbf{k}) \equiv E^f(\mathbf{q}) + E^b(\mathbf{q}\text{-}\mathbf{k})$ contains a ferminonic excitation $E^f(\mathbf{k}) \equiv \sqrt{\lambda^2 + t^2|g(\mathbf{k})|^2\Delta_b^2}$ and a bosonic excitation $E^b(\mathbf{k}) \equiv \sqrt{(U/2-\lambda)^2 - t^2|g(\mathbf{k})|^2\Delta_f^2}$. $v_{\mathbf{k}}$ and $V_{\mathbf{k}}$ are defined as $|v_{\mathbf{k}}|^2 = \frac{1}{2}(-1 + \frac{U/2-\lambda}{E^b(\mathbf{k})})$ and $|V_{\mathbf{k}}|^2 = \frac{1}{2}(1 + \frac{\lambda}{E^f(\mathbf{k})})$. As we are considering half-filling, the retarded Green's function exhibits particle-hole symmetry. To make our calculations more solid, we first check if the sum rule of spectrum function $\rho(\mathbf{k},\omega) \equiv \frac{1}{\pi}\mathrm{Im}[G^r_{\alpha\sigma}]$ is satisfied. Since it is based on the anticommunication relations between $c_{\mathbf{k}}$ and $c^\dagger_{\mathbf{k}}$ and it has been taken into account by Eq. 5.3 on the average, the sum rule of our slave-boson mean-field approach is implicitly fulfilled by the mean-field equations. The local density of states $\rho(\omega) \equiv \sum_{\mathbf{k}} \rho(\mathbf{k},\omega)$ is shown in Fig. 5.4 for $U = 1.8t$ and $\lambda_{\mathrm{SO}} = 0$. The single particle gap is found to be $0.57t$. This is the gap at the Dirac point. Instead of calculating it numerically in Ref. [168], we can determine it analytically in our case. The poles of the retarded Green's function are at $\omega = \pm E(\mathbf{q},\mathbf{k})$ and the positive pole reaches its minimum at Dirac point, $\mathbf{q} = \mathbf{k} = \mathbf{K}$, therefore it is clear that the single particle gap at the Dirac point is $\Delta_{\mathrm{sp}} = E(\mathbf{K},\mathbf{K}) = |\lambda| + \sqrt{(U/2-\lambda)^2 - 9t^2\Delta_f^2} = 0.57t$ for $U = 1.8t$. Since our phase boundary for SL differs from Ref. [168], we cannot compare the single particle gap directly for the same U. However, our result for a point sitting about in the middle of SL phase ($0.57t$) is comparable to a typical single particle gap from Ref. [168] (about $0.1t$).

A SL is also found in the slave-rotor mean-field approach, though its properties are quite different from the one obtained here[70, 167]. For example, only hopping terms of spinons are present in the SL within the slave-rotor approach and

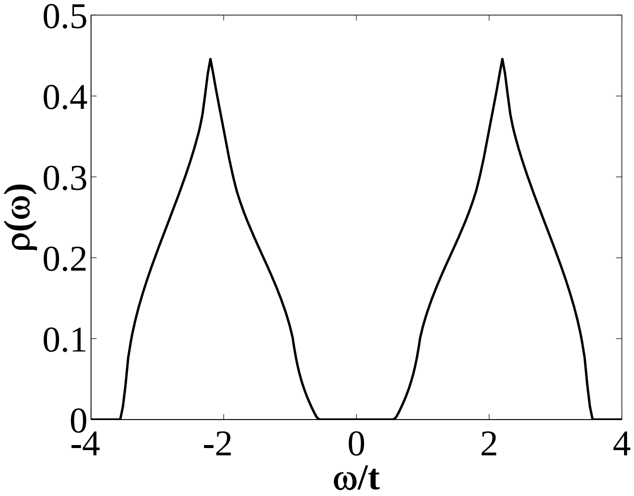

Figure 5.4: The local density of states for the spin liquid phase at half-filling. We have taken $U = 1.8t$ and $\lambda_{\mathrm{SO}} = 0$.

it has a U(1) gauge symmetry. In 2D, U(1) gauge fluctuations are important[150] and it has been argued that other gapless layers (spinons) are required to screen the gauge field and suppress the gauge fluctuations[40]. Our spin/charge gapped SL, however, does not require an additional layer to stabilize the mean-field result. The key difference with the slave-boson approach is that the effective fermionic Hamiltonian for the SL consists of pairing terms instead of hopping of spinons. As a result, the presence of NNN pairings allow the staggered U(1) gauge symmetry to break down to a Z_2 gauge symmetry by the Anderson-Higgs mechanism and gap out the U(1) fluctuations[171]. Therefore, our mean-field result has at least a chance of being realistic, and quantum Monte Carlo calculations[147] and dynamical mean-field theory calculations[169] support this result in a similar parameter regime.

(3) *Dimerized phase* (DM)–The spin liquid phase is unstable to dimerization

in the large U limit. The dimerized phase is close in many respects to an antiferromagnetic phase, which is expected to occur at large interactions on a bi-partite lattice like the honeycomb lattice[70, 147, 149, 168, 169]. With the present form of Kane-Mele-Hubbard model (in the absence of a spin-exchange term), it is difficult to include antiferromagnetic order in our mean-field approach[171]. We will instead turn to a dimerized phase which has anisotropy in some direction (*i.e.* breaks lattice rotational symmetry) yet keeps the translational symmetry intact. Similar ideas have been applied in the slave-rotor approach[40]. To perform our calculations, we will assume rotational symmetry is spontaneously broken. We consider an ansatz of three different mean-field Δ_{f1}, Δ_{f2}, and Δ_{f3} for NN pairings, and Δ'_{f1}, Δ'_{f2}, and Δ'_{f3} for NNN pairings. We do the same in the chargeon sector. In the parameter space we consider, the mean-field solutions are those that satisfy $\Delta_{f1} \neq 0$, $\Delta_{f2} = \Delta_{f3} = 0$ and $\Delta_{b1} \neq 0$, $\Delta_{b2} = \Delta_{b3} = 0$ while the NNN pairings for spinons and bosons vanish. This is an extreme example of dimerization and it corresponds to an atomic-like insulator which consists of noninteracting pairs of NN sites. This can be taken as a “closest cousin” to the antiferromagnetic state expected at large U for half-filling.

To make further connections to the numerical studies, we follow Ref [168] and plot the derivative of the kinetic energy per unit cell dE_{kin}/dU as a function of U/t in Fig. 5.5. After a comparison to the QMC, we find: (i) our kinetic energy is higher than the one in QMC and we expect our ground state energy is also higher, though we are not aware of reported ground state energy in QMC; (ii) Our kinetic energy profile resembles the one in QMC, though we have a jump around $U = 1.9t$ from the spin liquid phase to the dimer phase while it has a continuous behavior in QMC; (iii) Our calculations show that we have a second order phase transition at the first critical point $U_{c1} = 1.5t$ followed by a first order phase transition at $U_{c2} = 1.9t$

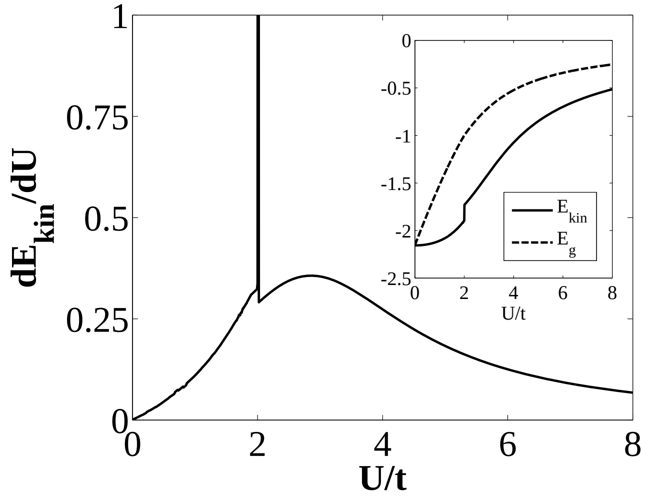

Figure 5.5: The derivative of kinetic energy per unit cell dE_{kin}/dU for $\lambda_{\mathrm{SO}} = 0$. Insert: the kinetic energy and the ground state energy. The kinetic energy has a jump around $U = 1.9t$ and the derivative of it shows a sharp peak at the same location, which indicates a first order transition around $U = 1.9t$.

while there appears to be a continuous Mott transition around $U = 3.5t$[55].

5.3.2 Doping Cases

Up to this point, we have focused on the case of half-filling and our mean-field results could be directly compared with other numerical approaches[70, 147, 149, 168, 169, 169]. We now break new ground by considering the case of doping away from half-filling where other methods may encounter serious shortcomings.

The doped Hubbard model in the strongly interacting limit and its descendant *t*-*J* model are believed to capture the physics of high temperature superconductivity upon doping[99, 185]. In most slave-boson treatments, one assumes strong interactions and simplifies the calculations by removing double occupancy from the

Hilbert space. However, since we are mostly interested in the intermediate regime where U and t are comparable, and a possible spin liquid phase resides, we will start with the Kane-Mele-Hubbard model without assuming a strong interaction. We therefore retain the entire Hilbert space.

Using the mean-field self-consistency equations (see Appendix for details), one finds that the SL at half-filling is unstable to infinitesimal doping and a Bose-Einstein condensations of chargeons takes place for *any* doping. This can be seen from Eq. (6) where the doping is directly related to the condensates. The number of doublons at each site is not equal to the number of holons, and at least one of them has to be finite. This indicates the onset of Bose-Einstein condensation for any doping. Our mean-field solutions show that the χs also acquire finite values, *i.e.* spinons and chargeons can both hop and form pairs on the lattice.

In Fig. 5.6 and Fig. 5.7, we show various NN and NNN order parameters. As one can see, χ_b and χ_b' have linear relations with respect to doping, which readily follows from Eq. (6), Eq. (6) and Eq. (6). χ_f and χ_f' have similar behaviors and are odd functions of doping while Δ_b, Δ_f,Δ_b' and Δ_f' are even functions of doping. Interestingly, the value of Δ_b' and Δ_f' are numerically very close to zero at half filling. The four condensates are related via $h_A = -h_B$ and $d_A = -d_B$(or other equivalent configurations).

In Fig. 5.8, we plot the physical onsite, NN and NNN singlet pairings as a function of doping for parameters $U = 1.8t$ and $\lambda_{\text{SO}} = 0.05t$, whose ground state is a SL without doping. As the doping is increased, singlet pairings between same sublattices and different sublattices acquire finite values and signal the occurrence of a SC phase. The singlet pairings are not monotonic functions of the doping and there exists an “optimal” doping (around ±0.8 electron/site) where the magnitude of on-site and NN parings are maximized. This bears some similarity to the famous

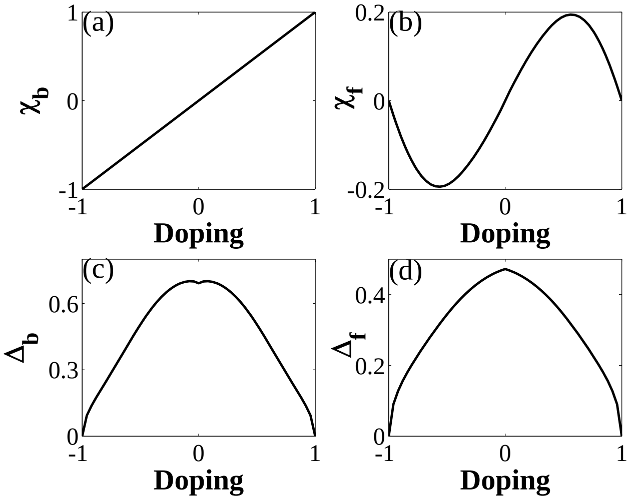

Figure 5.6: The NN order parameters as functions of doping. We have set $U = 1.8t$ and $\lambda_{\text{SO}} = 0.05t$, which is a SL at half-filling.

SC "dome" in the phase diagram of high temperature superconductors[99], though electron doping and hole doping are "equivalent" in our case. We also remark that the dimerized phase will become a SC state via doping. Therefore, upon doping the SC phase takes over the entire phase diagram within the slave-boson mean-field treatment. However, as we mentioned earlier, the SC phase obtained is not one that possess topological order of any obvious type.

In Fig. 5.9, we plot the ground state energy as a function of doping. We have set $U = 1.8t$ and $\lambda_{\text{SO}} = 0.05t$, which is a SL at half-filling. For the ground state energy, one can understand it as follows. At $x = -1$ where electrons are completely depleted the energy is zero, and when one starts to add more electrons to the system, the ground state energy decreases since kinetic energy dominates over the potential energy and lowers the ground state energy. As more electrons are added, the potential energy starts to dominate and cause the increase of ground s-

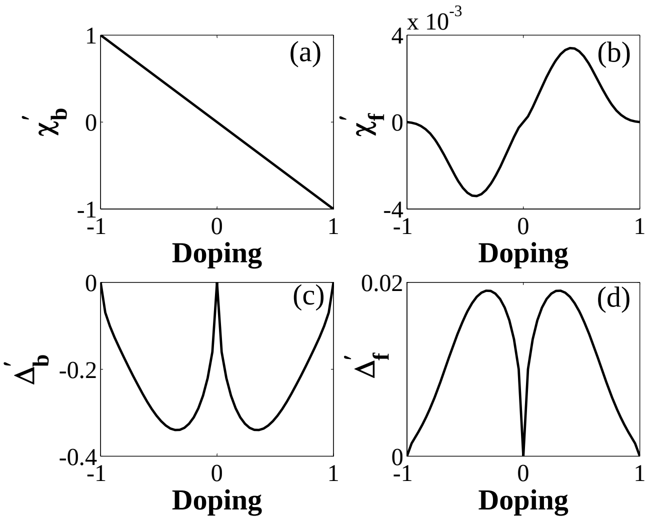

Figure 5.7: The NNN order parameters as functions of doping. We have set $U = 1.8t$ and $\lambda_{\rm SO} = 0.05t$, which is a SL at half-filling.

tate energy. This happens around $x = -0.5$ where χ_f (a measure of kinetic energy) acquires the maximum amplitude. Eventually, when the number of electrons reaches 2 per site, electrons are frozen at each sites and they cannot hop any more and the ground state energy is the classical potential energy ($3.6t$ in our case). Therefore, our slave-boson mean-field calculations is able to replicate the exact ground state energy at two doping limits, and we expect it should describe the intermediate doping well. We comment our ground state energy bears a similar trend to the one in Kotliar-Ruckenstein slave-boson mean-field approach[183].

5.4 Conclusions

In this paper we have studied the Kane-Mele-Hubbard model on the honeycomb lattice via the slave-boson mean-field approach. We have considered both the case

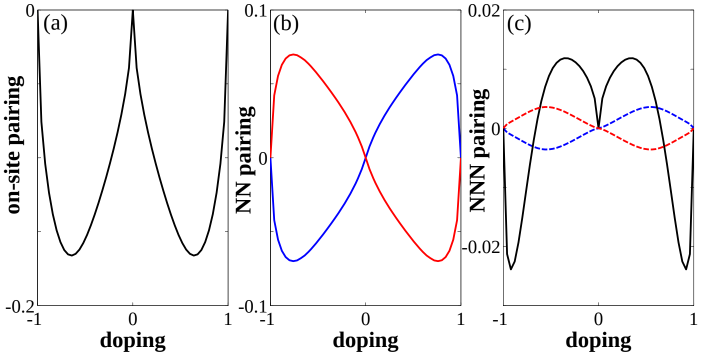

Figure 5.8: Singlet parings at $U = 1.8t$ and $\lambda_{\text{SO}} = 0.05t$ corresponding to the SL at half-filling in Fig.5.1. Shown as a function of doping (additional electrons/site) is: (a) The on-site pairing, (b) the nearest neighbor paring, and (c) the next nearest neighbor pairing. The black solid line is for the real part of the pairing, which is identical for both sublattices; the blue and red solid (dash) lines are for the real (imaginary) part of paring that is different for A and B sublattices.

of half-filling, which has been addressed earlier in the literature via other methods, and the case of doping, which has not been previously investigated to the best of our knowledge. Our main results are summarized in Fig. 5.1 and Fig. 5.8.

At half-filling, the slave-boson mean-field approach fails to capture the correct physics of weak interactions and predicts a SC state (rather than a TBI), but we find it correctly predicts a spin liquid phase for intermediate interactions and small spin-orbit coupling. This is one of the least well understood regimes, and in the presence of strong spin-orbit coupling is likely to lead to new phases[19, 41, 173]. It would be interesting to consider models with further range interactions (first or second-neighbor) to see if they might favor any new phases in the phase diagram, and possibly other mean-field ansatz for the present case as well.

With finite doping, the spin liquid and dimerized phases become supercon-

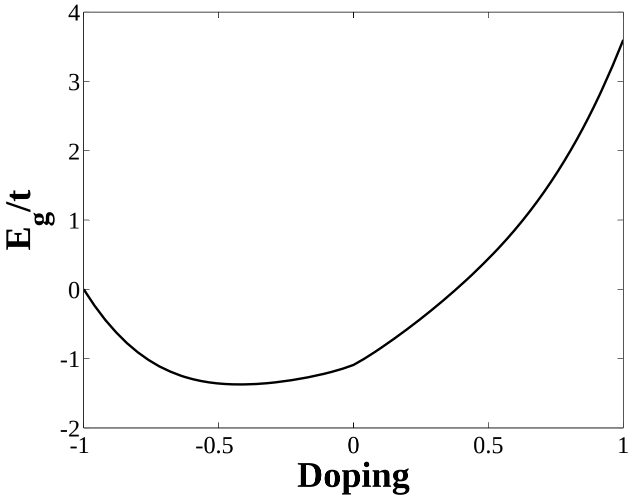

Figure 5.9: The ground state energy per unit cell E_g as a function of doping. We have set $U = 1.8t$ and $\lambda_{\mathrm{SO}} = 0.05t$, which is a SL at half-filling.

ducting states characterized by finite singlet parings (and the superconducting state at half-filling remains a superconducting state). Unfortunately, all the superconducting states we find do not possess any obvious form of topological order. Thus, our work leaves largely open the question of how likely doping-induced topological superconducting states are to appear in models that support interacting topological insulators at half-filling. We hope our work will help to stimulate future studies on the effects of doping topological insulators, including those with longer-range interactions. Doping three dimensional multi-orbital models also seems a promising direction[19, 41].

Chapter 6

Conclusion and Future Directions

I conclude this thesis briefly in this chapter and discuss some of future directions one can take.

The basic question I have been trying to address in this thesis is the interplay between spin-orbit coupling and electron-electron interaction. Due to the complexity of electron-electron interactions (as in any many-body problem), some approximations have to be made and the results depend crucially on them. In some sense, these approximations are biased and our mean-field results could differ from a "true" solution (however one may not be able to find it). The philosophy within the mean-field approach is to start with some guess solution which is reasonable in some limit and reveal as many interesting and exotic phases of topological insulators as possible so that they can be checked against experiments and more sophisticated calculations in the near future.

Once a topological insulator is established without interactions, it is stable against weak interactions until the bulk gap is closed and a quantum phase transition takes place. Usually, the required interaction strength is of intermediate strength (the same order as the kinetic energy), and this regime is notoriously difficult to handle analytically, yet probably the most interesting since the competing between spin-orbit coupling and interactions can result in some exotic phases which cannot be found elsewhere. On the other hand, one might be in a easier position to study the strong interaction limit where some type of spin model can be derived, and there have been numerous publications on spin models obtained in such a way.

Though the basic properties of topological insulators have been established, there remain many open questions to be addressed theoretically and experimentally. Due to the limit of mean-field approach, I only touch a small part of this field. Theoretically, accurate numerical simulations have to be carried out to identify topological insulators, study interaction effects, and compare the results with more analytical approaches. Due to the nature of the many-body problem, this will remain an open question.

Recently, a new phase of matter called the Weyl semimetal has been proposed and studied[186–190]. This resembles a topological insulating state in that there exists gapless surface states and it can also be well described with Bloch band theory. However, unlike a topological insulator where a bulk gap exists, a Weyl semimetal has several band touching points where the chemical potential lies. These band touch points (called "Weyl points") can only be annihilated in pairs. Furthermore, Weyl semimetal can only exist in three dimensions and must break either time-reversal symmetry or inversion symmetry or both. Therefore, it is expected to exist in many systems with magnetic order.

Once these Weyl points are established, it does not require any fine-tuning or symmetry. Therefore, Weyl points are stable against small perturbations. However, to find a Weyl semimetal may be difficult in real materials. In lattice models, however, it has been shown that a Kane-Mele model on the diamond lattice combined with a sublattice potential which breaks inversion symmetry can host Weyl points.

This could be served as a basis for future theoretic study of the Weyl semimetal in the presence of interactions.

Appendix

Transformation to orbital angular momentum states

In terms of the t_{2g} states, the effective $l = 1$ angular momentum states are given by

$$\begin{aligned}
|l_z = 1\rangle &= -\frac{1}{\sqrt{2}}(|yz\rangle + i|zx\rangle) \\
|l_z = 0\rangle &= |xy\rangle \\
|l_z = -1\rangle &= \frac{1}{\sqrt{2}}(|yz\rangle - i|zx\rangle)
\end{aligned}$$

so that in terms of the t_{2g} orbitals the effective l_z angular momentum is given by

$$l_z = \frac{1}{\sqrt{2}} \begin{pmatrix} 0 & 0 & 0 \\ 0 & 0 & i \\ 0 & -i & 0 \end{pmatrix},$$

in the basis (d_{xy}, d_{yz}, d_{zx}). This immediately gives $l_z^2 = n_{yz} + n_{zx}$ in terms of the t_{2g} state occupations.

Spin-orbit coupled states

The transformation between the spin $s = 1/2$ in the effective $l = 1$, t_{2g} orbital basis (d_{xy}, d_{yz}, d_{zx}) and the basis of $|j, j_z\rangle$ for $j = 1/2, 3/2$ is given by

$$\begin{pmatrix} |\frac{1}{2},\frac{1}{2}\rangle \\ |\frac{1}{2},-\frac{1}{2}\rangle \\ |\frac{3}{2},\frac{3}{2}\rangle \\ |\frac{3}{2},\frac{1}{2}\rangle \\ |\frac{3}{2},-\frac{1}{2}\rangle \\ |\frac{3}{2},-\frac{3}{2}\rangle \end{pmatrix} = \begin{pmatrix} 0 & \frac{1}{\sqrt{3}} & 0 & \frac{i}{\sqrt{3}} & \frac{1}{\sqrt{3}} & 0 \\ \frac{1}{\sqrt{3}} & 0 & \frac{-i}{\sqrt{3}} & 0 & 0 & \frac{-1}{\sqrt{3}} \\ \frac{1}{\sqrt{2}} & 0 & \frac{-i}{\sqrt{2}} & 0 & 0 & 0 \\ 0 & \frac{-1}{\sqrt{6}} & 0 & \frac{-i}{\sqrt{6}} & \frac{2}{\sqrt{6}} & 0 \\ \frac{1}{\sqrt{6}} & 0 & \frac{-i}{\sqrt{6}} & 0 & 0 & \frac{2}{\sqrt{6}} \\ 0 & \frac{1}{\sqrt{2}} & 0 & \frac{-i}{\sqrt{2}} & 0 & 0 \end{pmatrix} \begin{pmatrix} |yz\uparrow\rangle \\ |yz\downarrow\rangle \\ |zx\uparrow\rangle \\ |zx\downarrow\rangle \\ |xy\uparrow\rangle \\ |xy\downarrow\rangle \end{pmatrix}.$$

Slave-boson self-consistency equations

In this section, we provide some details on the mean-field self-consistency equations and order parameters for readers interested in the details of our calculations. To obtain the self-consistency equations, we start with the ground state energy per unit cell $E_g = E_f + E_b + E_c$ where E_f (E_b) is the ground state energy from the fermionic (bosonic) part and E_c is an energy constant. We have

$$E_f = -\frac{1}{N}\sum_{\mathbf{k}}\left[\left(A_1 - 2\sqrt{A_2}\right)^{1/2} + \left(A_1 + 2\sqrt{A_2}\right)^{1/2}\right],$$

where A_1 and A_2 are defined as

$$A_1 \equiv \lambda^2 + |g|^2 t^2 \Delta_b^2 + g_1^2 \Delta_b'^2 \lambda_{\mathrm{SO}}^2 + |g|^2 t^2 \chi_b^2 + g_1^2 \lambda_{\mathrm{SO}}^2 \chi_b'^2,$$

$$A_2 \equiv |g|^2\lambda^2 t^2 \chi_b^2 + |g|^2 t^2 g_1^2 \Delta_b'^2 \lambda_{\mathrm{SO}}^2 \chi_b^2 - 2|g|^2 t^2 g_1^2 \Delta_b \Delta_b' \lambda_{\mathrm{SO}}^2 \chi_b \chi_b' + \lambda^2 g_1^2 \lambda_{\mathrm{SO}}^2 \chi_b'^2 + |g|^2 t^2 g_1^2 \Delta_b^2 \lambda_{\mathrm{SO}}^2 \chi_b'^2.$$

The bosonic ground state energy is

$$E_b = -U + \frac{1}{2N}\sum_{\mathbf{k}}\left[\sqrt{(-2\lambda+U)^2 - 4|gt\Delta_f - g_2\Delta_f'\lambda_{\mathrm{SO}}|^2} + \sqrt{(-2\lambda+U)^2 - 4|gt\Delta_f + g_2\Delta_f'\lambda_{\mathrm{SO}}|^2}\right],$$

where we have chosen excitation spectra[191] that may give rise to Bose-Einstein condensation at $\mathbf{k} = 0$. The energy

$$E_c = 2\lambda + 2x\mu - 6(d_B h_A + d_A h_B)t\Delta_f + 12(d_A h_A + d_B h_B)\Delta_f'\lambda_{\mathrm{SO}} + 6(d_A d_B - h_A h_B)t\chi_f + 6t(\Delta_b\Delta_f + \chi_b\chi_f) + (h_A^2 + h_B^2)(-\lambda + \mu + 6\lambda_{\mathrm{SO}}\chi_f') - (d_A^2 + d_B^2)(\lambda - U + \mu + 6\lambda_{\mathrm{SO}}\chi_f') - 12\lambda_{\mathrm{SO}}(\Delta_b'\Delta_f' + \chi_b'\chi_f').$$

Taking the derivative of E_g with respect to the order parameters, we immediately obtain the self-consistency equations:

$$x = \frac{1}{2}(d_A^2 + d_B^2 - h_A^2 - h_B^2),$$

$$\chi_b = h_A h_B - d_A d_B,$$

$$\chi_b' = -\frac{1}{2}(d_A^2 + d_B^2 - h_A^2 - h_B^2),$$

$$
\begin{aligned}
d_A(\lambda - U + \mu + 6\lambda_{\mathrm{SO}}\chi'_f) + 3h_B t\Delta_f - 6h_A\Delta'_f\lambda_{\mathrm{SO}} - 3d_B t\chi_f &= 0,\\
d_B(\lambda - U + \mu + 6\lambda_{\mathrm{SO}}\chi'_f) + 3h_A t\Delta_f - 6h_B\Delta'_f\lambda_{\mathrm{SO}} - 3d_A t\chi_f &= 0,\\
h_A(-\lambda + \mu + 6\lambda_{\mathrm{SO}}\chi'_f) - 3d_B t\Delta_f + 6d_A\Delta'_f\lambda_{\mathrm{SO}} - 3h_B t\chi_f &= 0,\\
h_B(-\lambda + \mu + 6\lambda_{\mathrm{SO}}\chi'_f) - 3d_A t\Delta_f + 6d_B\Delta'_f\lambda_{\mathrm{SO}} - 3h_A t\chi_f &= 0,
\end{aligned}
$$

$$
\chi_f = \frac{1}{6Nt}\sum_{\mathbf{k}}\left[\left(2|g|^2t^2\chi_b - \frac{d_6}{d_5}\right)/d_1 + \left(2|g|^2t^2\chi_b + \frac{d_6}{d_5}\right)/d_2\right],
$$

$$
\Delta_f = \frac{1}{6Nt}\sum_{\mathbf{k}}\left[\left(2|g|^2t^2\Delta_b + \lambda_{\mathrm{SO}}^2\frac{d_7}{d_5}\right)/d_1 + \left(2|g|^2t^2\Delta_b - \lambda_{\mathrm{SO}}^2\frac{d_7}{d_5}\right)/d_2\right],
$$

$$
\Delta_b = d_A h_B + h_A d_B + \frac{1}{3N}\sum_{\mathbf{k}}\left[|g|\big(\big(|g|t\Delta_f + g_2\Delta'_f\lambda_{\mathrm{SO}}\big)/d_3 + \big(|g|t\Delta_f - g_2\Delta'_f\lambda_{\mathrm{SO}}\big)/d_4\big)\right],
$$

$$
\Delta'_f = -\frac{\lambda_{\mathrm{SO}}}{12N}\sum_{\mathbf{k}}\left[\left(2g_1^2\Delta'_b - \frac{d_{10}}{d_5}\right)/d_1 + \left(2g_1^2\Delta'_b + \frac{d_{10}}{d_5}\right)/d_2\right],
$$

$$
\Delta'_b = h_A d_A + h_B d_B - \frac{1}{6N}\sum_{\mathbf{k}}\left[g_2\big(-\big(|g|t\Delta_f + g_2\Delta'_f\lambda_{\mathrm{SO}}\big)/d_3 + \big(|g|t\Delta_f - g_2\Delta'_f\lambda_{\mathrm{SO}}\big)/d_4\big)\right],
$$

$$
\chi'_f = -\frac{\lambda_{\mathrm{SO}}}{12N}\sum_{\mathbf{k}}\left[(2g_1^2\chi'_b - \frac{d_8}{d_5})/d_1 + (2g_1^2\chi'_b + \frac{d_8}{d_5})/d_2\right],
$$

$$2 = d_A^2 + d_B^2 + h_A^2 + h_B^2 - \frac{1}{2N}\sum_{\mathbf{k}}\left[(4\lambda - 2U)\left(\frac{1}{d_3} + \frac{1}{d_4}\right) + 2\left(-2\lambda + \frac{d_9}{d_5}\right)/d_1 - 2\left(2\lambda + \frac{d_9}{d_5}\right)/d_2\right],$$

where the d_i are defined as follows:

$$d_{1,2} = 2\Big[\lambda^2 + |g|^2 t^2\left(\Delta_b^2 + \chi_b^2\right) + g_1^2\lambda_{\text{SO}}^2\left(\Delta_b'^2 + \chi_b'^2\right)$$

$$\mp 2\sqrt{|g|^2 t^2\left(\lambda^2 + g_1^2\Delta_b'^2\lambda_{\text{SO}}^2\right)\chi_b^2 - 2|g|^2 t^2 g_1^2 \Delta_b \Delta_b' \lambda_{\text{SO}}^2 \chi_b \chi_b' + g_1^2\left(\lambda^2 + |g|^2 t^2 \Delta_b^2\right)\lambda_{\text{SO}}^2 \chi_b'^2}\,\Big]^{\frac{1}{2}},$$

$$d_{3,4} = \sqrt{(-2\lambda + U)^2 - 4|g|^2 t^2 \Delta_f^2 \mp 8|g| t g_2 \Delta_f \Delta_f' \lambda_{\text{SO}} - 4 g_2^2 \Delta_f'^2 \lambda_{\text{SO}}^2},$$

$$d_5 = \sqrt{|g|^2 t^2\left(\lambda^2 + g_1^2\Delta_b'^2\lambda_{\text{SO}}^2\right)\chi_b^2 - 2|g|^2 t^2 g_1^2 \Delta_b \Delta_b' \lambda_{\text{SO}}^2 \chi_b \chi_b' + g_1^2\left(\lambda^2 + |g|^2 t^2 \Delta_b^2\right)\lambda_{\text{SO}}^2 \chi_b'^2},$$

$$d_6 = 2|g|^2 t^2\left[\left(\lambda^2 + g_1^2\Delta_b'^2\lambda_{\text{SO}}^2\right)\chi_b - g_1^2 \Delta_b \Delta_b' \lambda_{\text{SO}}^2 \chi_b'\right],$$

$$d_7 = 2|g|^2 t^2 g_1^2 \chi_b'\left(\Delta_b' \chi_b - \Delta_b \chi_b'\right),$$

$$d_8 = 2g_1^2 \left(-|g|^2 t^2 \Delta_b \Delta_b' \chi_b + \lambda^2 \chi_b' + |g|^2 t^2 \Delta_b^2 \chi_b'\right),$$

$$d_9 = 2\lambda \left(|g|^2 t^2 \chi_b^2 + g_1^2 \lambda_{\mathrm{SO}}^2 \chi_b'^2\right),$$

and

$$d_{10} = 2|g|^2 t^2 g_1^2 \chi_b \left(\Delta_b' \chi_b - \Delta_b \chi_b'\right).$$

Bibliography

[1] D. J. Thouless, M. Kohmoto, M. P. Nightingale, and M. den Nijs, Phys. Rev. Lett. **49**, 405 (1982).

[2] X. gang Wen, Advances in Physics **44**, 405 (1995).

[3] C. L. Kane and E. J. Mele, Phys. Rev. Lett. **95**, 226801 (2005).

[4] C. L. Kane and E. J. Mele, Phys. Rev. Lett. **95**, 146802 (2005).

[5] L. Fu, C. L. Kane, and E. J. Mele, Phys. Rev. Lett. **98**, 106803 (2007).

[6] M. Z. Hasan and C. L. Kane, Rev. Mod. Phys. **82**, 3045 (2010).

[7] J. E. Moore, Nature **464**, 194 (2010).

[8] X.-L. Qi and S.-C. Zhang, Physics Today **63**, 33 (2010).

[9] X.-L. Qi and S.-C. Zhang, Rev. Mod. Phys. **83**, 1057 (2011).

[10] B. A. Bernevig, T. L. Hughes, and S.-C. Zhang, Science **314**, 1757 (2006).

[11] M. Konig, S. Wiedmann, C. Brune, A. Roth, H. Buhmann, L. W. Molenkamp, X.-L. Qi, and S.-C. Zhang, Science **318**, 766 (2007).

[12] D. Hsieh, D. Qian, L. Wray, Y. Xia, Y. S. Hor, R. J. Cava, and M. Z. Hasan, Nature **452**, 970 (2008).

[13] D. Hsieh, Y. Xia, D. Qian, L. Wray, J. H. Dil, F. Meier, J. Osterwalder, L. Patthey, J. G. Checkelsky, N. P. Ong, A. V. Fedorov, H. Lin, A. Bansil, D. Grauer, Y. S. Hor, R. J. Cava, and M. Z. Hasan, Nature **460**, 1101 (2009).

[14] F. D. M. Haldane, Phys. Rev. Lett. **61**, 2015 (1988).

[15] Z. Wang, X.-L. Qi, and S.-C. Zhang, Phys. Rev. Lett. **105**, 256803 (2010).

[16] A. Rüegg, J. Wen, and G. A. Fiete, Phys. Rev. B **81**, 205115 (2010).

[17] H. Yao and S. A. Kivelson, Phys. Rev. Lett. **99**, 247203 (2007).

[18] J. Wen, A. Rüegg, C.-C. J. Wang, and G. A. Fiete, Phys. Rev. B **82**, 075125 (2010).

[19] M. Kargarian, J. Wen, and G. A. Fiete, Phys. Rev. B **83**, 165112 (2011).

[20] J. Wen, M. Kargarian, A. Vaezi, and G. A. Fiete, Phys. Rev. B **84**, 235149 (2011).

[21] X. Wan, A. M. Turner, A. Vishwanath, and S. Y. Savrasov, Phys. Rev. B **83**, 205101 (2011).

[22] G. E. Volovik, *The Universe in a Helium Droplet* (Clarendon Press, 2003).

[23] X.-G. Wen, *Quantum Field Theory of Many-Body Systems* (Oxford, New York, 2004).

[24] C. Nayak, S. H. Simon, A. Stern, M. Freedman, and S. D. Sarma, Rev. Mod. Phys. **80**, 1083 (2008).

[25] B. A. Bernevig and S.-C. Zhang, Phys. Rev. Lett. **96**, 106802 (2006).

[26] L. Fu and C. L. Kane, Phys. Rev. B **76**, 045302 (2007).

[27] J. C. Y. Teo, L. Fu, and C. L. Kane, Phys. Rev. B **78**, 045426 (2008).

[28] H. Zhang, C.-X. Liu, X.-L. Qi, X. Dai, Z. Fang, and S.-C. Zhang, Nat. Phys. **5**, 438 (2009).

[29] A. Roth, C. Brüne, H. Buhmann, L. W. Molenkamp, J. Maciejko, X.-L. Qi, and S.-C. Zhang, Science **325**, 294 (2009).

[30] Y. Xia, D. Qian, D. Hsieh, L. Wray, A. Pal, H. Lin, A. Bansil, D. Grauer, Y. S. Hor, R. J. Cava, and M. Z. Hasan, Nat. Phys. **5**, 398 (2009).

[31] Y. L. Chen, G. Analytis, J.-H. Chu, Z. K. Liu, S.-K. Mo, X. L. Qi, H. J. Zhang, D. H. Lu, X. Dai, Z. Fang, S. C. Zhang, I. R. Fisher, Z. Hussain, and Z.-X. Shen, Science **325**, 178 (2009).

[32] A. Kitaev, Annals of Physics **321**, 2 (2006), january Special Issue.

[33] H.-M. Guo and M. Franz, Phys. Rev. B **80**, 113102 (2009).

[34] H.-M. Guo and M. Franz, Phys. Rev. Lett. **103**, 206805 (2009).

[35] C. Wu, D. Arovas, and H.-H. Hung, Phys. Rev. B **79**, 134427 (2009).

[36] A. P. Schnyder, S. Ryu, and A. W. W. Ludwig, Phys. Rev. Lett. **102**, 196804 (2009).

[37] S. Raghu, X.-L. Qi, C. Honerkamp, and S.-C. Zhang, Phys. Rev. L **100**, 156401 (2008).

[38] Y. Zhang, Y. Ran, and A. Vishwanath, Phys. Rev. B **79**, 245331 (2009).

[39] T. Grover and T. Senthil, Phys. Rev. Lett. **100**, 156804 (2008).

[40] M. W. Young, S.-S. Lee, and C. Kallin, Phys. Rev. B **78**, 125316 (2008).

[41] D. Pesin and L. Balents, Nat. Phys. **6**, 376 (2010).

[42] K. Ohgushi, S. Murakami, and N. Nagaosa, Phys. Rev. B **62**, R6065 (2000).

[43] D.-H. Lee, G.-M. Zhang, and T. Xiang, Phys. Rev. Lett. **99**, 196805 (2007).

[44] S. Murakami, S. Iso, Y. Avishai, M. Onoda, and N. Nagaosa, Phys. Rev. B **76**, 205304 (2007).

[45] A. M. Essin and J. E. Moore, Phys. Rev. B **76**, 165307 (2007).

[46] D. N. Sheng, Z. Y. Weng, L. Sheng, and F. D. M. Haldane, Phys. Rev. Lett. **97**, 036808 (2006).

[47] K. Sun, H. Yao, E. Fradkin, and S. A. Kivelson, Phys. Rev. Lett. **103**, 046811 (2009).

[48] C.-Y. Hou, C. Chamon, and C. Mudry, Phys. Rev. Lett. **98**, 186809 (2007).

[49] G. Jackeli and G. Khaliullin, Phys. Rev. Lett. **102**, 017205 (2009).

[50] S. Dusuel, K. P. Schmidt, J. Vidal, and R. L. Zaffino, Phys. Rev. B **78**, 125102 (2008).

[51] T. Fukui, Y. Hatsugai, and H. Suzuki, J. Phys. Soc. Jap. **74**, 1674 (2005).

[52] V. Chua, H. Yao, and G. A. Fiete, Phys. Rev. B **83**, 180412 (2011).

[53] X. Hu, M. Kargarian, and G. A. Fiete, Phys. Rev. B **84**, 155116 (2011).

[54] M. Kargarian and G. A. Fiete, Phys. Rev. B **82**, 085106 (2010).

[55] F. Wang, Phys. Rev. B **81**, 184416 (2010).

[56] Y.-Z. Zheng, M.-L. Tong, W. Xue, W.-Z. Zhang, X.-M. Chen, F. Grandjean, and G. Long, Agnew. Chem. Int. Edn. **46**, 6076 (2007).

[57] L.-M. Duan, E. Demler, and M. D. Lukin, Phys. Rev. Lett. **91**, 090402 (2003).

[58] J. Ruostekoski, Phys. Rev. Lett. **103**, 080406 (2009).

[59] A. P. Schnyder, S. Ryu, A. Furusaki, and A. W. W. Ludwig, Phys. Rev. B **78**, 195125 (2008).

[60] J. E. Moore and L. Balents, Phys. Rev. B **75**, 121306 (2007).

[61] R. Roy, Phys. Rev. B **79**, 195322 (2009).

[62] D. Hsieh, Y. Xia, L. Wray, D. Qian, A. Pal, J. H. Dil, J. Osterwalder, F. Meier, B. Bihlmayer, C. L. Kane, Y. Hor, R. J. Cava, and M. Z. Hasan, Science **323**, 919 (2009).

[63] D. Hsieh, Y. Xia, D. Qian, L. Wray, F. Meier, J. H. Dil, J. Osterwalder, L. Patthey, A. V. Fedorov, H. Lin, A. Bansil, D. Grauer, Y. S. Hor, R. J. Cava, and M. Z. Hasan, Phys. Rev. Lett. **103**, 146401 (2009).

[64] H.-J. Zhang, S. Chadov, L. Müchler, B. Yan, X.-L. Qi, J. Kübler, S.-C. Zhang, and C. Felser, Phys. Rev. Lett. **106**, 156402 (2011).

[65] S. Chadov, X.-L. Qi, J. Kübler, G. H. Fecher, C. Felser, and S.-C. Zhang, Nat. Mat. **9**, 541 (2010).

[66] Y. X. S. X. S. J. R. J. C. A. B. M. Z. H. Hsin Lin, L. Andrew Wray, Nature Materials **9**, 546 (2010).

[67] H. Lin, L. Wray, Y. Xia, S.-Y. Xu, S. Jia, R. Cava, A. Bansil, and M. Hasan, arXiv:1004.0999 (2010).

[68] J. Li, R.-L. Chu, J. K. Jain, and S.-Q. Shen, Phys. Rev. Lett. **102**, 136806 (2009).

[69] C. W. Groth, M. Wimmer, A. R. Akhmerov, J. Tworzydło, and C. W. J. Beenakker, Phys. Rev. Lett. **103**, 196805 (2009).

[70] S. Rachel and K. Le Hur, Phys. Rev. B **82**, 075106 (2010).

[71] I. Affleck and J. B. Marston, Phys. Rev. B **37**, 3774 (1988).

[72] X.-G. Wen and P. A. Lee, Phys. Rev. Lett. **76**, 503 (1996).

[73] C. M. Varma, Phys. Rev. Lett. **83**, 3538 (1999).

[74] S. Chakravarty, R. B. Laughlin, D. K. Morr, and C. Nayak, Phys. Rev. B **63**, 094503 (2001).

[75] A. Mielke, Journal of Physics A: Mathematical and General **25**, 4335 (1992).

[76] H. Tasaki, Progress of Theoretical Physics **99**, 489 (1998).

[77] F. Pollmann, P. Fulde, and K. Shtengel, Phys. Rev. Lett. **100**, 136404 (2008).

[78] T. Ohashi, N. Kawakami, and H. Tsunetsugu, Phys. Rev. Lett. **97**, 066401 (2006).

[79] M. Hermele, Y. Ran, P. A. Lee, and X.-G. Wen, Phys. Rev. B **77**, 224413 (2008).

[80] F. Wang and A. Vishwanath, Phys. Rev. B **74**, 174423 (2006).

[81] R. R. P. Singh and D. A. Huse, Phys. Rev. B **76**, 180407 (2007).

[82] G. Evenbly and G. Vidal, Phys. Rev. Lett. **104**, 187203 (2010).

[83] J. S. Helton, K. Matan, M. P. Shores, E. A. Nytko, B. M. Bartlett, Y. Yoshida, Y. Takano, A. Suslov, Y. Qiu, J.-H. Chung, D. G. Nocera, and Y. S. Lee, Phys. Rev. Lett. **98**, 107204 (2007).

[84] T. Imai, E. A. Nytko, B. M. Bartlett, M. P. Shores, and D. G. Nocera, Phys. Rev. Lett. **100**, 077203 (2008).

[85] W. Koshibae and S. Maekawa, Phys. Rev. Lett. **91**, 257003 (2003).

[86] M. Indergand, Y. Yamashita, H. Kusunose, and M. Sigrist, Phys. Rev. B **71**, 214414 (2005).

[87] B.-J. Yang, A. Paramekanti, and Y. B. Kim, Phys. Rev. **81**, 134418 (2010).

[88] C. Weeks and M. Franz, Phys. Rev. B **81**, 085105 (2010).

[89] D. A. Huse and V. Elser, Phys. Rev. Lett. **60**, 2531 (1988).

[90] B. Bernu, P. Lecheminant, C. Lhuillier, and L. Pierre, Phys. Rev. B **50**, 10048 (1994).

[91] A. Singh, Phys. Rev. B **71**, 214406 (2005).

[92] S. Nishimoto, M. Nakamura, A. O'Brien, and P. Fulde, Phys. Rev. Lett. **104**, 196401 (2010).

[93] A. O'Brien, F. Pollmann, and P. Fulde, Phys. Rev. B **81**, 235115 (2010).

[94] R. Moessner, S. L. Sondhi, and P. Chandra, Phys. Rev. B **64**, 144416 (2001).

[95] B. Seradjeh and M. Franz, Phys. Rev. Lett. **101**, 146401 (2008).

[96] M. Indergand, A. Läuchli, S. Capponi, and M. Sigrist, Phys. Rev. B **74**, 064429 (2006).

[97] S. Maekawa, T. Tohyama, S. E. Barnes, S. Ishihara, W. Koshibae, and G. Khaliullin, *Physics of Transition Metal Oxides* (Springer, Heidelberg, Germany, 2004).

[98] Y. Tokura, *Colossal Magnetoresistive Oxides* (Gordon and Beach, New York, 2000).

[99] P. A. Lee, N. Nagaosa, and X.-G. Wen, Rev. Mod. Phys. **78**, 17 (2006).

[100] E. Dagotto, Rev. Mod. Phys. **66**, 763 (1994).

[101] M. B. Salamon and M. Jaime, Rev. Mod. Phys. **73**, 583 (2001).

[102] S.-H. Lee, Y. Qiu, C. Broholm, Y. Ueda, and J. J. Rush, Phys. Rev. Lett. **86**, 5554 (2001).

[103] A. Shimoyamada, S. Tsuda, K. Ishizaka, T. Kiss, T. Shimojima, T. Togashi, S. Watanabe, C. Q. Zhang, C. T. Chen, Y. Matsushita, H. Ueda, Y. Ueda, and S. Shin, Phys. Rev. Lett. **96**, 026403 (2006).

[104] P. E. Jönsson, K. Takenaka, S. Niitaka, T. Sasagawa, S. Sugai, and H. Takagi, Phys. Rev. Lett. **99**, 167402 (2007).

[105] L. Balents, Nature **464**, 199 (2010).

[106] M. Imada, A. Fujimori, and Y. Tokura, Rev. Mod. Phys. **70**, 1039 (1998).

[107] W. D. Ryden, A. W. Lawson, and C. C. Sartain, Phys. Rev. B **1**, 1494 (1970).

[108] S. J. Moon, M. W. Kim, K. W. Kim, Y. S. Lee, J.-Y. Kim, J.-H. Park, B. J. Kim, S.-J. Oh, S. Nakatsuji, Y. Maeno, I. Nagai, S. I. Ikeda, G. Cao, and T. W. Noh, Phys. Rev. B **74**, 113104 (2006).

[109] S. Nakatsuji and Y. Maeno, Phys. Rev. Lett. **84**, 2666 (2000).

[110] J. S. Lee, Y. S. Lee, T. W. Noh, K. Char, J. Park, S.-J. Oh, J.-H. Park, C. B. Eom, T. Takeda, and R. Kanno, Phys. Rev. B **64**, 245107 (2001).

[111] B. J. Kim, H. Jin, S. J. Moon, J.-Y. Kim, B.-G. Park, C. S. Leem, J. Yu, T. W. Noh, C. Kim, S.-J. Oh, J.-H. Park, V. Durairaj, G. Cao, and E. Rotenberg, Phys. Rev. Lett. **101**, 076402 (2008).

[112] B. J. Kim, H. Ohsumi, T. Komesu, S. Sakai, T. Morita, H. Takagi, and T. Arima, Science **323**, 1329 (2009).

[113] H. Jin, H. Jeong, T. Ozaki, and J. Yu, Phys. Rev. B **80**, 075112 (2009).

[114] Y. Singh and P. Gegenwart, Phys. Rev. B **82**, 064412 (2010).

[115] H. Jin, H. Kim, H. Jeong, C. H. Kim, and J. Yu, arXiv:0907.0743 (2009).

[116] H. Watanabe, T. Shirakawa, and S. Yunoki, Phys. Rev. Lett. **105**, 216410 (2010).

[117] Y. Okamoto, M. Nohara, H. Aruga-Katori, and H. Takagi, Phys. Rev. Lett. **99**, 137207 (2007).

[118] M. J. Lawler, H.-Y. Kee, Y. B. Kim, and A. Vishwanath, Phys. Rev. Lett. **100**, 227201 (2008).

[119] G. Chen and L. Balents, Phys. Rev. B **78**, 094403 (2008).

[120] Y. Zhou, P. A. Lee, T.-K. Ng, and F.-C. Zhang, Phys. Rev. Lett. **101**, 197201 (2008).

[121] M. J. Lawler, A. Paramekanti, Y. B. Kim, and L. Balents, Phys. Rev. Lett. **101**, 197202 (2008).

[122] M. R. Norman and T. Micklitz, Phys. Rev. B **81**, 024428 (2010).

[123] T. Micklitz and M. R. Norman, Phys. Rev. B **81**, 174417 (2010).

[124] E. J. Bergholtz, A. M. Läuchli, and R. Moessner, Phys. Rev. Lett. **105**, 237202 (2010).

[125] J. Chaloupka, G. Jackeli, and G. Khaliullin, Phys. Rev. Lett. **105**, 027204 (2010).

[126] A. Shitade, H. Katsura, J. Kuneš, X.-L. Qi, S.-C. Zhang, and N. Nagaosa, Phys. Rev. Lett. **102**, 256403 (2009).

[127] R. Li, J. Wang, X.-L. Qi, and S.-C. Zhang, Nat. Phys. **6**, 284 (2010).

[128] J. Wang, R. Li, S.-C. Zhang, and X.-L. Qi, Phys. Rev. Lett. **106**, 126403 (2011).

[129] F. Wang and T. Senthil, Phys. Rev. Lett. **106**, 136402 (2011).

[130] T. Dodds, T.-P. Choy, and Y. B. Kim, Phys. Rev. B **84**, 104439 (2011).

[131] S. Landron and M.-B. Lepetit, Phys. Rev. B **77**, 125106 (2008).

[132] A. Shitade, H. Katsura, J. Kuneš, X.-L. Qi, S.-C. Zhang, and N. Nagaosa, Phys. Rev. Lett. **102**, 256403 (2009).

[133] S. Florens and A. Georges, Phys. Rev. B **66**, 165111 (2002).

[134] S. Florens and A. Georges, Phys. Rev. B **70**, 035114 (2004).

[135] B.-J. Yang and Y. B. Kim, Phys. Rev. B **82**, 085111 (2010).

[136] G. Chen, R. Pereira, and L. Balents, Phys. Rev. B **82**, 174440 (2010).

[137] D. L. Bergman, R. Shindou, G. A. Fiete, and L. Balents, Phys. Rev. B **74**, 134409 (2006).

[138] Y. Ran, Y. Xhang, and A. Vishwanath, Nat. Phys. **5**, 298 (2009).

[139] D. Mandrus, J. R. Thompson, R. Gaal, L. Forro, J. C. Bryan, B. C. Chakoumakos, L. M. Woods, B. C. Sales, R. S. Fishman, and V. Keppens, Phys. Rev. B **63**, 195104 (2001).

[140] D. J. Singh, P. Blaha, K. Schwarz, and J. O. Sofo, Phys. Rev. B **65**, 155109 (2002).

[141] D. Podolsky, A. Paramekanti, Y. B. Kim, and T. Senthil, Phys. Rev. Lett. **102**, 186401 (2009).

[142] S.-S. Lee and P. A. Lee, Phys. Rev. Lett. **95**, 036403 (2005).

[143] A. M. Polyakov, Phys. Lett. **59B**, 82 (1975).

[144] I. F. Herbut, B. H. Seradjeh, S. Sachdev, and G. Murthy, Phys. Rev. B **68**, 195110 (2003).

[145] I. F. Herbut and B. H. Seradjeh, Phys. Rev. Lett. **91**, 171601 (2003).

[146] M. Hermele, T. Senthil, M. P. A. Fisher, P. A. Lee, N. Nagaosa, and X.-G. Wen, Phys. Rev. B **70**, 214437 (2004).

[147] M. Hohenadler, T. C. Lang, and F. F. Assaad, Phys. Rev. Lett. **106**, 100403 (2011).

[148] D. Zheng, G.-M. Zhang, and C. Wu, Phys. Rev. B **84**, 205121 (2011).

[149] Y. Yamaji and M. Imada, Phys. Rev. B **83**, 205122 (2011).

[150] W. Witczak-Krempa, T. P. Choy, and Y. B. Kim, Phys. Rev. B **82**, 165122 (2010).

[151] Q. Liu, H. Yao, and T. Ma, Phys. Rev. B **82**, 045102 (2010).

[152] C. N. Varney, K. Sun, M. Rigol, and V. Galitski, Phys. Rev. B **82**, 115125 (2010).

[153] H.-M. Guo, G. Rosenberg, G. Refael, and M. Franz, Phys. Rev. Lett. **105**, 216601 (2010).

[154] M. A. Subramanian, G. Aravamudan, and G. V. S. Rao, Prog. Solid State Chem. **15**, 55 (1983).

[155] J. Maciejko, X.-L. Qi, A. Karch, and S.-C. Zhang, Phys. Rev. Lett. **105**, 246809 (2010).

[156] B. Swingle, M. Barkeshli, J. McGreevy, and T. Senthil, "Correlated topological insulators and the fractional magnetoelectric effect," (2010), arXiv:1005.1076.

[157] G. Y. Cho and J. E. Moore, "Topological bf field theory description of topological insulators," (2010), arXiv:1011.3485.

[158] B. Canals and C. Lacroix, Phys. Rev. Lett. **80**, 2933 (1998).

[159] B. Canals and C. Lacroix, Phys. Rev. B **61**, 1149 (2000).

[160] D. L. Bergman, G. A. Fiete, and L. Balents, Phys. Rev. B **73**, 134402 (2006).

[161] M. Elhajal, B. Canals, R. Sunyer, and C. Lacroix, Phys. Rev. B **71**, 094420 (2005).

[162] J. D. M. Champion, M. J. Harris, P. C. W. Holdsworth, A. S. Wills, G. Balakrishnan, S. T. Bramwell, E. Čižmár, T. Fennell, J. S. Gardner, J. Lago, D. F. McMorrow, M. Orendáč, A. Orendáčová, D. M. Paul, R. I. Smith, M. T. F. Telling, and A. Wildes, Phys. Rev. B **68**, 020401 (2003).

[163] F. Zhang, J. Jung, G. A. Fiete, Q. Niu, and A. H. MacDonald, Phys. Rev. Lett. **106**, 156801 (2011).

[164] A. Rüegg and G. A. Fiete, Phys. Rev. B **83**, 165118 (2011).

[165] F. Wang and Y. Ran, Phys. Rev. B **84**, 241103 (2011).

[166] K.-Y. Yang, W. Zhu, D. Xiao, S. Okamoto, Z. Wang, and Y. Ran, Phys. Rev. B **84**, 201104 (2011).

[167] J. He, S.-P. Kou, Y. Liang, and S. Feng, Phys. Rev. B **83**, 205116 (2011).

[168] Z. Y. Meng, T. C. Lang, S. Wessel, F. F. Assaad, and A. Muramatsu, Nature **464**, 847 (2010).

[169] W. Wu, S. Rachel, W.-M. Liu, and K. L. Hur, arXiv:1106.0943 (2011).

[170] B. K. Clark, D. A. Abanin, and S. L. Sondhi, Phys. Rev. Lett. **107**, 087204 (2011).

[171] A. Vaezi and X.-G. Wen, arXiv:1010.5744v1 (2010).

[172] Y.-M. Lu and Y. Ran, Phys. Rev. B **84**, 024420 (2011).

[173] A. Rüegg and G. A. Fiete, Phys. Rev. Lett. **108**, 046401 (2012).

[174] D. Xiao, W. Zhu, Y. Ran, N. Nagaosa, and S. Okamoto, Nature Communications **2**, 536 (2011).

[175] G. A. Fiete, V. Chua, M. Kargarian, R. Lundgren, A. Regg, J. Wen, and V. Zyuzin, Physica E: Low-dimensional Systems and Nanostructures , (2011).

[176] M. Troyer and U.-J. Wiese, Phys. Rev. Lett. **94**, 170201 (2005).

[177] J. M. C. F. G. Dionys Baeriswyl, David K. Campbell and E. Louis(Eds.), *The Hubbard Model: Its Physics and its Mathematical Physics* (Springer, 1995).

[178] S. E. Barnes, J. Phys. F: Met. Phys. **6**, 1375 (1976).

[179] P. Coleman, Phys. Rev. B **29**, 3035 (1984).

[180] Z. Zou and P. W. Anderson, Phys. Rev. B **37**, 627 (1988).

[181] S. Raghu and S. A. Kivelson, Phys. Rev. B **83**, 094518 (2011).

[182] G. Kotliar and A. E. Ruckenstein, Phys. Rev. Lett. **57**, 1362 (1986).

[183] L. Lilly, A. Muramatsu, and W. Hanke, Phys. Rev. Lett. **65**, 1379 (1990).

[184] R. Fresard and K. Doll, arXiv:cond-mat/9603125v1 (1996).

[185] T. Senthil and P. A. Lee, Phys. Rev. B **71**, 174515 (2005).

[186] X. Wan, A. Vishwanath, and S. Y. Savrasov, "Computational design of axion insulators based on 5d spinels compounds," (2011), arXiv:1103.4634.

[187] A. A. Burkov and L. Balents, Phys. Rev. Lett. **107**, 127205 (2011).

[188] A. A. Burkov, M. D. Hook, and L. Balents, Phys. Rev. B **84**, 235126 (2011).

[189] K.-Y. Yang, Y.-M. Lu, and Y. Ran, Phys. Rev. B **84**, 075129 (2011).

[190] G. Xu, H. Weng, Z. Wang, X. Dai, and Z. Fang, Phys. Rev. Lett. **107**, 186806 (2011).

[191] J.-P. Blaizot and G. Ripka, *Quantum Theory of Finite Systems* (The MIT Press, Cambridge, Massachusetts, 1986).

Vita

Jun Wen was born in Jiangsu, China in 1982. He received the Bachelor of Science degree in Physics in July 2004 and Master of Science degree in Physics in July 2007 from Nanjing University. In August 2007 he started to study in the Graduate School of the University of Texas at Austin to pursue a PhD in Physics.

Permanent Address: 1642 W. 6th Street, Apt C, Austin, TX 78703

This dissertation was typeset by the author.

List of Publications

[1] Jun Wen, Mehdi Kargarian, Abolhassan Vaezi, Gregory A. Fiete, *Doping the Kane-Mele-Hubbard model: A Slave-Boson Approach*, Physical Review B, **84**, 235149 (2011).

[2] Wanxiang Feng, Jun Wen, Jinjian Zhou, Di Xiao, Yugui Yao, *First-principles calculation of topological invariants Z2 within the FP-LAPW formalism* (submitted, arXiv:1107.2679).

[3] Gregory A. Fiete, Victor Chua, Xiang Hu, Mehdi Kargarian, Rex Lundgren, Andreas Ruegg, Jun Wen, Vladimir Zyuzin, *Topological Insulators and Quantum Spin Liquids* (accepted, to appear in Physica E, arXiv:1106.0013).

[4] Mehdi Kargarian, Jun Wen, Gregory A. Fiete, *Competing exotic topological insulator phases in transition metal oxides on the pyrochlore lattice with distortion*, Physical

Review B **83**, 165112 (2011).

[5] Di Xiao, Yugui Yao, Wanxiang Feng, Jun Wen, Wenguang Zhu, Xing-Qiu Chen, G. Malcolm Stocks, and Zhenyu Zhang, *Half-Heusler compounds as a new class of three dimensional topological insulators*, Physical Review Letters **105**, 096404 (2010).

[6] Jun Wen, Andreas Ruegg, C.-C. Joseph Wang, Gregory A. Fiete, *Interaction-driven topological insulators on the kagome and the decorated honeycomb lattices*, Physical Review B **82**, 075125 (2010).

[7] Andreas Ruegg, Jun Wen, and Gregory A. Fiete, *Topological insulators on the decorated honeycomb lattice*, Physical Review B **81**, 205115 (2010).